

# Coupled FEM-BEM Techniques for 2D Inverse Wave Scattering Problems

**Sherwin Bagheri**

B. Sc. (Hons) Macquarie University (2012)

**Supervisor: Dr Stuart C. Hawkins**

A thesis presented for the degree of  
Doctor of Philosophy



**MACQUARIE**  
University

Department of Mathematics

Macquarie University

Sydney, Australia

2016

---

## Declaration

I certify that the work in this thesis has not previously been submitted for a degree nor has it been submitted as part of the requirements for a degree to any other university or institution other than Macquarie University.

I also certify that this thesis is an original piece of research and has been written by me. Any help and assistance that I have recieved in my research work and the preparation of the thesis itself has been appropriately acknowledged.

In addition, I certify that all information sources and literature used are indicated in the thesis.

---

Sherwin Bagheri

date: 

---

---

## Acknowledgements

First and foremost I would like to take this opportunity to thank God, who I believe is solely responsible for each and every blessing I have in my life.

In particular I would like to thank Him for giving me two amazing parents. Without their support, I would have never been able to embark on an education, and would not have been able to pursue a PhD in the first place.

I would like to thank my dear supervisor Stuart Hawkins, who introduced me to the world of research some five years ago. He has patiently trained me ever since, and I thank him for his remarkable insight, excellent guidance and wonderful support during that time. Without his supervision, none of this thesis would have been possible.

I would also like to thank the staff of the Mathematics Department at Macquarie University for all the kindness they have shown me during the course of my studies. In particular, I would like to express my sincere thanks to Rod Yager, Paul Smith, Christine Hale, Frank Valckenborgh, Jim Denier, Carolyn Kennet, Dilshara Hill and Garry Lawson.

Last but not least, I would like to thank all my friends who have supported me during my studies. In particular, I would like to thank Fu Ken Ly, Cheong Ho Seng, Kenny Liew, Poon Leung, Audrey Markowskei, Remy Tuyeras, Joshua Peate, Geoff Edington-Cheater, Leon Beale, Ramon Abud Alcala and Branko Nikolic.

# Abstract

In this thesis we consider an impenetrable cylindrical scatterer surrounded by a heterogeneous dielectric coating. We present a numerical scheme for reconstructing the refractive index of the heterogeneous medium using far field data. The numerical scheme is based only on the mild assumption that the inhomogeneous medium is contained inside a circular cylinder, and does not require axis-symmetry or other similar restrictions. Moreover, we only require the boundary of the scatterer to be piecewise smooth. We reformulate this inverse problem as a nonlinear equation, which we then solve using a regularised Newton-type solver. The key innovation is performing nonlinear function evaluations, which involve solving a forward scattering problem, using an efficient coupled finite-element/boundary element method (FEM-BEM) for the heterogeneous Helmholtz equation, which ensures that the important radiation condition is incorporated exactly. We derive an analytic representation for the Fréchet derivative for the heterogeneous dielectric coated scatterer, which we efficiently compute using a novel extension of the coupled FEM-BEM scheme. The scheme is then demonstrated by reconstructing challenging continuous and discontinuous media from noisy far field data.

# Contents

<b>1</b>	<b>Introduction</b>	<b>8</b>
1.1	Background . . . . .	9
1.2	Review of the Literature . . . . .	23
1.3	Thesis Outline . . . . .	26
<b>2</b>	<b>Preliminaries</b>	<b>29</b>
2.1	Function Spaces . . . . .	29
2.2	Inverse Problem Theory . . . . .	33
2.2.1	Linearization . . . . .	37
2.2.2	Tikhonov Regularization . . . . .	38
2.2.3	Morozov Discrepancy Principle . . . . .	39
2.3	Angular Legendre Functions . . . . .	41
2.4	Notational and Variable Definitions . . . . .	42
<b>3</b>	<b>Coupled FEM-BEM Technique</b>	<b>44</b>
3.1	Motivation . . . . .	46
3.2	Coupled FEM-BEM Technique . . . . .	47
3.3	Galerkin Scheme . . . . .	51
3.3.1	Evaluating the exterior field . . . . .	53
3.3.2	Evaluating the interior field . . . . .	58
3.3.3	Constructing the Solution to the Forward Problem . . . . .	61
3.4	Numerical Results . . . . .	62

3.4.1	Efficiency of the Nyström Method . . . . .	63
3.4.2	Accuracy of the FEM . . . . .	64
3.4.3	Validation of the Coupled FEM-BEM Scheme . . . . .	64
3.4.4	Scattering by a Square . . . . .	65
3.4.5	Discussion . . . . .	68
<b>4</b>	<b>Coupled FEM-BEM Technique for Inhomogeneous Problems</b>	<b>69</b>
4.1	The Inhomogeneous Problem . . . . .	69
4.2	Formulation . . . . .	71
4.3	Evaluating the induced field . . . . .	73
4.4	Numerical Results . . . . .	75
4.4.1	Discussion . . . . .	83
<b>5</b>	<b>Inverse Medium Problem for Non-Stratified Media</b>	<b>84</b>
5.1	Logan-Shepp Polynomials . . . . .	87
5.2	Reformulating the Inverse Problem as a Discrete Nonlinear Equation	88
5.3	Numerical Results . . . . .	89
5.3.1	Discussion . . . . .	97
<b>6</b>	<b>Inverse Coated Problem</b>	<b>99</b>
6.1	Approximation Theory . . . . .	100
6.2	An analytic representation for the Fréchet derivative . . . . .	103
6.2.1	The <i>Lippmann-Schwinger</i> Equation . . . . .	103
6.3	Numerics . . . . .	107
6.3.1	Discussion . . . . .	115
<b>7</b>	<b>Discussion</b>	<b>118</b>
<b>8</b>	<b>Conclusion</b>	<b>122</b>
<b>9</b>	<b>Appendix</b>	<b>125</b>
9.1	Neumann Boundary Condition for TE Waves . . . . .	125

9.2	The Tikhonov Regularization Theorem . . . . .	127
9.3	Finite Element Calculations . . . . .	130
9.4	Derivation of the Integral Representation of the Far Field . . . . .	135
9.5	Radiating Wave Functions . . . . .	138
9.6	Orthogonal Polynomials . . . . .	140
9.6.1	Chebyshev polynomials . . . . .	140
9.6.2	Logan-Shepp polynomials . . . . .	141
9.7	Gaussian Quadrature . . . . .	144
9.8	Green's Theorems . . . . .	145
9.8.1	Green's Identities . . . . .	145
9.8.2	Green's Representation Formula . . . . .	145

# Chapter 1

## Introduction

The field of inverse scattering theory for acoustic and electromagnetic waves originated during World War II, with the invention of radar and sonar [20]. However, the field did not make any significant progress until the 1980's [15], making inverse scattering theory relatively underdeveloped despite its age [23]. The field has grown immensely in the last thirty years and today is one of the most active and important areas of research in mathematics [19], with diverse applications in disciplines such as medical imaging, materials science, nondestructive testing, radar, remote sensing and seismic explorations [86].

Inverse scattering theory is a vast field (see [23, 18, 57, 69, 70, 74, 79, 80, 82, 87] and references therein for an overview of the subject), whose main focus is to solve two problems: the inverse obstacle problem, and the inverse medium problem.

For both problems, an unknown obstacle is illuminated by an acoustic or electromagnetic wave and induces a scattered field. Using knowledge of the scattered field at some distance away from the obstacle, both problems seek to determine information about the obstacle. In the case of the inverse obstacle problem, the aim is to determine the *shape* of the obstacle. In the case of the inverse medium problem, the aim is to determine the *material properties* of the obstacle. In this thesis, we



present a novel numerical scheme to solve a particular inverse medium problem.

We begin in Section 1.1 by introducing our problem of interest. In Section 1.2 we give a brief review of the literature related to our problem. In Section 1.3 we give an outline of the thesis, highlighting which parts constitute our main contributions to the field.

## 1.1 Background

Our problem of interest is a two dimensional inverse medium problem, which arises in the acoustic and electromagnetic imaging of anisotropic media. In this section we explain how the problem arises in both acoustic and electromagnetic settings, before giving the formal statement of the problem.

Let  $P$  be an infinite impenetrable prism in  $\mathbb{R}^3$  running parallel to the  $z$ -axis, surrounded by a heterogeneous dielectric medium. We assume the the refractive index of the dielectric medium is constant outside the infinite unit cylinder  $C$ , so that the heterogeneity of the medium is contained within  $\Lambda := C \setminus \bar{P}$ . Furthermore, we denote the two-dimensional cross section of  $P$  and  $\Lambda$  as  $D$  and  $\Omega$  respectively (see Figure 1.1).

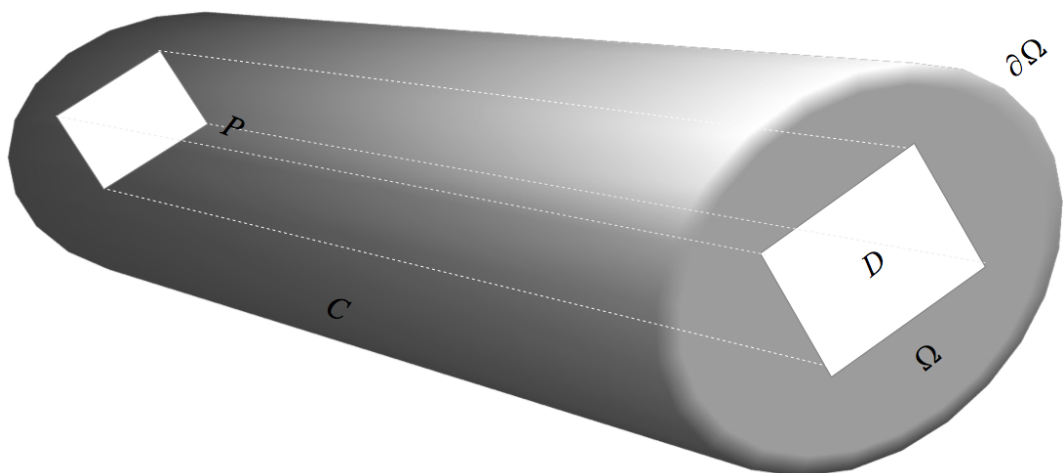


Figure 1.1: An infinite prism  $P$  with “dielectric coating”  $\Lambda$  running parallel to the  $z$ -axis, in the case where the cross-section  $D$  is a square.

## The Acoustic Case

Suppose  $\mathbb{R}^3 \setminus \bar{P}$  contains an inviscid fluid. When the scatterer  $P$  is illuminated by an *incident* wave  $u^{\text{inc}}$ , the boundary  $\partial P$  of  $P$  together with the heterogeneous media within  $\Lambda$  induce a *scattered field*  $u^s$  in  $\mathbb{R}^3 \setminus C$ , and an *induced field*  $u^i$  in  $\Lambda$ . The fields  $u^s$  and  $u^i$  must satisfy the homogeneous and heterogeneous Helmholtz equations respectively.

We start by considering the propagation of acoustic waves in  $\mathbb{R}^3 \setminus \bar{P}$ . Let  $v' = v'(\mathbf{x}, t)$  be the velocity field,  $p' = p'(\mathbf{x}, t)$  be the pressure,  $\rho' = \rho'(\mathbf{x}, t)$  be the density, and  $S' = S'(\mathbf{x}, t)$  be the entropy of the fluid at point  $\mathbf{x}$  and time  $t$ , where  $\mathbf{x} \in \mathbb{R}^3 \setminus \bar{P}$ .

For such a fluid, the conservation of momentum law is expressed as

$$\frac{\partial v'}{\partial t} + v' \cdot \nabla v' + \frac{1}{\rho'} \nabla p' = 0. \quad (1.1)$$

Here gravity and other external forces are ignored. The conservation of mass law is expressed as

$$\frac{\partial \rho'}{\partial t} + \nabla \cdot \rho v' = 0. \quad (1.2)$$

Assuming the system is in local thermodynamic equilibrium, the state equation

$$p' = f(\rho', S') \quad (1.3)$$

will also hold, where the function  $f$  depends on the nature of the fluid. Following [23], we assume  $(v, p, \rho, S)$  is a small perturbation of the static state  $(v_0, p_0, \rho_0, S_0)$ , where  $v_0 = 0$  and  $p_0, \rho_0, S_0$  are constant. That is,

$$v' = v, p' = p_0 + p, \rho' = \rho_0 + \rho, S' = S_0 + S, \quad (1.4)$$

where  $v$  is a small acoustic wave perturbation,  $\rho$  is a small perturbation in the

density,  $p$  is a small perturbation in the in the pressure and  $S$  is a small perturbation in the entropy. Substituting (1.4) into (1.1)–(1.2) yields:

$$\frac{\partial v}{\partial t} + v \cdot \nabla v + \frac{1}{\rho_0 + \rho} \nabla(p_0 + p) = 0, \quad (1.5)$$

$$\frac{\partial(\rho_0 + \rho)}{\partial t} + \nabla \cdot ((\rho_0 + \rho)v) = 0. \quad (1.6)$$

Expanding  $p$  in a Taylor series in  $\rho$  gives an expansion of the form:

$$p = \left( \frac{\partial p}{\partial \rho} \right) \Big|_{\rho=0} + \frac{1}{2} \left( \frac{\partial^2 p}{\partial \rho^2} \right) \Big|_{\rho=0} \rho^2 + \dots \quad (1.7)$$

Substituting (1.7) into (1.5)–(1.6) and truncating to first order gives the following linear acoustic equations:

$$\frac{\partial v}{\partial t} + \frac{1}{\rho_0} \nabla p = 0, \quad (1.8)$$

$$\frac{\partial \rho}{\partial t} + \rho_0 (\nabla \cdot v) = 0, \quad (1.9)$$

$$\frac{\partial p}{\partial t} = c^2 \frac{\partial \rho}{\partial t}, \quad (1.10)$$

where the speed of sound  $c$  in the medium satisfies

$$c^2 = \frac{\partial f}{\partial \rho}(\rho_0, S_0).$$

To derive the wave equation we begin by taking the curl of (1.8):

$$\nabla \times \left( \frac{\partial v}{\partial t} + \frac{1}{\rho_0} \nabla p \right) = 0. \quad (1.11)$$

Noting the identity  $\nabla \times \nabla p = 0$ , we deduce from (1.11) that

$$\frac{\partial}{\partial t} (\nabla \times v) = 0.$$

That is,  $\nabla \times v$  is constant in time. Assuming the velocity field is irrational initially,

this implies  $\nabla \times v = 0$  and hence

$$v = \nabla \mathcal{U}, \quad (1.12)$$

for some velocity potential  $\mathcal{U}$ . Therefore (1.9) becomes

$$\frac{\partial \rho}{\partial t} + \rho_0(\nabla \cdot \nabla \mathcal{U}) = 0.$$

That is,

$$\frac{\partial \rho}{\partial t} + \rho_0 \Delta \mathcal{U} = 0,$$

and hence

$$\rho_0 \Delta \mathcal{U} + \frac{1}{c^2} \frac{\partial p}{\partial t} = 0 \quad (1.13)$$

by (1.10). Now substituting (1.12) into (1.8) yields

$$\frac{\partial}{\partial t}(\nabla \mathcal{U}) + \frac{1}{\rho_0} \nabla p = 0,$$

which implies

$$p = -\rho_0 \frac{\partial \mathcal{U}}{\partial t} + K(t),$$

for some  $K(t)$ . Assuming  $K(t)$  is constant, (1.13) becomes

$$\rho_0 \Delta \mathcal{U} - \frac{\rho_0}{c^2} \frac{\partial^2 \mathcal{U}}{\partial t^2} = 0,$$

which simplifies to the wave equation in terms of the velocity potential:

$$\frac{1}{c^2} \frac{\partial^2 \mathcal{U}}{\partial t^2} - \Delta \mathcal{U} = 0. \quad (1.14)$$

For time-harmonic waves, we express  $\mathcal{U}$  as

$$\mathcal{U}(\mathbf{x}, t) = U(\mathbf{x})e^{-i\omega t},$$

where  $\omega$  is the angular frequency of the wave and the spatial component  $U$  is independent of the time variable  $t$ . Substituting back into the wave equation (1.14), the spatial component  $U$  satisfies the 3D Helmholtz equation:

$$\Delta U(\mathbf{x}) + k^2(\mathbf{x})U(\mathbf{x}) = 0 \quad \text{for } \mathbf{x} \in \mathbb{R}^3 \setminus \bar{P}, \quad (1.15)$$

where  $k(\mathbf{x}) = \frac{\omega}{c}$  is the wavenumber.

In our problem of interest, we are going to assume independency of  $U$  in the  $z$ -direction so that

$$U(x, y, z) = u^s(x, y), \quad (1.16)$$

Substituting (1.16) into (1.15) implies  $u^s$  satisfies the 2D Helmholtz equation

$$\Delta u^s(\mathbf{x}) + k^2(\mathbf{x})u^s(\mathbf{x}) = 0 \quad \text{for } \mathbf{x} \in \mathbb{R}^2 \setminus \bar{D}, \quad (1.17)$$

where recall  $D$  is the cross section of  $P$ . In this thesis, it is convenient to write the effective wavenumber  $k(\mathbf{x})$  as  $n(\mathbf{x})k$  where  $k$  is a constant and  $n(\mathbf{x})$  is the spatial dependent refractive index. Our assumption that  $k$  is constant is a reasonable and common assumption to make as both absorbing and dissipative media satisfy this assumption. It follows

$$\Delta u^s(\mathbf{x}) + k^2 n(\mathbf{x})u^s(\mathbf{x}) = 0 \quad \text{for } \mathbf{x} \in \mathbb{R}^2 \setminus \bar{D}. \quad (1.18)$$

Note that in the above equation the heterogeneity is contained within the cross-section  $B$  of the cylinder  $C$ , where  $B = \{(x, y) \in \mathbb{R}^2 : x^2 + y^2 < 1\}$  denotes the open

unit disk. We therefore normalize the refractive index function so that

$$n(\mathbf{x}) = 1 \quad \text{for} \quad \mathbf{x} \in \mathbb{R}^2 \setminus B.$$

It follows that for  $\mathbf{x} \in \mathbb{R}^2 \setminus B$ ,  $u^s$  satisfies the homogeneous 2D Helmholtz equation

$$\Delta u^s(\mathbf{x}) + k^2 u^s(\mathbf{x}) = 0.$$

Thus when  $P$  is illuminated by an incident plane wave  $u^{\text{inc}}$ , the behaviour of the *total field*

$$u(\mathbf{x}) = \begin{cases} u^i(\mathbf{x}), & \mathbf{x} \in \Omega, \\ u^{\text{inc}}(\mathbf{x}) + u^s(\mathbf{x}), & \mathbf{x} \in \mathbb{R}^2 \setminus B, \end{cases} \quad (1.19)$$

is governed by the *heterogeneous* Helmholtz equation (1.18), where we assume  $n(\mathbf{x})$  to be bounded and piecewise-continuous in the cross section  $\Omega$  of  $\Lambda$ .

In addition to equation (1.18),  $u$  will also satisfy a boundary condition on the boundary  $\partial D$  of  $D$ . If  $P$  is a *sound-soft* obstacle, then the pressure of the total wave will vanish on the boundary i.e.  $u$  will satisfy a Dirichlet boundary condition

$$u = 0 \quad \text{on} \quad \partial D. \quad (1.20)$$

If  $P$  is a *sound-hard* obstacle, then the normal velocity of the acoustic wave will vanish on the boundary i.e.  $u$  will satisfy a Neumann boundary condition

$$\frac{\partial u}{\partial \mathbf{n}} = 0 \quad \text{on} \quad \partial D, \quad (1.21)$$

where  $\mathbf{n}$  is the unit outward normal to  $\partial D$ . A third possibility is that the normal velocity on the boundary is proportional to the excess pressure on the boundary. In

that case,  $u$  will satisfy a *Robin* boundary condition on  $\partial D$ :

$$\frac{\partial u}{\partial \mathbf{n}} + iku = 0 \quad (1.22)$$

To ensure uniqueness of the solution, we also require that the scattered component  $u^s$  satisfies the *Sommerfeld radiation condition*:

$$\lim_{r \rightarrow \infty} \sqrt{r} \left( \frac{\partial u^s}{\partial r} - iku^s \right) = 0, \quad r = |\mathbf{x}|, \quad (1.23)$$

uniformly for all  $\mathbf{x}$ . The *forward scattering problem* in the acoustic case is to compute the total field (1.19) that satisfies the Helmholtz Equation (1.18), the Sommerfeld radiation condition and a given boundary condition, from knowledge of the refractive index  $n(\mathbf{x})$ . Note that we require the total field and its normal derivative to be continuous across the boundary  $\partial B$  of  $B$ , to ensure continuity of the pressure and of the normal velocity across the interface.

## The Electromagnetic Case

We now show how the same forward scattering problem arises in the setting of electromagnetic waves.

Suppose  $\Gamma$  represents a homogeneous dielectric medium. The behaviour of electric and magnetic fields in  $\Gamma$  are governed by Maxwell's equations:

$$\nabla \times \mathbf{E} = -\frac{\partial \mathbf{B}}{\partial t}, \quad (1.24)$$

$$\nabla \cdot \mathbf{B} = 0, \quad (1.25)$$

$$\nabla \times \mathbf{H} = \frac{\partial \mathbf{D}}{\partial t}, \quad (1.26)$$

$$\nabla \cdot \mathbf{D} = 0, \quad (1.27)$$

where  $\mathbf{E}$  is the electric intensity,  $\mathbf{B}$  is the magnetic flux density,  $\mathbf{H}$  is the magnetic

intensity and  $\mathbf{D}$  is the electric flux density.

The complex form of the electric intensity  $\mathbf{E}$ , is related to the instantaneous form of the electric intensity  $\mathbf{E}$ , by:

$$\mathbf{E}(\mathbf{x}, t) = \text{Re}(\mathbf{E}(\mathbf{x})e^{i\omega t}). \quad (1.28)$$

The other instantaneous quantities  $\mathbf{B}$ ,  $\mathbf{H}$  and  $\mathbf{D}$  are related in a similar way to their corresponding complex quantities  $\mathbf{B}, \mathbf{H}, \mathbf{D}$ . These relations can be used to derive the complex form of Maxwell's equations. For instance, substituting (1.28) into (1.24), we have

$$\nabla \times [\text{Re}(\mathbf{E}e^{i\omega t})] = -\frac{\partial}{\partial t}[\text{Re}(\mathbf{B}e^{i\omega t})], \quad (1.29)$$

which means

$$\text{Re}(\nabla \times \mathbf{E}e^{i\omega t}) = -\text{Re}(i\omega \mathbf{B}e^{i\omega t}). \quad (1.30)$$

Since this holds for all  $t$ , we get:

$$\nabla \times \mathbf{E} = -i\omega \mathbf{B}. \quad (1.31)$$

Similarly, it is straightforward to derive

$$\nabla \times \mathbf{H} = i\omega \mathbf{D}, \quad (1.32)$$

as well as  $\nabla \cdot \mathbf{D} = 0$  and  $\nabla \cdot \mathbf{B} = 0$ . These variables are related to each other via the equations [51, Page 18]:

$$\mathbf{D} = \hat{\epsilon} \mathbf{E}, \quad (1.33)$$

$$\mathbf{B} = \hat{\mu} \mathbf{H}, \quad (1.34)$$



where  $\hat{\epsilon}$  is called the electric permittivity of the medium and  $\hat{\mu}$  is called the magnetic permeability of the medium. These are constants which specify the characteristics of the media. Substituting (1.34) into (1.31) and (1.33) into (1.32), we get the reduced Maxwell equations:

$$\nabla \times \mathbf{E} = -i\omega\hat{\mu}\mathbf{H}, \quad (1.35)$$

$$\nabla \times \mathbf{H} = i\omega\hat{\epsilon}\mathbf{E}. \quad (1.36)$$

Taking the curl of (1.35) on both sides, we have

$$\nabla \times \nabla \times \mathbf{E} = -i\omega\hat{\mu}\nabla \times \mathbf{H}. \quad (1.37)$$

Substituting (1.36) into (1.37), we get

$$\nabla \times \nabla \times \mathbf{E} = \omega^2\hat{\epsilon}\hat{\mu}\mathbf{E}. \quad (1.38)$$

Defining the wavenumber  $k = \sqrt{\omega^2\hat{\epsilon}\hat{\mu}}$ , (1.38) becomes:

$$\nabla \times \nabla \times \mathbf{E} - k^2\mathbf{E} = \mathbf{0}. \quad (1.39)$$

Applying the same series of steps to (1.36), we obtain

$$\nabla \times \nabla \times \mathbf{H} - k^2\mathbf{H} = \mathbf{0}. \quad (1.40)$$

Furthermore, we have

$$\nabla \cdot \mathbf{E} = 0 \quad \text{and} \quad \nabla \cdot \mathbf{H} = 0, \quad (1.41)$$

by taking the divergence of (1.39) and (1.40). Using the identity

$$\triangle \mathbf{A} = \nabla(\nabla \cdot \mathbf{A}) - \nabla \times \nabla \times \mathbf{A} \quad (1.42)$$

which holds for any arbitrary vector  $\mathbf{A}$ , we can write (1.39) and (1.40) as

$$\Delta \mathbf{E} + k^2 \mathbf{E} = \mathbf{0} \quad \text{and} \quad \Delta \mathbf{H} + k^2 \mathbf{H} = \mathbf{0}. \quad (1.43)$$

It follows that equations (1.41) and (1.43) combined are the equivalent of equations (1.39) and (1.40). So consider the system of equations:

$$\Delta \mathbf{H} + k^2 \mathbf{H} = \mathbf{0}, \quad (1.44)$$

$$\nabla \cdot \mathbf{H} = 0. \quad (1.45)$$

Since the divergence of  $\mathbf{H}$  is zero,  $\mathbf{H}$  must be the curl of some other vector,

$$\text{i.e. } \mathbf{H} = \nabla \times \mathbf{A}, \quad (1.46)$$

where  $\mathbf{A}$  is the magnetic vector potential. Substituting the above into (1.35), we obtain

$$\nabla \times (\mathbf{E} + i\omega \hat{\mu} \mathbf{A}) = \mathbf{0}. \quad (1.47)$$

Since the curl of  $(\mathbf{E} + i\omega \hat{\mu} \mathbf{A})$  is zero, it must be the gradient of some scalar,

$$\text{i.e. } \mathbf{E} + i\omega \hat{\mu} \mathbf{A} = -\nabla \Phi^a, \quad (1.48)$$

where  $\Phi^a$  is an arbitrary electric scalar potential. Substituting (1.46) and (1.48) into (1.36) gives

$$\nabla \times \nabla \times \mathbf{A} = i\omega \hat{\epsilon} (-\nabla \Phi^a - i\omega \hat{\mu} \mathbf{A}) \quad (1.49)$$

$$= -i\omega \hat{\epsilon} \nabla \Phi^a + k^2 \mathbf{A}. \quad (1.50)$$

$$\text{i.e. } \nabla \times \nabla \times \mathbf{A} - k^2 \mathbf{A} = -i\omega \hat{\epsilon} \nabla \Phi^a. \quad (1.51)$$

Next, we apply the same series of steps to the system

$$\Delta \mathbf{E} + k^2 \mathbf{E} = \mathbf{0}, \quad (1.52)$$

$$\nabla \cdot \mathbf{E} = 0. \quad (1.53)$$

Since the divergence of  $\mathbf{E}$  is zero,  $\mathbf{E}$  must be the curl of some other vector,

$$\text{i.e. } \mathbf{E} = -\nabla \times \mathbf{F}, \quad (1.54)$$

where  $\mathbf{F}$  is the electric vector potential. Using a similar method to before, we obtain

$$\nabla \times \nabla \times \mathbf{F} - k^2 \mathbf{F} = -i\omega\hat{\epsilon}\nabla\Phi^f, \quad (1.55)$$

where  $\Phi^f$  is a magnetic vector potential. But note that the scalar fields  $\Phi^a$  and  $\Phi^f$  were arbitrarily chosen. If we pick our scalars such that

$$\nabla \cdot \mathbf{A} = -i\omega\hat{\epsilon}\Phi^a, \quad (1.56)$$

$$\nabla \cdot \mathbf{F} = -i\omega\hat{\mu}\Phi^f, \quad (1.57)$$

then equations (1.51) and (1.55) reduce to

$$\Delta \mathbf{A} + k^2 \mathbf{A} = \mathbf{0}, \quad (1.58)$$

$$\Delta \mathbf{F} + k^2 \mathbf{F} = \mathbf{0}. \quad (1.59)$$

Now, note from (1.35)–(1.36),

$$\mathbf{E} = \frac{1}{i\omega\hat{\epsilon}}\nabla \times \mathbf{H}, \quad (1.60)$$

$$\mathbf{H} = -\frac{1}{i\omega\hat{\mu}}\nabla \times \mathbf{E}. \quad (1.61)$$

We then have

$$\mathbf{E} = \frac{1}{i\omega\hat{\epsilon}} \nabla \times \nabla \times \mathbf{A}, \quad (1.62)$$

$$\mathbf{H} = -\frac{1}{i\omega\hat{\mu}} \nabla \times \nabla \times \mathbf{F}, \quad (1.63)$$

using (1.46) and (1.54). Notice that these are valid solutions of Maxwell's equations, along with equations (1.46) and (1.54). In general, a solution to Maxwells equations is a linear combination of both types of solutions. That is [51, page 99],

$$\mathbf{E} = -\nabla \times \mathbf{F} + \frac{1}{i\omega\hat{\epsilon}} \nabla \times \nabla \times \mathbf{A}, \quad (1.64)$$

$$\mathbf{H} = \nabla \times \mathbf{A} - \frac{1}{i\omega\hat{\mu}} \nabla \times \nabla \times \mathbf{F}. \quad (1.65)$$

Now suppose we choose  $\mathbf{A}$  and  $\mathbf{F}$  to be of the form:

$$\mathbf{A} = \mathbf{c}\psi^a,$$

$$\mathbf{F} = \mathbf{c}\psi^f,$$

where  $\mathbf{c}$  is a constant vector. Then  $\mathbf{A}$  and  $\mathbf{F}$  will satisfy the vector Helmholtz equations (1.58)–(1.59) if and only if  $\psi^a$  and  $\psi^f$  satisfy the scalar Helmholtz equations. That is,

$$\Delta\psi^a + k^2\psi^a = 0, \quad (1.66)$$

$$\Delta\psi^f + k^2\psi^f = 0. \quad (1.67)$$

Now recall that  $\Gamma$  represents any arbitrary homogeneous medium. It therefore follows that much like the acoustic case, electromagnetic waves satisfy the homogeneous Helmholtz equation in  $\mathbb{R}^3 \setminus C$ . Within the dielectric coating  $\Lambda$  however, they will of course satisfy the inhomogeneous Helmholtz equation instead, due to the presence of a varying refractive index.

Also, the same boundary conditions mentioned in the acoustic case reappear in the electromagnetic setting. Following [51, page 130], we consider two main types of electromagnetic waves: waves that are *transverse magnetic* to  $z$  (TM waves), and waves that are *transverse electric* to  $z$  (TE waves).

TM waves arise in the special case where  $\mathbf{c} = (0, 0, 1)$  and  $\psi^f = 0$ . In that case, the components of  $\mathbf{E}$  become:

$$\mathbf{E}_x = \frac{1}{i\omega\epsilon} \frac{\partial^2 \psi^a}{\partial x \partial z}, \quad (1.68)$$

$$\mathbf{E}_y = \frac{1}{i\omega\epsilon} \frac{\partial^2 \psi^a}{\partial y \partial z}, \quad (1.69)$$

$$\mathbf{E}_z = \frac{1}{i\omega\epsilon} \left( \frac{\partial^2}{\partial z^2} + k^2 \right) \psi^a. \quad (1.70)$$

Assuming  $\psi^a$  is independent of  $z$ , we get  $\mathbf{E} = (0, 0, \frac{k^2}{i\omega\epsilon} \psi^a)$ . Enforcing the boundary condition  $\mathbf{n} \times \mathbf{E} = 0$  where  $\mathbf{n} = (n_1, n_2, n_3)$  is the outward pointing unit normal on  $\partial P$ , we get

$$\frac{k^2}{i\omega\epsilon} (n_2 \psi^a, n_1 \psi^a, 0) = 0,$$

which implies

$$\psi^a = 0$$

on the boundary  $\partial P$  of  $P$ . That is, TM waves lead to a Dirichlet boundary condition.

It can be similarly shown that TE waves lead to a Neumann boundary condition (see Section 9.1).

To ensure uniqueness of the solutions, we require the scattered components  $\mathbf{E}^s$  and  $\mathbf{H}^s$  of  $\mathbf{E}$  and  $\mathbf{H}$  to satisfy the *Silver-Müller* radiation conditions [23, p. 3]

$$\lim_{r \rightarrow \infty} (\mathbf{H}^s \times \mathbf{x} - r \mathbf{E}^s) = \mathbf{0},$$

$$\lim_{r \rightarrow \infty} (\mathbf{E}^s \times \mathbf{x} + r \mathbf{H}^s) = \mathbf{0},$$

which are equivalent [23, Theorem 6.8] to the Sommerfeld radiation condition for the Cartesian components:

$$\begin{aligned}\lim_{r \rightarrow \infty} \sqrt{r} \left( \frac{\partial \mathbf{E}^s}{\partial r} - ik \mathbf{E}^s \right) &= 0, \\ \lim_{r \rightarrow \infty} \sqrt{r} \left( \frac{\partial \mathbf{H}^s}{\partial r} - ik \mathbf{H}^s \right) &= 0,\end{aligned}$$

with  $r = |\mathbf{x}|$ .

## Statement of the Problem

We see that in both the acoustic and electromagnetic setting, the same 2D boundary value problem arises. Given knowledge of the incident field  $u^{\text{inc}}$  and the refractive index  $n(\mathbf{x})$  in  $\Omega$ , we seek to find the total field

$$u(\mathbf{x}) = \begin{cases} u^i(\mathbf{x}), & \mathbf{x} \in \Omega, \\ u^{\text{inc}}(\mathbf{x}) + u^s(\mathbf{x}), & \mathbf{x} \in \mathbb{R}^2 \setminus B \end{cases} \quad (1.71)$$

which satisfies

$$\Delta u(\mathbf{x}) + k^2 n(\mathbf{x}) u(\mathbf{x}) = 0 \quad \text{for } \mathbf{x} \in \mathbb{R}^2 \setminus \bar{D}, \quad (1.72)$$

the Sommerfeld radiation condition

$$\lim_{r \rightarrow \infty} \sqrt{r} \left( \frac{\partial u^s}{\partial r} - ik u^s \right) = 0, \quad r = |\mathbf{x}|, \quad (1.73)$$

and a boundary condition of the form

$$\mathcal{B}u(\mathbf{x}) = f(\mathbf{x}) \quad \text{on } \partial D, \quad (1.74)$$

where  $\mathcal{B}u(\mathbf{x}) = f(\mathbf{x})$  can represent a Dirichlet, Neumann or Robin boundary condition. In particular, we seek to compute the far field of the scattered wave

$$u_\infty(\hat{\mathbf{x}}) = \lim_{|\mathbf{x}| \rightarrow \infty} \sqrt{|\mathbf{x}|} e^{-ik|\mathbf{x}|} u^s(\mathbf{x}) \quad (1.75)$$

for fixed  $k$ , where  $\hat{\mathbf{x}} = \mathbf{x}/|\mathbf{x}|$ .

We refer to this problem as the *forward medium problem*. In this thesis, we solve the inverse of this problem i.e. determining the refractive index  $n(\mathbf{x})$  from knowledge of  $u_\infty$ . We have referred to this problem in the thesis as the *Inverse Coated Problem*, in the case where the obstacle  $D$  is situated in the middle of  $\Omega$ . Solving this problem poses several major challenges, as the problem is nonlinear and improperly posed; small perturbations of the far field pattern lead to large errors in the reconstruction of  $n(\mathbf{x})$ . Moreover, our method of solution for the inverse problem requires solving the forward problem, which in itself is quite hard and requires innovation.

## 1.2 Review of the Literature

In the literature, the problem of determining the refractive index  $n$  from knowledge of the far field is referred to as the inverse medium problem. Approaches to solving the inverse medium problem fall under three categories: decomposition methods, sampling methods and nonlinear optimization techniques. As far as we are aware, the Inverse Coated Problem has yet to be considered in the literature; these three methods of solution have instead been applied to the instances of the inverse medium problem where the obstacle  $D$  is absent.

There are two versions of the decomposition method. In the first version [28], the inverse medium problem is reformulated as solving a series of boundary integrals equations relating the far field to spherical harmonics. In the second version [26, 29] these integral equations are modified to avoid transmission eigenvalues. These two

versions have been compared numerically in [24], and further modifications of the decomposition method have been discussed in [21, 27, 25].

Sampling methods [16, 17, 59] require less a priori information than the other two methods, and reduce the nonlinear problem to a series of linear problems. However their numerical implementation requires more data than the other techniques and can only provide a rough estimate of the material properties of the medium.

The third method is based on noting [23] that

$$u_\infty(\hat{\mathbf{x}}) = -\frac{k^2}{4\pi} \int_{\mathbb{R}^2 \setminus \bar{D}} e^{-ik\hat{\mathbf{x}} \cdot \mathbf{y}} m(\mathbf{y}) u(\mathbf{y}) d\mathbf{y}, \quad \hat{\mathbf{x}} = \frac{\mathbf{x}}{|\mathbf{x}|}, \quad (1.76)$$

where  $m = 1 - n$ .

Then the inverse problem is reformulated as a nonlinear optimization problem in which we seek to solve the *Lippmann-Schwinger* volume integral equations while ensuring the constraint (1.76) is satisfied (we discuss these equations thoroughly in Section 6.2.1). This approach has been utilised in solving the inverse medium problem for both the acoustic and electromagnetic case [10, 63, 64, 2]. However the manner in which this approach is implemented varies in the literature. For instance, (1.76) is at times replaced by a near-field condition, and the optimization scheme has been numerically solved using different methods, including successive over-relaxation, sinc basis methods, steepest descent and Newton's method.

Our approach for solving the inverse medium problem in this thesis is the third method. However, our approach is novel in that instead of solving the *Lippmann-Schwinger* equations, we solve the forward problem (1.72)–(1.74) while ensuring the constraint (1.76) is satisfied. We then solve the optimization scheme using an iterative Newton-type solver. In [7], we solved the Inverse Coated Problem in the special case where the obstacle  $D$  was absent. Unlike other articles in the literature, in [7] we did not assume any radial symmetry regarding the refractive index  $n$ . In Chapter 5 we revisit this problem and improve on the results already published in [7]. We



then solve the Inverse Coated Problem in its full generality in Chapter 6, which has yet to be considered in the literature.

Our choice of solution method for the inverse problem requires us to solve repeated iterations of the forward problem. Two common approaches for solving such boundary value problems are finite element methods (FEMs) and boundary element methods (BEMs).

FEMs can solve PDEs over complex geometries, and are suitable for both homogeneous and heterogeneous problems. However FEMs cannot be applied when solving (1.72)–(1.74) because they are only applicable to problems over bounded regions. An adaptation of the FEM is the *expanding grids* technique [42, 65], in which the unbounded domain is approximated by a large bounded domain, and the Sommerfeld radiation condition (1.73) is replaced by an appropriate boundary condition on the outer boundary. But because the FEM depends on using a fixed number of elements per wavelength in the FEM mesh [31, 72, 73], the expanding grids technique leads to solving a large linear system. Furthermore, this approach does not provide a direct approximation to the far field pattern of the scattered wave [60].

BEMs reformulate PDEs in terms of boundary integral equations, making discretization only necessary over the boundary. They are an efficient technique for solving homogeneous PDEs over unbounded regions and are particularly advantageous because they ensure the radiation condition (1.73) is satisfied exactly. However, BEMs cannot be solely used to solve the forward media problem (1.72)–(1.74) because they are not applicable to heterogeneous problems. Moreover, applying BEMs to problems with non-smooth boundaries requires innovation [66, 44, 54, 83], because standard BEMs require the boundary to be smooth.

In this thesis, we solve the forward problem (1.72)–(1.74) using the coupled FEM-BEM technique, which takes advantage of and facilitates the strengths of both approaches, while avoiding the disadvantages associated with each technique. We

apply a transmission boundary condition on  $\partial\Omega$  in a manner which splits the forward problem into two sub-problems: an exterior problem in  $\mathbb{R}^2 \setminus B$  and an interior problem in  $\Omega$ . This allows us to apply a BEM in  $\mathbb{R}^2 \setminus B$  while applying a FEM in  $\Omega$ . In this way, the radiation condition (1.73) is satisfied exactly, while the heterogeneous refractive index  $n(x)$  in  $\Omega$  and the non-smooth boundary  $\partial D$  are handled appropriately.

In [7], we solved the forward problem in each iteration of Newton's method using this method. As far as we are aware, we were the first in the literature to apply this approach to the forward problem. Since then, another article [39] has appeared in the literature which also solves the forward problem using the coupled FEM-BEM technique. The focus in [39] is rapid solution of the forward problem which they achieve using a high order FEM. We note that their high order FEM would also be applicable here using a similar approach to the one described in this thesis. Implementing a higher order FEM in our forward solver like in [39] would be a good idea for further research.

## 1.3 Thesis Outline

In this thesis, we reformulate the Inverse Coated Problem as a nonlinear operator equation, which we then solve using a regularized Newton-type solver. This solver requires solution of one or more forward problems in each iteration.

In Chapter 2 we discuss the preliminaries and background knowledge necessary for the comprehension of later chapters of the thesis. We begin with a summary of relevant results on function spaces, and then outline the relevant theory on inverse problems. In particular, because the inverse problem is ill-posed and requires regularization, we describe the regularization technique that we employ. We also include a summary of the basic notational and variable definitions used throughout the thesis, which can be readily referred to for the reader's convenience.

In Chapter 3 we describe solution of the forward medium problem, using the coupled FEM-BEM technique. We begin Chapter 3 by motivating the coupled FEM-BEM technique, before detailing how to apply the coupled FEM-BEM technique to solve the forward problem. Although the coupled FEM-BEM technique was first described in [60], we believe we are the first to implement it. Note that the results in [60] are not for the FEM-BEM technique; they use the Mie-series for the exterior rather than the BEM by considering the special case where  $D$  is a circle. Also note that [39] does indeed have an implementation of the coupled FEM-BEM technique. But this was written independently at the same time as our paper [7], which [39] itself cites.

The iterative solver also requires computing a Fréchet derivative in each iteration. We will see in Chapters 5 and 6 of the thesis that computing this Fréchet derivative involves solving a particular inhomogeneous boundary value problem. In Chapter 4 we develop a novel extension of the coupled FEM-BEM scheme for this inhomogeneous boundary value problem and numerically demonstrate its effectiveness.

In Chapter 5 we consider a special case of the Inverse Coated Problem where the impenetrable scatterer  $D$  is absent i.e.  $\Omega$  is the open unit disk. Similar problems have been considered in the literature with symmetry assumptions on the refractive index that simplify the problem considerably. Here we do not assume the refractive  $n(\mathbf{x})$  in  $\Omega$  to possess any form of symmetry. In a preliminary work [7] we numerically solved this problem computing the Fréchet derivative using the method of finite-differences. In Chapter 5 we present an improved approach that computes the Fréchet derivative as the solution of an inhomogeneous boundary value problem using the method in Chapter 4. Computing the Fréchet derivative in this way drastically reduces the CPU time which in turn leads to far better numerical results compared to those accomplished in [7]. A full comparison of these results is provided in Chapter 5.

In Chapter 6 we consider the case where  $D \neq \emptyset$ . This is more difficult than the case where  $D = \emptyset$  for several reasons. Firstly, there are no results in the literature that give an analytic expression for the Fréchet derivative for a medium exterior to

an impenetrable scatterer. In Chapter 6 we establish an analytic expression for the Fréchet derivative as the solution of an inhomogeneous boundary value problem, analogous to the result when  $D = \emptyset$ . Secondly, the refractive index must be approximated in an annular region (possibly with Lipschitz boundary) and there is no natural approximation space analogous to the Logan-Shepp polynomials employed in Chapter 5. We obtain a suitable approximation space by introducing a bijective mapping from the annular region to a suitable reference domain on which a high order orthogonal basis is available. As in Chapter 5 we solve the inhomogeneous boundary value problem using the novel coupled FEM-BEM scheme we described in Chapter 6. Numerical results demonstrate the capability of this approach for reconstructing various challenging heterogeneous media surrounding cylinders of circular or square cross section.

# Chapter 2

## Preliminaries

In this chapter, we first give a summary in Section 2.1 of the results from the theory of function spaces used throughout this thesis. Then in Section 2.2 we outline the relevant theory of inverse problems used in Chapters 5–6. In Section 2.3 we construct the *Angular-Legendre* polynomials, which will be use in Chapter 6. We then conclude the chapter by tabulating the basic notational and variable definitions used throughout the thesis, for the reader’s convenience.

### 2.1 Function Spaces

Throughout this section we suppose  $(S, d\mu)$  is a measure space for some domain (i.e. open, bounded and connected)  $S \subset \mathbb{R}^2$ .

#### Spaces of Continuous Functions

The space of all continuous functions on  $S$  is denoted as  $C(S)$ ; it is a vector space under the usual addition and scalar multiplication operations for functions.  $C(\bar{S})$  denotes the space of continuous functions on the closure  $\bar{S}$  of  $S$ . For  $j \in \mathbb{Z}^+$ ,  $C^j(S)$

represents the set of all functions on  $S$  which are  $j$ -times continuously differentiable. Similarly  $C^j(\bar{S})$  is the set of all functions on the closure  $\bar{S}$  which are  $j$ -times continuously differentiable. We define

$$C^\infty(S) = \{v \in C(S) : v \in C^j(S) \text{ for all } j \in \mathbb{Z}^+\}.$$

That is,  $C^\infty(S)$  is the space of infinitely differentiable functions on  $S$ . For a function  $f$  on  $S$ , the *support* of  $f$  is defined as

$$\text{supp}(f) = \overline{\{\mathbf{x} \in S : f(\mathbf{x}) \neq 0\}}.$$

We then define  $C_c^\infty(S)$  to be the space of all infinitely differentiable functions with compact support in  $S$ .

## $L^p$ Spaces

Given  $1 \leq p < \infty$ , the space  $L^p(S)$  is defined as

$$L^p(S) = \{f : S \rightarrow \mathbb{R} \text{ measurable} \mid \|f\|_p < \infty\},$$

where

$$\|f\|_p = \left( \iint_S |f|^p d\mu \right)^{\frac{1}{p}}.$$

The function  $f : S \rightarrow \mathbb{R}$  is called *p-locally integrable* if

$$\iint_K |f|^p d\mu < \infty,$$

for all compact  $K \subset S$ . The set of all such functions is denoted as  $L_{\text{loc}}^p(S)$ :

$$L_{\text{loc}}^p(S) = \left\{ f : S \rightarrow \mathbb{R} \text{ measurable} \mid \iint_K |f|^p d\mu < \infty \text{ for all compact } K \subset S \right\}.$$

Clearly  $L^p(S)$  is contained in  $L^p_{\text{loc}}(S)$ .

**Theorem 2.1.1.**  $L^p(S)$  is a subspace of  $L^1_{\text{loc}}(S)$  for all  $p \geq 1$ , where  $S$  is an open subset of  $\mathbb{R}^2$ .

## Weak Derivatives

A two-dimensional *multi-index* is an ordered pair  $\alpha = (\alpha_1, \alpha_2)$  of non-negative integers. We define  $|\alpha| = \alpha_1 + \alpha_2$  and denote the  $\alpha$ -th order partial derivative of a function  $f$  as

$$\partial^\alpha f(\mathbf{x}) = \frac{\partial^{|\alpha|} f(\mathbf{x})}{\partial x_1^{\alpha_1} \partial x_2^{\alpha_2}} \quad \text{where } \mathbf{x} = (x_1, x_2).$$

Note that in the special case where  $\alpha = (0, 0)$ , we have  $\partial^\alpha f = f$ . We say the function  $f \in L^1_{\text{loc}}(S)$  has  $\alpha$ -th *weak derivative*  $f' \in L^1_{\text{loc}}(S)$  if

$$\iint_S f' \partial^\alpha \phi \, d\mu = (-1)^{|\alpha|} \iint_S f \phi \, d\mu$$

for all  $\phi \in C_c^\infty(S)$ . In this case we denote the weak derivative of  $f$  as  $f' := D^\alpha f$ .

## Sobolev Spaces of Natural Order

Suppose  $m \in \mathbb{N}$ ,  $1 \leq p \leq \infty$  and  $S$  is an open set in  $\mathbb{R}^2$ . The Sobolev space  $W^{m,p}$  is defined as

$$W^{m,p}(S) = \{f \in L^p(S) : D^\alpha f \in L^p(S) \text{ for all } |\alpha| \leq m\},$$

and is equipped with the following norm:

$$\|f\|_{W^{m,p}(S)} = \left( \sum_{|\alpha| \leq m} \|D^\alpha f\|_p^p \right)^{\frac{1}{p}}.$$

In the special case where  $p = 2$ , the Sobolev space  $W^{m,p}$  is a Hilbert space, and we write  $W^{m,2}(S) = H^m(S)$ . That is,

$$H^m(S) = \{f \in L^2(S) : D^\alpha f \in L^2(S) \text{ for all } |\alpha| \leq m\},$$

and

$$\|f\|_{H^m(S)} = \left( \sum_{|\alpha| \leq m} \|D^\alpha f\|_2^2 \right)^{\frac{1}{2}}. \quad (2.1)$$

The local Sobolev space (when  $p = 2$ ) is defined as

$$H_{\text{loc}}^m(S) = \{f \in L_{\text{loc}}^2(S) : D^\alpha f \in L_{\text{loc}}^2(S) \text{ for all } |\alpha| \leq m\}.$$

## Sobolev Spaces of Fractional Order

When  $m$  is a positive fraction, the Sobolev space is defined as

$$H^m(S) = \left\{ f \in H^{[m]}(S) : D^\alpha f \in L^2(S), \int_{\Omega \times \Omega} \frac{|f(\mathbf{x}) - f(\mathbf{y})|^2}{|\mathbf{x} - \mathbf{y}|^{2+2m-2[m]}} d\mu(\mathbf{x})d\mu(\mathbf{y}) < \infty \text{ for } |\alpha| \leq [m] \right\}.$$

The Sobolev space  $H^{-m}(S)$  is defined to be the dual space of  $H^m(S)$ .

## Trace Theorems

The following theorem is based on theorem 7.3.11 from [5, p. 298].

**Theorem 2.1.2.** *Assume  $S$  is a bounded open set with Lipschitz boundary<sup>1</sup>  $\Gamma$ . Then*

---

<sup>1</sup>That is,  $\Gamma$  is locally the graph of a Lipschitz continuous function. Examples include smooth boundaries and polygonal boundaries.



there exist unique bounded linear and surjective mappings

$$\gamma_0 : H^1(S) \rightarrow H^{\frac{1}{2}}(\Gamma)$$

$$\gamma_1 : H^1(S) \rightarrow H^{-\frac{1}{2}}(\Gamma)$$

such that  $\gamma_0 v = v|_{\Gamma}$  and  $\gamma_1 v = \frac{\partial v}{\partial \mathbf{n}}|_{\Gamma}$  when  $v \in H^1(S) \cap C^1(\bar{S})$ .

## Weak solution

The following definition follows from [5, p. 353].

**Definition 2.1.3.** Assume  $S$  is a bounded open set with Lipschitz boundary  $\Gamma$ . Then for  $f \in L^2(S), g \in L^2(\Gamma)$ , we define  $u$  to be a weak solution to the boundary value problem

$$\begin{aligned} \Delta u + k^2 u &= f, \\ \frac{\partial u}{\partial \mathbf{n}} + iku &= g, \end{aligned}$$

if  $u \in H^1(S)$  and

$$\iint_S \nabla v(\mathbf{x}) \cdot \nabla u(\mathbf{x}) - k^2 v(\mathbf{x}) u(\mathbf{x}) \, d\mathbf{x} = \int_{\Gamma} v(\mathbf{x}) (g(\mathbf{x}) - iku(\mathbf{x})) \, ds(\mathbf{x}) - \iint_S v(\mathbf{x}) f(\mathbf{x}) \, d\mathbf{x}$$

for all  $v \in H^1(S)$ .

## 2.2 Inverse Problem Theory

In Chapter 3 we describe a numerical method to solve the forward media problem. That is computing the far field  $u_{\infty}$  of the scattered wave  $u^s$ , given knowledge of the shape of  $D$  and the refractive index of medium i.e.  $n(\mathbf{x})$ .

There we assume the medium is homogeneous outside the unit disk  $B$ , so that the

heterogeneity of the medium is contained within  $\Omega := B \setminus \bar{D}$ . This lets us describe the refractive index by the function  $m(\mathbf{x}) := 1 - n(\mathbf{x})$ , which is advantageous because  $m$  has compact support.

Thus the forward problem is equivalent to computing  $\mathcal{F}(m)$ , where the operator  $\mathcal{F} : L^2(\Omega) \rightarrow L^2(\mathbb{S}^1)$  maps  $m$  to the corresponding far field  $u_\infty$  of the induced scattered wave  $u^s$ . That is,

$$[\mathcal{F}(m)](\hat{\mathbf{x}}) = \lim_{|\mathbf{x}| \rightarrow \infty} \sqrt{|\mathbf{x}|} e^{-ik|\mathbf{x}|} u^s(\mathbf{x}), \quad \hat{\mathbf{x}} = \mathbf{x}/|\mathbf{x}|.$$

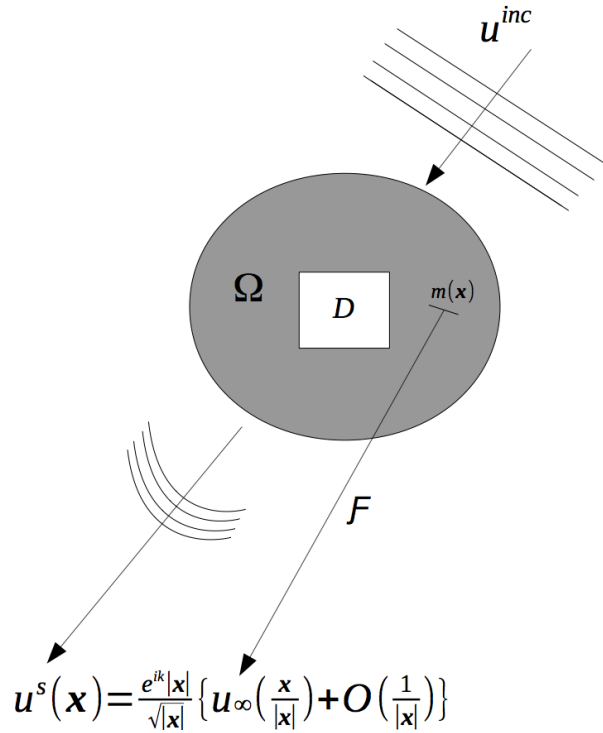


Figure 2.1: The incident wave  $u^{\text{inc}}$  interacts with the coated scatter  $D$  resulting in the scattered wave  $u^s$ . The operator  $\mathcal{F}$  maps the refractive index  $m$  in  $\Omega$  to the far field  $u_\infty$  of  $u^s$ .

In Chapters 5–6, we solve the corresponding inverse problem. That is, computing  $m(\mathbf{x})$  given the far field of the induced scattered wave. In both cases, the inverse problem equates to solving an equation of the form

$$\mathcal{F}(m) = f_\infty \quad (2.2)$$

for  $m$ , where  $f_\infty$  represents given far field data. Due to the differing nature of the two inverse problems, we use the notation  $\mathcal{F}_d$  for the operator in Chapter 5, and  $\mathcal{F}_c$  for the operator in Chapter 6. For the sake of generality, we describe the operator theory necessary to solve both inverse problems in terms of the operator  $\mathcal{F}$  in this chapter.

Note from [23, p. 277], the far field pattern can be expressed as

$$\mathcal{F}(m) = -\frac{k^2}{4\pi} \iint_{\mathbb{R}^2 \setminus \bar{D}} e^{-ik\mathbf{x} \cdot \mathbf{y}} m(\mathbf{y}) u(\mathbf{y}) d\mathbf{y},$$

which shows  $\mathcal{F}$  is completely continuous.

This can also be used to show  $\mathcal{F}$  is nonlinear. To see why, let  $u_n$  denote the solution to  $\Delta u + k^2 n u = 0$ , so that  $u_n$  is a function of  $n$ . Then note  $u_1 = H_0^{(1)}(kr)$  is a solution when  $n = 1$ , where  $H_0^{(1)}$  denotes the Hankel function of the first kind and order 0. If  $u$  was a linear function of  $n$ , then  $2u_1$  should be a solution for  $n = 4$ , which is not the case. We therefore deduce  $u$  is a nonlinear function of  $n$ , and consequently a nonlinear function of  $m$ .

Thus equation (2.2) is ill-posed by [23, Thm 4.2] and nonlinear. That is, the refractive index  $m$  in (2.2) does not depend continuously on the far field data  $f_\infty$ . Figure 2.2 illustrates a refractive index that does not continuously depend on far field data.

This is problematic because in practical applications the far field  $f_\infty$  is not known *exactly*, but includes noise. We label our data  $f_\infty^\delta$  (which may be a perturbation of the exact data) and assume there exists  $\delta > 0$  such that

$$\|f_\infty - f_\infty^\delta\|_{L^2(\mathbb{S}^1)} \leq \delta. \quad (2.3)$$

We then seek an approximate solution to (2.2) for a perturbed right hand side  $f_\infty^\delta$  with a known error level given by (2.3). For a perturbed right hand side, we cannot expect  $f_\infty^\delta \in \{\mathcal{F}(m) : m \in L^2(\Omega)\}$ . That is, we cannot expect  $f_\infty^\delta$  to lie in the range of  $\mathcal{F}$ . Using the data  $f_\infty^\delta$ , we then want to construct an approximation  $m^\delta$  close to the exact solution  $m$  of the unperturbed equation (2.2). Due to the ill-posed nature of the problem however, we cannot expect the error  $\|m - m^\delta\|_{L^2(\Omega)}$  between the true solution  $m$  and the approximate solution  $m^\delta$  to be small. Hence we require a *regularization strategy* to obtain a stabilized solution.

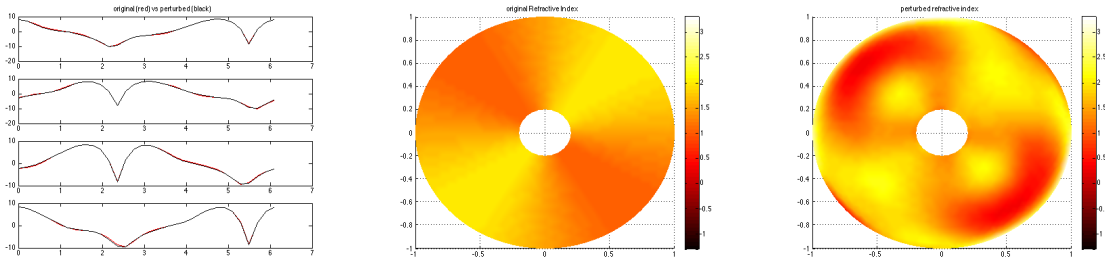


Figure 2.2: Visual example demonstrating the ill-posedness of (2.2). Visually the far field of  $f_\infty$  and  $f_\infty^\delta$  on the left are barely distinguishable, whereas the plot of  $m$  (center) and  $m^\delta$  (right) are clearly quite distinct.

A common approach to solving ill-posed nonlinear equations is the Levenburg-Marquardt scheme [58, 45, 50]. This is a regularized Newton-type solver, where the regularization is done according to Tikhonov's method (see Section 2.2.2), and the regularization parameter is chosen according to Morozov's discrepancy principle (see Section 2.2.3).

The Levenburg-Marquardt scheme is computationally practical because it provides a systematic way to choose the regularization parameter. For this reason, we equip the Levenburg-Marquardt scheme with our efficient forward solver to solve equations of the form (2.2) in Chapters 5–6.

### 2.2.1 Linearization

Given an approximate solution  $m^\delta$  to the exact solution  $m$  of the unperturbed equation (2.2), we seek an improved approximation  $m^\delta + q$  by solving the linearized equation

$$\mathcal{F}(m^\delta) + \mathcal{F}'(m^\delta)q = f_\infty^\delta \quad (2.4)$$

for  $q$ , where the Fréchet derivative  $\mathcal{F}'(m^\delta)$  of  $\mathcal{F}$  at  $m^\delta$  in the direction of  $d$  is defined by

$$\mathcal{F}'(m^\delta)d = \lim_{h \rightarrow 0} \frac{\mathcal{F}(m^\delta + hd) - \mathcal{F}(m^\delta)}{h},$$

and  $d$  is a function having compact support  $\Omega$ . In Chapters 5–6, we discretize (2.4) to obtain a linear system of the form

$$Fm^\delta + F'_m q^\delta = f^\delta.$$

Note by [23, Thm 4.21] that  $F'_m : \mathbb{R}^N \rightarrow \mathbb{R}^N$  is compact and equation (2.4) inherits the ill-posedness of equation (2.2); thus the discretized equation

$$F'_m q^\delta = f^\delta - Fm^\delta \quad (2.5)$$

is also ill-posed, and must be approached using a suitable regularisation strategy.

### 2.2.2 Tikhonov Regularization

A family of bounded linear operators  $\{R_\alpha\}_{\alpha>0}$ , with the property of pointwise convergence

$$\lim_{\alpha \rightarrow 0} R_\alpha F'_m q^\delta = q^\delta$$

for all  $q^\delta \in \mathbb{R}^N$  is called a regularization strategy for the operator  $F'_m$ . Moreover, the parameter  $\alpha$  is called the regularization parameter.

Tikhonov regularization is one type of regularization strategy, which is based on the following result [58, p. 38]:

**Theorem 2.2.1.** *Suppose  $F'_m$  is injective. Then for  $\alpha > 0$ , the operator  $\alpha I + (F'_m)^T F'_m$  is bounded and invertible, where  $I$  is the identity matrix and  $(F'_m)^T$  denotes the transpose of  $(F'_m)$ . The operators*

$$R_\alpha := [\alpha I + (F'_m)^T F'_m]^{-1} (F'_m)^T$$

*form a regularization strategy, called the Tikhonov regularization method.  $R_\alpha (f^\delta - Fm^\delta)$  is defined as the unique solution  $q^{\alpha,\delta}$  of the equation*

$$\alpha q^{\alpha,\delta} + (F'_m)^T F'_m q^{\alpha,\delta} = (F'_m)^T (f^\delta - Fm^\delta). \quad (2.6)$$

It follows from the above result that the regularized solution to (2.5) is given by

$$q^{\alpha,\delta} = [\alpha I + (F'_m)^T F'_m]^{-1} (F'_m)^T (f^\delta - Fm^\delta). \quad (2.7)$$

### 2.2.3 Morozov Discrepancy Principle

The Morozov Discrepancy Principle is a guide in selecting the regularization parameter  $\alpha$ . The logic behind the principle is that knowing the magnitude of the error in the far field is bounded by  $\delta$ , we require  $q^{\alpha,\delta}$  to be such that the error produced is at most  $\delta$ . That is,

$$\|f^\delta - F'_m q^{\alpha,\delta} - Fm\| \leq \delta. \quad (2.8)$$

From our earlier assumption, we know that

$$\|f^\delta - Fm\| \leq \delta.$$

It follows that we can achieve the bound in (2.8) by solving [50]

$$\|f^\delta - F'_m q^{\alpha,\delta} - Fm\| = \rho \|f^\delta - Fm\|$$

for some  $0 < \rho < 1$ . Squaring both sides and bringing all terms to one side leads to  $\varphi(\alpha) = 0$  where

$$\varphi(\alpha) = \|f^\delta - F'_m q^{\alpha,\delta} - Fm\|^2 - \rho^2 \|f^\delta - Fm\|^2, \quad (2.9)$$

which we solve using Newton's method. Note this solution will be unique provided  $\|f^\delta - f\| \leq \delta \leq \|f\|$  (see [58, page 48]).

To compute  $\varphi'(\alpha)$  for given  $\alpha$ , we differentiate both sides of (2.6) with respect to  $\alpha$  to get

$$q^{\alpha,\delta} + \alpha J_\alpha + (F'_m)^T F'_m J_\alpha = \mathbf{0},$$

where  $J_\alpha$  denotes the Jacobian of  $q^{\alpha,\delta}$  i.e.  $J_\alpha = \frac{dq^{\alpha,\delta}}{d\alpha}$ . Therefore,

$$J_\alpha = - [\alpha I + (F'_m)^T F'_m]^{-1} q^{\alpha,\delta}. \quad (2.10)$$

Now note  $q^{\alpha,\delta}$  is the only term in  $\varphi(\alpha)$  that depends on  $\alpha$ . Therefore, differentiating the expression in (2.9) using the chain rule, we get

$$\varphi'(\alpha) = -2 (f^\delta - F'_m q^{\alpha,\delta} - Fm) \cdot (F'_m J_\alpha),$$

where  $J_\alpha$  is given by (2.10). Then given an estimate  $\alpha_t$ , we compute an improved estimate  $\alpha_{t+1}$  by using Newton's formula

$$\alpha_{t+1} = \alpha_t - \frac{\varphi(\alpha_t)}{\varphi'(\alpha_t)}. \quad (2.11)$$

From before, equation  $\varphi(\alpha) = 0$  will have a unique solution  $\alpha^*$  provided  $\|f^\delta - f\| \leq \delta \leq \|f\|$ . The following result [5, Theorem 5.4.1] describes the convergence of Newton's method (2.11) in solving  $\varphi(\alpha) = 0$ .

**Theorem 2.2.2.** *Suppose*

$$|\varphi'(\alpha) - \varphi'(\beta)| \leq K |\alpha - \beta|$$

*for all  $\alpha, \beta$  in some neighbourhood of  $\alpha^*$ , and  $K > 0$  is a constant. Then there exists an  $\epsilon > 0$  such that  $|\alpha_0 - \alpha^*| \leq \epsilon$  implies sequence  $\{\alpha_t\}$  converges to  $\alpha^*$ , where  $\alpha_0$  is the initial guess in Newton's method. We also have*

$$|\alpha_t - \alpha^*| \leq \frac{(M\epsilon)^{2^t}}{M}$$

*for some constant  $M$  satisfying  $M\epsilon < 1$ .*

With regards to equation (2.2), the iterated solution from the Levenburg-Marquardt



scheme will converge to the true solution provided (2.2) has a unique solution and

$$\|\mathcal{F}(\chi) - \mathcal{F}(\psi) - \mathcal{F}'_\chi(\chi - \psi)\| \leq c\|\chi - \psi\|\|\mathcal{F}(\chi) - \mathcal{F}(\psi)\|$$

for some  $c > 0$ , and all  $\chi, \psi$  in some neighbourhood of  $m$ . Thus the existence and uniqueness of the iterated solution depends on the existence and uniqueness of the solution to (2.2).

## 2.3 Angular Legendre Functions

Let  $L_s$  denote the Legendre polynomial of degree  $s$

$$L_s(r) = \frac{1}{2^s s!} \frac{d^s}{dr^s} [(r^2 - 1)^s],$$

satisfying the recurrence relation [1]

$$(s+1)L_{s+1}(r) = (2s+1)rL_s(r) - sL_{s-1}(r).$$

Now using the fact [1] that the Legendre polynomials are orthogonal on  $[-1, 1]$ :

$$\frac{2s_1+1}{2} \int_{-1}^1 L_{s_1}(r) \overline{L_{s_2}(r)} dr = \delta_{s_1, s_2}, \quad s_1, s_2 \in \mathbb{N},$$

and the complex exponential functions are orthogonal on  $[0, 2\pi]$ :

$$\frac{1}{2\pi} \int_0^{2\pi} e^{it_1\theta} \overline{e^{it_2\theta}} d\theta = \delta_{t_1, t_2}, \quad t_1, t_2 \in \mathbb{Z},$$

we deduce

$$\frac{2s_1+1}{4\pi} \int_0^{2\pi} \int_{-1}^1 L_{s_1}(r) e^{it_1\theta} \overline{L_{s_2}(r) e^{it_2\theta}} dr d\theta = \delta_{s_1, s_2} \delta_{t_1, t_2}.$$

Therefore, the functions

$$A_{s,t}(r, \theta) = L_s(r)e^{it\theta}, \quad s \in \mathbb{N}, \quad t \in \mathbb{Z}, \quad (2.12)$$

are orthogonal on  $R = [-1, 1] \times [0, 2\pi]$ . We refer to the functions given in (2.12) as the *Angular Legendre functions*.

## 2.4 Notational and Variable Definitions

In this thesis, the surface integral of a function  $f$  along a closed piecewise-smooth curve  $C \subset \mathbb{R}^2$  is defined as

$$\int_C f(\mathbf{x}) ds(\mathbf{x}) = \int_a^b f(\mathbf{q}(t)) \sqrt{[q_1'(t)]^2 + [q_2'(t)]^2} dt,$$

where  $\mathbf{q} : [a, b] \rightarrow C; t \mapsto (q_1(t), q_2(t))$  is a bijective parametrization of the curve  $C$ .

We then define the  $L^2$  inner product on  $C$  as follows:

$$\langle \phi, \psi \rangle_{L^2(C)} = \int_C \phi(\mathbf{x}) \overline{\psi(\mathbf{x})} ds(\mathbf{x}).$$

The following table gives a summary of the basic notational and variable definitions used throughout the thesis, for the reader's convenience.

$B$	Open unit disk $\{(x, y) \in \mathbb{R}^2 : x^2 + y^2 < 1\}$
$\partial B$	Unit circle $\{(x, y) \in \mathbb{R}^2 : x^2 + y^2 = 1\}$
$D$	An impenetrable scatter with piecewise smooth boundary
$\partial D$	The boundary of $D$
$\Omega$	The open region $B \setminus \bar{D}$
$\Omega^c$	The region $\mathbb{R}^2 \setminus B$
$\partial\Omega$	Unit circle $\{(x, y) \in \mathbb{R}^2 : x^2 + y^2 = 1\}$
$k$	Wavenumber
$\omega$	Radial frequency
$\hat{\mathbf{d}}$	Wave direction
$u$	Total field
$u^i$	Induced field
$u^{\text{inc}}$	Incident field
$u^s$	Scattered field
$u_{\text{int}}$	Interior solution in $\Omega$
$u_{\text{ext}}$	Interior solution in $\Omega^c$
$\Phi$	Green's function for the 2D Helmholtz equation
$H_m^{(1)}$	Hankel's function of the first kind; degree $m$
$J_m$	Bessel's function of the first kind; degree $m$
$\mathbf{x}, \mathbf{y}$	Domain points
$\mathbf{s}$	Boundary point
$G_i$	Interior solution operator
$G_e$	Exterior solution operator
$G_p$	Particular solution operator for the interior problem
$\gamma$	Trace operator
$\mathbf{q}$	Invertible map which parametrizes $\partial\Omega$
FEM	Finite element method
BEM	Boundary element method
$h$	Mesh size in the FEM
$\mathbf{n}$	Unit outward normal
$n$	Refractive index function defined on $\mathbb{R}^2 \setminus \bar{D}$ , which has compact support $\Omega$
$m$	This function is defined as $m = 1 - n$
$\mathcal{B}$	Boundary condition operator
$R$	Robin boundary condition operator; $Rv = \frac{\partial v}{\partial n} + ikv$
$R_j^{(N)}$	Special quadrature formulation
$u_\infty$	Far field
$\hat{\mathbf{x}}$	Defined to be $\frac{\mathbf{x}}{ \mathbf{x} }$
$\mathcal{F}_c$	Operator which maps $m$ to the resulting far field in the case where $D = \emptyset$
$\mathcal{F}_c$	Operator which maps $m$ to the resulting far field in the case where $D \neq \emptyset$
$\alpha$	Regularisation parameter
$P_{l,j}$	Logan-Shepp polynomial
$A_{s,t}$	Angular-Legendre function

## Chapter 3

# Coupled FEM-BEM Technique

Consider an impenetrable scatterer  $D \subset \mathbb{R}^2$  with piecewise-smooth boundary  $\partial D$ , surrounded by a heterogeneous dielectric medium. We assume the refractive index  $n(\mathbf{x})$  is constant outside the open unit disk  $B$  centred at the origin, so that the heterogeneity of the medium is contained within the open set  $\Omega := B \setminus \bar{D}$  (see Figure 3.1). Note however that we have adopted the unusual notation of taking  $\partial\Omega$  to only be the outer boundary of  $\Omega$  i.e.  $\partial\Omega = \partial B$ . We normalize so that

$$n(\mathbf{x}) = 1 \quad \text{for} \quad \mathbf{x} \in \mathbb{R}^2 \setminus B,$$

and assume  $n(\mathbf{x})$  is bounded and piecewise-continuous in  $\Omega$ .

Consider an *incident* plane wave  $u^{\text{inc}}(\mathbf{x}) = e^{ik\mathbf{x} \cdot \hat{\mathbf{d}}}$ , where  $k$  is the wavenumber and the unit vector  $\hat{\mathbf{d}}$  denotes the wave-direction. When illuminated by  $u^{\text{inc}}$ , the boundary  $\partial D$  together with the heterogeneous media within  $\Omega$  induce a *scattered field*  $u^s$  in  $\mathbb{R}^2 \setminus B$ , and an *induced field*  $u^i$  in  $\Omega$ . The *total field*  $u$  is then

$$u(\mathbf{x}) = \begin{cases} u^i(\mathbf{x}), & \mathbf{x} \in \Omega, \\ u^{\text{inc}}(\mathbf{x}) + u^s(\mathbf{x}), & \mathbf{x} \in \mathbb{R}^2 \setminus B. \end{cases} \quad (3.1)$$

where  $u^i$  contains a scattered and incident component.

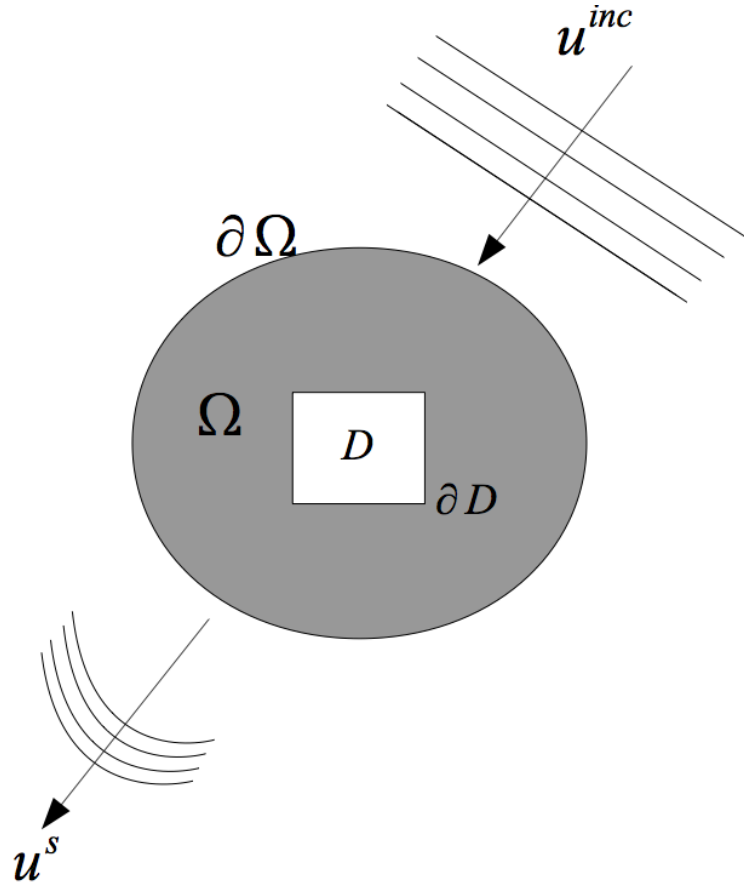


Figure 3.1: A impenetrable scatterer  $D$  with piecewise-smooth outer boundary  $\partial D$ , surrounded by a dielectric coating  $\Omega$ . Note that the closed region  $\bar{D}$  together with  $\Omega$  make up the open unit disk  $B$ , so that the boundary  $\partial B$  of  $B$  is the unit circle  $\{(x, y) \in \mathbb{R}^2 : x^2 + y^2 = 1\}$ . Moreover,  $\partial B = \partial \Omega$ .

In this chapter we describe a numerical method to solve the *forward media problem* of computing the total field  $u$ , given knowledge of the boundary  $\partial D$  and the refractive index  $n$ . In Chapter 6, we will solve the corresponding inverse problem.

**Definition 3.0.1** (Forward Media Problem). *Find the total field  $u \in C^2(\mathbb{R}^2 \setminus \bar{D}) \cap C(\mathbb{R}^2 \setminus D)$  that satisfies the Helmholtz equation*

$$\Delta u(\mathbf{x}) + k^2 n(\mathbf{x}) u(\mathbf{x}) = 0 \text{ for } \mathbf{x} \in \mathbb{R}^2 \setminus \bar{D}, \quad (3.2)$$

*the Sommerfeld radiation condition*

$$\lim_{r \rightarrow \infty} \sqrt{r} \left( \frac{\partial u^s}{\partial r} - i k u^s \right) = 0, \quad r = |\mathbf{x}| \quad (3.3)$$

uniformly with respect to the direction  $\mathbf{x}$ , and a boundary condition of the form

$$\mathcal{B}u(\mathbf{x}) = f(\mathbf{x}) \text{ on } \partial D, \quad (3.4)$$

where the operator  $\mathcal{B}$  and the function  $f$  depend on the incident wave and the material properties of the scatterer  $D$ .

The theory presented in this chapter is applicable to the cases where the boundary condition is either a Dirichlet, Neumann or Robin boundary condition.

## 3.1 Motivation

Two common approaches for solving PDEs are finite element methods (FEMs) and boundary element methods (BEMs).

FEMs can solve PDEs over complex geometries, and are suitable for both homogeneous and heterogeneous problems. FEMs are only applicable to problems over bounded regions and consequently cannot be applied when solving the forward media problem (3.2)–(3.4), which has an unbounded domain. An adaptation of the FEM is the *expanding grid* technique [42, 65], in which the unbounded domain  $\mathbb{R}^2 \setminus \bar{D}$  is approximated by a large bounded domain, and the Sommerfeld radiation condition (3.3) is replaced by an appropriate boundary condition on the outer boundary. This approach requires solving a large linear system, because the accuracy of the FEM depends on using a fixed number of elements per wavelength in the FEM mesh [31, 72, 73]. Moreover, this technique does not provide a direct approximation to the far field pattern of the scattered wave [60], which is useful in several applications.

BEMs reformulate PDEs in terms of boundary integral equations, making discretization only necessary over the boundary. This reformulation reduces the dimension of the problem by one, which means solving a smaller linear system compared to

the FEM, making BEMs an efficient technique for solving homogeneous PDEs over unbounded regions. In the case of scattering problems, BEMs are particularly desirable because they ensure the radiation condition (3.3) is satisfied exactly. However, BEMs are not applicable to heterogeneous problems and therefore cannot be solely used to solve the forward media problem (3.2)–(3.4). Moreover, standard BEMs require the boundary to be smooth; their application to problems with non-smooth boundaries requires adaptation [66, 44, 54, 83].

In this chapter, we solve the forward media problem using the coupled FEM-BEM technique, which takes advantage of and facilitates the strengths of both approaches, while avoiding the disadvantages associated with each technique. We introduce a smooth artificial transmission boundary  $\partial\Omega$  which splits  $\mathbb{R}^2 \setminus \bar{D}$  into two sub-regions:

1. **Interior Region:** The region  $\Omega$ , which contains the heterogeneity of the medium, where  $n(\mathbf{x})$  is some bounded piecewise-continuous function.
2. **Exterior Region:** The region  $\Omega^c := \mathbb{R}^2 \setminus B$  exterior to the artificial boundary, where  $n(\mathbf{x}) = 1$ .

We then apply a transmission boundary condition on  $\partial\Omega$  through which the original forward problem can be split into two sub-problems: an exterior problem in  $\Omega^c$  and an interior problem in  $\Omega$ . We then apply a BEM in  $\Omega^c$  and a FEM in  $\Omega$ . In this way, the radiation condition (3.3) is satisfied exactly, while the heterogeneous refractive index  $n(\mathbf{x})$  in  $\Omega$  and the non-smooth boundary  $\partial D$  are handled appropriately.

## 3.2 Coupled FEM-BEM Technique

In the coupled FEM-BEM technique we seek a solution of the form

$$u(\mathbf{x}) = \begin{cases} u_{int}(\mathbf{x}), & \mathbf{x} \in \Omega, \\ u_{ext}(\mathbf{x}), & \mathbf{x} \in \Omega^c, \end{cases} \quad (3.5)$$

for  $u_{int} \in H^1(\Omega)$  and  $u_{ext} \in \mathcal{W}(\Omega^c)$ , where

$$\mathcal{W}(\Omega^c) = \left\{ v \in H_{loc}^1(\Omega^c) : \frac{\partial v}{\partial r} - ikv = o\left(\frac{1}{\sqrt{r}}\right) \right\}.$$

Standard regularity results (see [41, Chapter 8]) imply that a solution of the form (3.5) is the unique solution to the forward media problem, provided  $u$  and its normal derivative are continuous across  $\partial\Omega$ .

The aim behind seeking a solution of the form (3.5) is to split the forward media problem into an interior boundary value problem in  $\Omega$  and an exterior boundary value problem in  $\Omega^c$ , which can readily be solved using a FEM and BEM respectively. To formulate these two boundary value problems, we require a suitable boundary condition on  $\partial\Omega$ . This boundary condition should ensure continuity of  $u$  and its normal derivative across  $\partial\Omega$ .

To derive such a boundary condition, we follow [60, 61] and suppose

$$[R(u^s)](\mathbf{x}) = \frac{\partial u^s}{\partial \mathbf{n}}(\mathbf{x}) + ik u^s(\mathbf{x}), \quad \mathbf{x} \in \partial\Omega,$$

is known, where  $\mathbf{n}$  represents the unit outward pointing normal vector on  $\partial\Omega$ . That is,  $R(u^s) = \mu$  for some known  $\mu$ . Then we enforce a Robin boundary condition on  $\partial\Omega$  to formulate the aforementioned interior and exterior BVPs. To do this we introduce operators  $G_i$  and  $G_e$  below (see [60]), noting that since  $u_{int} \in H^1(\Omega)$ , Sobolev's trace theorem [5] implies  $\mu \in H^{-\frac{1}{2}}(\partial\Omega)$ .

**Definition 3.2.1.** *The operator  $G_i : H^{-\frac{1}{2}}(\partial\Omega) \rightarrow H^1(\Omega)$  is defined by the following BVP. Given  $\lambda \in H^{-\frac{1}{2}}(\partial\Omega)$ ,  $G_i\lambda$  is defined to be the weak solution  $v \in H^1(\Omega)$  of:*

$$\Delta v(\mathbf{x}) + k^2 n(\mathbf{x})v(\mathbf{x}) = 0, \quad \mathbf{x} \in \Omega, \tag{3.6}$$

$$\mathcal{B}v(\mathbf{x}) = f(\mathbf{x}), \quad \mathbf{x} \in \partial D, \tag{3.7}$$

$$[R(v)](\mathbf{x}) = \lambda(\mathbf{x}), \quad \mathbf{x} \in \partial\Omega. \tag{3.8}$$



**Remark.** We will numerically compute  $G_i\lambda$  using the finite element method (see Section 3.3.2 for more details). Existence and uniqueness results for such an approach are well known (see [6, 85]).

**Definition 3.2.2.** The operator  $G_e : H^{-\frac{1}{2}}(\partial\Omega) \rightarrow \mathcal{W}(\Omega^c)$  is defined by the following BVP. Given  $\lambda \in H^{-\frac{1}{2}}(\partial\Omega)$ ,  $G_e\lambda$  is defined as the weak solution  $v \in \mathcal{W}(\Omega^c)$  of:

$$\Delta v(\mathbf{x}) + k^2 v(\mathbf{x}) = 0, \quad \mathbf{x} \in \Omega^c, \quad (3.9)$$

$$\lim_{r \rightarrow \infty} r \left( \frac{\partial v}{\partial r} - i k v \right) = 0, \quad (3.10)$$

$$[R(v)](\mathbf{x}) = \lambda(\mathbf{x}), \quad \mathbf{x} \in \partial\Omega. \quad (3.11)$$

In (3.9), we have used  $n(\mathbf{x}) = 1$  in  $\mathbb{R}^2 \setminus B$ . Equipped with the operators  $G_e$  and  $G_i$ , we now state the following result proved in [60].

**Proposition 3.2.3.** The solution to the forward problem (3.2)–(3.4) is given by

$$u = \begin{cases} G_i [\mu + R(u^{\text{inc}})], & \text{in } \Omega, \\ G_e \mu + u^{\text{inc}}, & \text{in } \Omega^c, \end{cases} \quad (3.12)$$

provided

$$\gamma(G_e - G_i)\mu = \gamma G_i [R(u^{\text{inc}})] - \gamma u^{\text{inc}} \quad \text{on } \partial\Omega, \quad (3.13)$$

where

$$\gamma : H^1(\mathbb{R}^2 \setminus (\bar{D} \cup \partial\Omega)) \rightarrow H^{\frac{1}{2}}(\partial\Omega), \quad \gamma v = v|_{\partial\Omega}$$

is the trace operator.

*Proof.* By definition of  $G_i$ , the function  $u$  defined in (3.12) automatically satisfies boundary condition (3.4), and also satisfies Helmholtz equation (3.2) when  $\mathbf{x} \in \Omega$ . By definition of  $G_e$ , the solution also satisfies radiation condition (3.3). When

$\mathbf{x} \in \Omega^c$ ,

$$\begin{aligned}
\Delta u(\mathbf{x}) + k^2 n(\mathbf{x}) u(\mathbf{x}) &= \Delta u(\mathbf{x}) + k^2 u(\mathbf{x}) \quad \text{since } n(\mathbf{x}) = 1 \text{ for } \mathbf{x} \in \Omega^c \\
&= [\Delta G_e \mu](\mathbf{x}) + k^2 [G_e \mu](\mathbf{x}) + \Delta u^{\text{inc}}(\mathbf{x}) + k^2 u^{\text{inc}}(\mathbf{x}) \\
&= [\Delta G_e \mu](\mathbf{x}) + k^2 [G_e \mu](\mathbf{x}) \\
&= 0 \quad \text{by definition of } G_e.
\end{aligned}$$

Thus all that remains to show is that  $u$  and  $\frac{\partial u}{\partial \mathbf{n}}$  are continuous across  $\partial\Omega$ . Note from the definition of  $G_i$  that

$$\begin{aligned}
R(u) &= R(G_i [\mu + R(u^{\text{inc}})]) \\
&= \mu + R(u^{\text{inc}}).
\end{aligned}$$

From the definition of  $G_e$  we have

$$R(G_e \mu) = \mu.$$

In that case, it follows

$$\begin{aligned}
R(u) &= R(G_e \mu + u^{\text{inc}}) \\
&= R(G_e \mu) + R(u^{\text{inc}}) \\
&= \mu + R(u^{\text{inc}}),
\end{aligned}$$

which implies  $R(u)$  is continuous across  $\partial\Omega$ . Noting that (3.13) ensures continuity of  $u$  across  $\partial\Omega$ , we deduce  $\frac{\partial u}{\partial \mathbf{n}}$  must also be continuous across  $\partial\Omega$  by definition of  $R$ .  $\square$

We will solve the forward problem by computing the unknown  $\mu$ , and then evaluating the solution using (3.12). We do this by solving (3.13) using a Galerkin scheme.

### 3.3 Galerkin Scheme

We assume the smooth boundary  $\partial\Omega$  can be parametrized via an invertible map

$$\mathbf{q} : [0, 2\pi) \rightarrow \partial\Omega; \theta \mapsto (q_1(\theta), q_2(\theta)), \quad (3.14)$$

where  $q_1(\theta)$  and  $q_2(\theta)$  are  $2\pi$ -periodic continuously differentiable functions. This is advantageous because then  $\mu \circ \mathbf{q}$  is a function on  $[0, 2\pi)$ , and as a result can be approximated with high-order accuracy using the finite-dimensional space spanned by  $\{e^{ij\theta} : j = -N, \dots, N-1\}$ . Hence, we seek an approximate solution to (3.13) of the form

$$\mu(\mathbf{q}(\theta)) = \sum_{j=-N}^{N-1} a_j e^{ij\theta}, \quad \theta \in [0, 2\pi),$$

where the spectral coefficients  $a_j$  need to be determined for  $j = -N, \dots, N-1$ . We define  $L = \gamma(G_e - G_i)$  and  $g = \gamma G_i [R(u^{\text{inc}})] - u^{\text{inc}}$ , to rewrite (3.13) as  $L\mu = g$ . The Galerkin scheme requires

$$\langle L\mu, z_m \rangle_{L^2(\partial\Omega)} = \langle g, z_m \rangle_{L^2(\partial\Omega)}$$

for  $m = -N, \dots, N-1$ , where  $z_m(\mathbf{x}) = e^{im\mathbf{q}^{-1}(\mathbf{x})}$  and

$$\langle \varphi, \psi \rangle_{L^2(\partial\Omega)} = \int_{\partial\Omega} \varphi(\mathbf{x}) \overline{\psi(\mathbf{x})} ds(\mathbf{x}).$$

Therefore, we require

$$\sum_{j=-N}^{N-1} a_j \langle Lz_j, z_m \rangle_{L^2(\partial\Omega)} = \langle g, z_m \rangle_{L^2(\partial\Omega)} \quad (3.15)$$

for  $m = -N, \dots, N-1$ . We approximate the inner products in (3.15) using the rectangle rule quadrature approximation which converges exponentially on  $\partial\Omega$  (see [67, 68]) as  $N$  increases; the error is of order  $\mathcal{O}(e^{-N\sigma})$  where  $\sigma$  denotes half the width of the

parallel strip in the complex plane into which the integrand can be analytically extended. Applying this quadrature rule, we get

$$\langle \varphi, \psi \rangle_{L^2(\partial\Omega)} \approx \sum_{s=0}^{2N-1} \frac{\pi}{N} \varphi(\mathbf{q}(\theta_s)) \overline{\psi(\mathbf{q}(\theta_s))} J(\theta_s) \quad (3.16)$$

with

$$\theta_s = \frac{\pi s}{N} \quad \text{for } s = 0, \dots, 2N-1 \quad (3.17)$$

and Jacobian  $J(\theta_s) = \sqrt{[q'_1(\theta_s)]^2 + [q'_2(\theta_s)]^2}$ . We thus get

$$\langle Lz_j, z_m \rangle_{L^2(\partial\Omega)} \approx \sum_{s=0}^{2N-1} \frac{\pi}{N} \overline{z_m(\mathbf{q}(\theta_s))} J(\theta_s) [Lz_j](\mathbf{q}(\theta_s)).$$

Therefore the discrete version of (3.15) becomes

$$\sum_{j=-N}^{N-1} a_j \left\{ \sum_{s=0}^{2N-1} \frac{\pi}{N} \overline{z_m(\mathbf{q}(\theta_s))} J(\theta_s) [Lz_j](\mathbf{q}(\theta_s)) \right\} = \sum_{s=0}^{2N-1} \frac{\pi}{N} \overline{z_m(\mathbf{q}(\theta_s))} J(\theta_s) g(\mathbf{q}(\theta_s))$$

for  $m = -N, \dots, N-1$ . We write this system as a matrix equation

$$A\mathbf{x} = \mathbf{b}, \quad (3.18)$$

where

$$\begin{aligned} A_{j,m} &= \sum_{s=0}^{2N-1} \frac{\pi}{N} \overline{z_{j-N}(\mathbf{q}(\theta_s))} J(\theta_s) [Lz_{m-N}](\mathbf{q}(\theta_s)), \\ b_j &= \sum_{s=0}^{2N-1} \frac{\pi}{N} \overline{z_{j-N}(\mathbf{q}(\theta_s))} J(\theta_s) g(\mathbf{q}(\theta_s)), \quad j = 0, 1, \dots, 2N-1, \end{aligned}$$

and  $\mathbf{x} = (a_{1-N}, a_{2-N}, \dots, a_{N-1}, a_N)^T$  is a column vector containing the unknown coefficients.

Noting that  $L = \gamma(G_e - G_i)$ , we see that the main task in assembling matrix  $A$  in

(3.18) is evaluating  $[G_e z_m](\mathbf{q}(\theta_s))$  and  $[G_i z_m](\mathbf{q}(\theta_s))$  for  $m = -N, \dots, N-1$ . Likewise assembling  $\mathbf{b}$  requires evaluating  $[G_i R(u^{\text{inc}})](\mathbf{q}(\theta_s))$  because  $g = \gamma G_i [R(u^{\text{inc}})] - \gamma u^{\text{inc}}$ . All other calculations involved are relatively straightforward. We remark it improves efficiency to store the values of  $G_e z_m$  and  $G_i z_m$  for each  $z_m$  involved in assembling (3.18); the advantage of doing this is explained in Section 3.3.3. We now explain how to evaluate  $[G_e \lambda](\mathbf{q}(\theta_s))$  and  $[G_i \lambda](\mathbf{q}(\theta_s))$  for arbitrary  $\lambda$ .

### 3.3.1 Evaluating the exterior field

Evaluating the exterior field  $G_e \lambda$  equates to finding the radiating solution  $v$  to the Helmholtz equation in  $\Omega^c$ , satisfying the Robin condition  $R(v) = \lambda$  on  $\partial\Omega$ . We solve this problem using the Nyström method outlined in [23], which converges with order  $\mathcal{O}(1/n^q)$  for boundaries of class  $C^{q+2}$  (see [66]). We begin by using a direct formulation [61, Page 529] for  $v$  of the form

$$v(\mathbf{x}) = \int_{\partial\Omega} \left\{ \frac{\partial\Phi(\mathbf{x}, \mathbf{y})}{\partial\mathbf{n}(\mathbf{y})} v(\mathbf{y}) - \Phi(\mathbf{x}, \mathbf{y}) \frac{\partial v(\mathbf{y})}{\partial\mathbf{n}(\mathbf{y})} \right\} ds(\mathbf{y}), \quad (3.19)$$

for  $\mathbf{x} \in \Omega^c$ , where

$$\Phi(\mathbf{x}, \mathbf{y}) = \frac{i}{4} H_0^{(1)}(k|\mathbf{x} - \mathbf{y}|) \quad (3.20)$$

is the Green's function for the 2D Helmholtz equation and  $H_0^{(1)}$  is Hankel's function of the first kind. Using the boundary condition (3.11),

$$\frac{\partial v(\mathbf{y})}{\partial\mathbf{n}(\mathbf{y})} = \lambda(\mathbf{y}) - ikv(\mathbf{y}) \quad \text{for } \mathbf{y} \in \partial\Omega,$$

equation (3.19) becomes:

$$v(\mathbf{x}) = \int_{\partial\Omega} \left\{ \frac{\partial\Phi(\mathbf{x}, \mathbf{y})}{\partial\mathbf{n}(\mathbf{y})} v(\mathbf{y}) + ik\Phi(\mathbf{x}, \mathbf{y})v(\mathbf{y}) - \Phi(\mathbf{x}, \mathbf{y})\lambda(\mathbf{y}) \right\} ds(\mathbf{y}), \quad \mathbf{x} \in \Omega^c. \quad (3.21)$$

Applying the jump relations in [23, Page 39] which describe the limiting behaviour of surface potentials as the boundary is approached, we take the limiting value of both sides as  $\mathbf{x} \rightarrow \partial\Omega$  to obtain

$$v(\mathbf{x}) = \frac{1}{2}v(\mathbf{x}) + \int_{\partial\Omega} \left\{ \frac{\partial\Phi(\mathbf{x}, \mathbf{y})}{\partial\mathbf{n}(\mathbf{y})} v(\mathbf{y}) + ik\Phi(\mathbf{x}, \mathbf{y})v(\mathbf{y}) - \Phi(\mathbf{x}, \mathbf{y})\lambda(\mathbf{y}) \right\} ds(\mathbf{y}), \quad \mathbf{x} \in \partial\Omega.$$

Thus

$$-\frac{1}{2}v(\mathbf{x}) + \int_{\partial\Omega} \left\{ \frac{\partial\Phi(\mathbf{x}, \mathbf{y})}{\partial\mathbf{n}(\mathbf{y})} + ik\Phi(\mathbf{x}, \mathbf{y}) \right\} v(\mathbf{y}) ds(\mathbf{y}) = \int_{\partial\Omega} \Phi(\mathbf{x}, \mathbf{y})\lambda(\mathbf{y}) ds(\mathbf{y}).$$

Applying the parametrization (3.14) of  $\partial\Omega$ , we get

$$\begin{aligned} -\frac{1}{2}v(\mathbf{q}(\theta)) + \int_0^{2\pi} \{L(\theta, s) + ikM(\theta, s)\}v(\mathbf{q}(s)) ds \\ = \int_0^{2\pi} M(\theta, s)\lambda(\mathbf{q}(s)) ds \quad \text{for } \theta \in [0, 2\pi], \end{aligned} \quad (3.22)$$

where

$$\begin{aligned} L(\theta, s) &= \frac{\partial\Phi(\mathbf{q}(\theta), \mathbf{q}(s))}{\partial\mathbf{n}(\mathbf{q}(s))} J(s), \\ M(\theta, s) &= \Phi(\mathbf{q}(\theta), \mathbf{q}(s))J(s). \end{aligned}$$

The kernels  $L(\theta, s)$  and  $M(\theta, s)$  have a logarithmic singularity at  $\theta = s$ . This means the integrals appearing in (3.22) are singular, and hence cannot be evaluated accurately using standard quadrature rules. Thus we apply the following result [23, p.68]:

**Theorem 3.3.1.** *The kernels  $L(\theta, s)$  and  $M(\theta, s)$  can be split as:*

$$\begin{aligned} L(\theta, s) &= L_1(\theta, s) \ln \left( 4 \sin^2 \frac{\theta - s}{2} \right) + L_2(\theta, s), \\ M(\theta, s) &= M_1(\theta, s) \ln \left( 4 \sin^2 \frac{\theta - s}{2} \right) + M_2(\theta, s), \end{aligned}$$

where

$$\begin{aligned}
L_1(\theta, s) &= \frac{k}{2\pi} \{q_2'(s)[q_1(\theta) - q_1(s)] - q_1'(\theta)[q_2(\theta) - q_2(s)]\} \frac{J_1(kr(\theta, s))}{r(\theta, s)}, \\
L_2(\theta, s) &= L(\theta, s) - L_1(\theta, s) \ln \left( 4 \sin^2 \frac{\theta - s}{2} \right), \\
M_1(\theta, s) &= -\frac{1}{2\pi} J(s) J_0(kr(\theta, s)), \\
M_2(\theta, s) &= M(\theta, s) - M_1(\theta, s) \ln \left( 4 \sin^2 \frac{\theta - s}{2} \right), \\
r(t, s) &= \{[q_1(\theta) - q_1(s)]^2 + [q_2(\theta) - q_2(s)]^2\}^{\frac{1}{2}},
\end{aligned}$$

and  $J_0, J_1$  represent Bessel functions of the first kind of order zero and one respectively. Furthermore the kernels  $L_1(\theta, s)$  and  $M_1(\theta, s)$  can be continuously extended for  $s = \theta$ . Limiting values of kernels  $L_2(\theta, s)$  and  $M_2(\theta, s)$  at the point  $\theta = s$  are given by the expressions:

$$\begin{aligned}
L_2(\theta, \theta) &= \frac{q_1'(\theta)q_2''(\theta) - q_2'(\theta)q_1''(\theta)}{2\pi J(\theta)}, \\
M_2(\theta, \theta) &= \left\{ \frac{i}{2} - \frac{C}{\pi} - \frac{1}{\pi} \ln \left( \frac{kJ(\theta)}{2} \right) \right\} J(\theta)
\end{aligned}$$

for  $0 \leq \theta \leq 2\pi$ , where  $C$  denotes Euler's constant.

**Remark.** Note the expressions for  $L_2$  and  $M_2$  are exact expressions i.e. they are not approximations.

By defining

$$\begin{aligned}
K_1(\theta, s) &= L_1(\theta, s) + ikM_1(\theta, s), \\
K_2(\theta, s) &= L_2(\theta, s) + ikM_2(\theta, s),
\end{aligned}$$

equation (3.22) becomes

$$-\frac{1}{2}\tilde{v}(\theta) + \int_0^{2\pi} K(\theta, s)\tilde{v}(s) ds = \int_0^{2\pi} M(\theta, s)\tilde{\lambda}(s) ds \quad \text{for } \theta \in [0, 2\pi], \quad (3.23)$$

where  $\tilde{v} = v \circ \mathbf{q}$ ,  $\tilde{\lambda} = \lambda \circ \mathbf{q}$  and

$$K(\theta, s) = K_1(\theta, s) \ln \left( 4 \sin^2 \frac{\theta - s}{2} \right) + K_2(\theta, s).$$

In the Nyström method we approximate the above integrals by using appropriate quadrature formulas. The first formula (see [23, p.78]) is given by the following lemma, which like before converges exponentially [67, 68] with the error term being of order  $\mathcal{O}(e^{-N\sigma})$ .

**Lemma 3.3.2.** *Given the quadrature points (3.17), define*

$$R_j^{(N)}(\theta) = -\frac{2\pi}{N} \sum_{m=1}^{N-1} \frac{1}{m} \cos m(\theta - \theta_j) - \frac{\pi}{N^2} \cos N(\theta - \theta_j), \quad \text{for } j = 0, \dots, 2N-1.$$

*Then for an analytic function  $h$ , we have the approximation*

$$\int_0^{2\pi} h(s) \ln \left( 4 \sin^2 \frac{\theta - s}{2} \right) ds \approx \sum_{j=0}^{2N-1} R_j^{(N)}(\theta) h(\theta_j), \quad 0 \leq \theta \leq 2\pi.$$

This result can be directly used to approximate the singular integrals

$$\begin{aligned} & \int_0^{2\pi} K_1(\theta, s) \ln \left( 4 \sin^2 \frac{\theta - s}{2} \right) \tilde{v}(s) ds, \\ & \int_0^{2\pi} M_1(\theta, s) \ln \left( 4 \sin^2 \frac{\theta - s}{2} \right) \tilde{\lambda}(s) ds, \end{aligned}$$

respectively. For the smooth integrals, we apply the rectangle rule quadrature formula. That is,

$$\begin{aligned} \int_0^{2\pi} K_2(\theta, s) \tilde{v}(s) ds & \approx \sum_{j=0}^{2N-1} \frac{\pi}{N} K_2(\theta, \theta_j) \tilde{v}(\theta_j), \\ \int_0^{2\pi} M_2(\theta, s) \tilde{v}(s) ds & \approx \sum_{j=0}^{2N-1} \frac{\pi}{N} M_2(\theta, \theta_j) \tilde{v}(\theta_j). \end{aligned}$$



Using the above approximations, (3.23) becomes

$$\begin{aligned} -\frac{1}{2}\tilde{v}(\theta) + \sum_{j=0}^{2N-1} \left\{ R_j^{(N)}(\theta) K_1(\theta, \theta_j) + \frac{\pi}{N} K_2(\theta, \theta_j) \right\} \tilde{v}(\theta_j) \\ = \sum_{j=0}^{2N-1} \left\{ R_j^{(N)}(\theta) M_1(\theta, \theta_j) + \frac{\pi}{N} M_2(\theta, \theta_j) \right\} \tilde{\lambda}(\theta_j). \end{aligned}$$

Requiring equality to hold for  $t$  at the quadrature points (3.17), we get

$$\begin{aligned} -\frac{1}{2}V_i + \frac{1}{2} \sum_{j=0}^{2N-1} \left[ R_j^{(N)}(\theta_i) K_1(\theta_i, \theta_j) + \frac{\pi}{n} K_2(\theta_i, \theta_j) \right] V_j \\ = \sum_{j=0}^{2N-1} \left[ R_j^{(N)}(\theta_i) M_1(\theta_i, \theta_j) + \frac{\pi}{n} M_2(\theta_i, \theta_j) \right] \Lambda_j \end{aligned}$$

for  $i = 0, \dots, 2N - 1$ , where  $V_j = v(\mathbf{q}(\theta_j))$  and  $\Lambda_j = \mu(\mathbf{q}(\theta_j))$ .

This discretized series of equations represents a linear system

$$(I - \mathbf{K})\mathbf{v} = \mathbf{\Lambda}, \quad (3.24)$$

where  $I$  is the identity matrix,  $\mathbf{v}_i = V_i$ ,

$$\mathbf{\Lambda}_i = -2 \sum_{j=0}^{2N-1} \left[ R_j^{(N)}(\theta_i) M_1(\theta_i, \theta_j) + \frac{\pi}{N} M_2(\theta_i, \theta_j) \right] \Lambda_j,$$

and

$$\mathbf{K}_{i,j} = R_j^{(N)}(\theta_i) K_1(\theta_i, \theta_j) + \frac{\pi}{N} K_2(\theta_i, \theta_j).$$

Due to the high order convergence of the Nyström method,  $N$  will be small in numerical computations. This enables us to use Gaussian elimination to solve matrix equation (3.24) for  $\mathbf{v}$ , which is precisely a column vector such that

$$\mathbf{v}_s = [G_e \lambda](\mathbf{q}(\theta_s)).$$

### 3.3.2 Evaluating the interior field

We evaluate the interior field  $[G_i\lambda](\mathbf{q}(\theta_s))$  using the FEM technique [55]. We start by multiplying (3.6) by a test function  $w \in H^1(\Omega)$  to obtain

$$w(\mathbf{x}) (\Delta v(\mathbf{x}) + k^2 n(\mathbf{x}) v(\mathbf{x})) = 0, \quad \mathbf{x} \in \Omega,$$

and then integrate over  $\Omega$  to get

$$\iint_{\Omega} w(\mathbf{x}) (\Delta v(\mathbf{x}) + k^2 n(\mathbf{x}) v(\mathbf{x})) \, d\mathbf{x} = 0.$$

Splitting the above integral and applying Green's first identity [5, p.325] yields

$$\iint_{\Omega} \nabla v(\mathbf{x}) \cdot \nabla w(\mathbf{x}) \, d\mathbf{x} - k^2 \iint_{\Omega} n(\mathbf{x}) w(\mathbf{x}) v(\mathbf{x}) \, d\mathbf{x} = \int_{\partial\Omega \cup \partial D} w(\mathbf{x}) \frac{\partial v}{\partial \mathbf{n}}(\mathbf{x}) \, dS,$$

where  $\mathbf{n}$  is the outward-pointing unit normal. Now recall that  $v = G_i\lambda$  satisfies the Robin boundary condition

$$\frac{\partial v}{\partial \mathbf{n}} + ikv = \lambda$$

on  $\partial\Omega$ . Thus

$$\begin{aligned} \int_{\partial\Omega \cup \partial D} w(\mathbf{x}) \frac{\partial v}{\partial \mathbf{n}}(\mathbf{x}) \, ds &= \int_{\partial D} w(\mathbf{x}) \frac{\partial v}{\partial \mathbf{n}}(\mathbf{x}) \, ds + \int_{\partial\Omega} w(\mathbf{x}) \frac{\partial v}{\partial \mathbf{n}}(\mathbf{x}) \, ds \\ &= \int_{\partial D} w(\mathbf{x}) \frac{\partial v}{\partial \mathbf{n}}(\mathbf{x}) \, ds + \int_{\partial\Omega} w(\mathbf{x}) (\lambda(\mathbf{x}) - ikv(\mathbf{x})) \, ds. \end{aligned}$$

It follows that the weak form of (3.6)–(3.8) is to solve

$$\begin{aligned} &\iint_{\Omega} \nabla v(\mathbf{x}) \cdot \nabla w(\mathbf{x}) \, d\mathbf{x} - k^2 \iint_{\Omega} n(\mathbf{x}) v(\mathbf{x}) w(\mathbf{x}) \, d\mathbf{x} \\ &+ ik \int_{\partial\Omega} v(\mathbf{x}) w(\mathbf{x}) \, ds = \int_{\partial D} w(\mathbf{x}) \frac{\partial v}{\partial \mathbf{n}} \, ds + \int_{\partial\Omega} w(\mathbf{x}) \lambda(\mathbf{x}) \, ds \end{aligned} \quad (3.25)$$

for all  $w \in H^1(\Omega)$ . In the finite element method, we seek an approximate solution  $v_h$  to (3.25) in a finite-dimensional subspace  $W_h \subset H^1(\Omega)$ . To construct  $W_h$ , let  $\partial\Omega_h$  and  $\partial D_h$  be polygonal approximations to  $\partial\Omega$  and  $\partial D$  respectively, where  $\partial\Omega_h$  includes vertices

$$\{\mathbf{q}(\theta_s) \mid s = 0, \dots, 2N - 1\}.$$

Let  $\Omega_h$  denote the polygonal domain bounded by  $\partial\Omega_h$  and  $\partial D_h$ , and let  $\tau_h$  be the regular triangulation of  $\overline{\Omega}_h$  with triangles of diameter<sup>1</sup>  $h$ , where the vertices of  $\tau_h$  are given by

$$\mathbf{x}_1, \mathbf{x}_1, \mathbf{x}_2, \dots, \mathbf{x}_{l-1}, \mathbf{x}_l.$$

For each  $i = 1, 2, \dots, l$  we define a piecewise linear function  $\phi_i$  to equal 1 at the vertex  $\mathbf{x}_i$  and to vanish at every other vertex, and then take

$$W_h = \text{span}\{\phi_1, \phi_2, \dots, \phi_l\}.$$

Thus we require (3.25) to hold for all  $w \in \text{span}\{\phi_1, \phi_2, \dots, \phi_l\}$ . That is, we require

$$\begin{aligned} & \iint_{\Omega_h} \nabla v(\mathbf{x}) \cdot \nabla \phi_j(\mathbf{x}) \, d\mathbf{x} - k^2 \iint_{\Omega_h} n(\mathbf{x}) v(\mathbf{x}) \phi_j(\mathbf{x}) \, d\mathbf{x} \\ & + ik \int_{\partial\Omega_h} v(\mathbf{x}) \phi_j(\mathbf{x}) \, ds = \int_{\partial D_h} \phi_j(\mathbf{x}) \frac{\partial v}{\partial \mathbf{n}} \, ds + \int_{\partial\Omega_h} \phi_j(\mathbf{x}) \lambda(\mathbf{x}) \, ds \end{aligned} \quad (3.26)$$

to hold for  $j = 1, 2, \dots, l$ . We then seek an approximate solution  $v_h$  to (3.26) of the form

$$v_h(\mathbf{x}) = \sum_{i=1}^l v_i \phi_i(\mathbf{x}), \quad (3.27)$$

---

<sup>1</sup>Here the diameter of a triangle is defined to be the length of its longest side [55]. In practice, the diameter  $h$  of the triangles in the triangulation  $\tau_h$  can be chosen to be either uniform, or to vary adaptively to account for the geometrical shape of the boundary  $\partial D$ . For example, the results we give in Section 3.4 use a uniform mesh when  $\partial D$  is a circle, but employ mesh refinement around the corners of  $\partial D$ , when  $D$  is a square.

where the coefficients  $v_i \approx v(\mathbf{x}_i)$  are unknown. Substituting (3.27) into (3.26), we get:

$$\begin{aligned} & \sum_{i=1}^l v_i \left( \iint_{\Omega_h} \nabla \phi_i(\mathbf{x}) \cdot \nabla \phi_j(\mathbf{x}) \, d\mathbf{x} - k^2 \iint_{\Omega_h} n(\mathbf{x}) \phi_i(\mathbf{x}) \phi_j(\mathbf{x}) \, d\mathbf{x} + ik \int_{\partial\Omega_h} \phi_i(\mathbf{x}) \phi_j(\mathbf{x}) \, ds \right) \\ &= \int_{\partial\Omega_h} \phi_j(\mathbf{x}) \lambda(\mathbf{x}) \, ds + \sum_{i=1}^l v_i \int_{\partial D_h} \phi_j(\mathbf{x}) \frac{\partial \phi_i}{\partial \mathbf{n}}(\mathbf{x}) \, ds. \end{aligned}$$

We write this algebraic equation in the form of a matrix equation

$$(B - k^2 C + ikD)\mathbf{v} = \mathbf{d}, \quad (3.28)$$

where

$$B_{j,i} = \iint_{\Omega_h} \nabla \phi_i(\mathbf{x}) \cdot \nabla \phi_j(\mathbf{x}) \, d\mathbf{x}, \quad (3.29)$$

$$C_{j,i} = \iint_{\Omega_h} n(\mathbf{x}) \phi_i(\mathbf{x}) \phi_j(\mathbf{x}) \, d\mathbf{x}, \quad (3.30)$$

$$D_{j,i} = \int_{\partial\Omega_h} \phi_j(\mathbf{x}) \phi_i(\mathbf{x}) \, ds, \quad (3.31)$$

$$\mathbf{d} = \int_{\partial\Omega_h} \phi_j(\mathbf{x}) \lambda(\mathbf{x}) \, ds + \sum_{i=1}^l v_i \int_{\partial D_h} \phi_j(\mathbf{x}) \frac{\partial \phi_i}{\partial \mathbf{n}}(\mathbf{x}) \, ds. \quad (3.32)$$

The column vector  $\mathbf{d}$  is mostly zero; the only entries that are non-zero are entries which correspond to a vertex  $\mathbf{x}_j$  such that  $\mathbf{x}_j \in \partial\Omega_h \cup \partial D_h$ . In that case, there are two possibilities:

1. If  $\mathbf{x}_j \in \partial D$ , then we modify the  $j$ -th row of  $B - k^2 C + ikD$  and the  $j$ -th entry of  $\mathbf{d}$  appropriately to account for the boundary condition (3.4) on  $\partial D$ .
2. If  $\mathbf{x}_j \in \partial\Omega_h$ , then

$$\mathbf{d}(j) = \int_{\partial\Omega_h} \phi_j(\mathbf{x}) \lambda(\mathbf{x}) \, ds. \quad (3.33)$$

To calculate this integral numerically, we approximate  $\lambda$  by

$$\lambda(\mathbf{x}) = \sum_{i=0}^l \lambda_i \phi_i(\mathbf{x}),$$

where  $\lambda_i = \lambda(\mathbf{x}_i)$ . Then

$$\mathbf{d}(j) = \sum_{i=0}^l \lambda_i \int_{\partial\Omega_h} \phi_j(\mathbf{x}) \phi_i(\mathbf{x}) \, ds. \quad (3.34)$$

This is known in closed form.

### 3.3.3 Constructing the Solution to the Forward Problem

We solve the Galerkin system (3.18) for the coefficients contained in  $\mathbf{x}$ , to obtain the value of

$$\mu(\mathbf{q}(\theta)) = \sum_{j=-N}^{N-1} a_j z_j(\mathbf{q}(\theta)), \quad \theta \in [0, 2\pi),$$

on the transmission boundary  $\partial\Omega$ . Recall from (3.12), that the solution to the forward problem is given by

$$u = \begin{cases} G_i [\mu + R(u^{\text{inc}})], & \text{in } \Omega, \\ G_e \mu + u^{\text{inc}}, & \text{in } \Omega^c. \end{cases} \quad (3.35)$$

That is, the solution in the interior is given by  $G_i [R(u^{\text{inc}})]$ , while the solution in the exterior is given by  $G_e \mu + u^{\text{inc}}$ . We can evaluate the expression  $u(\mathbf{x})$  for  $\mathbf{x} \in \Omega^c$  using the Nyström method from Section 3.3.1, and the expression for  $u$  in  $\Omega$  using the Finite Element method outlined in Section 3.3.2.

Note that the far field of  $u^s$  given by [23, page 75]

$$u_\infty(\hat{\mathbf{x}}) = \frac{e^{\frac{\pi i}{4}}}{\sqrt{8\pi k}} \int_{\partial\Omega} \left\{ \frac{\partial e^{-ik\hat{\mathbf{x}} \cdot \mathbf{y}}}{\partial \mathbf{n}(\mathbf{y})} u^s(\mathbf{y}) + ik e^{-ik\hat{\mathbf{x}} \cdot \mathbf{y}} u^s(\mathbf{y}) - e^{-ik\hat{\mathbf{x}} \cdot \mathbf{y}} \mu(\mathbf{y}) \right\} ds(\mathbf{y}), \quad (3.36)$$

where  $\hat{\mathbf{x}} = \frac{\mathbf{x}}{|\mathbf{x}|}$  (see Section 9.4 of the appendix for the derivation). We numerically evaluate this integral using a rectangle method approximation, in which we reuse the same quadrature points from the Nyström scheme. Thus by exploiting the calculations which were done while assembling the matrix equation (3.18), we can compute the far field without having to perform many additional computations. The same applies to the exterior field  $u^s$  itself, which we expressed as a boundary integral in Section 3.3.1.

To see how this can be done, note for instance that

$$\begin{aligned} G_e \mu(\mathbf{q}(\theta)) &= G_e \left( \sum_{j=-N}^{N-1} a_j z_j(\mathbf{q}(\theta)) \right) \\ &= \sum_{j=-N+1}^N a_j [G_e z_j](\mathbf{q}(\theta)). \end{aligned}$$

The values of  $G_e z_{m-N}(\mathbf{q}(\theta_s))$  at the points (3.17) for  $m = 0, \dots, 2N-1$ , while assembling (3.18) are given by  $G_e z_j(\mathbf{q}(\theta(s)))$  for  $j = -N, \dots, N-1$ . Hence  $G_e \mu$  is simply given by a linear combination of values already computed. The same is true for  $G_i \mu$ ; and hence evaluating  $G_i [R(u^{\text{inc}}) + \mu] = G_i [R(u^{\text{inc}})] + G_i \mu$  depends on computing  $G_i [R(u^{\text{inc}})]$ . However,  $G_i [R(u^{\text{inc}})]$  was already computed while assembling the vector  $\mathbf{b}$  in (3.18).

## 3.4 Numerical Results

In this section, we demonstrate the proficiency of the coupled FEM-BEM technique in solving the forward problem. We first show the efficiency of the Nyström method and the effectiveness of the FEM in solving BVPs associated with operators  $G_e$  and  $G_i$  respectively. We then validate our numerical implementation of the coupled FEM-BEM method, by considering instances of the forward scattering problem for which the true solution is known. The first test problem we consider is the case

where  $\partial D$  is a circle, in which case the true solution is known exactly. After that we consider the case where  $\partial D$  is a square which is a problem of great interest in its own right (see [66, 44, 54, 83] and references therein). In Section 3.4.4 we give excellent results for this particular forward problem using the coupled FEM-BEM technique.

### 3.4.1 Efficiency of the Nyström Method

In the special case where  $\Omega$  is a circle and  $\lambda = -R(u^{\text{inc}})$ , there exists a series representation (called the Mie-series solution) to the BVP which defines  $G_e\lambda$ . Taking the incident wave-direction to be  $\hat{\mathbf{d}} = (1, 0)$ , the Mie-series solution is given by

$$G_e\lambda(r, \theta) = - \sum_{m=-\infty}^{\infty} \frac{i^m J_{|m|}(ka)}{H_{|m|}^{(1)}(ka)} H_{|m|}^{(1)}(kr) (\cos m\theta + i \sin m\theta),$$

where  $a$  is the radius of  $D$ ,  $J_{|m|}$  and  $H_{|m|}^{(1)}$  represent Bessel's and Hankel's function of the first kind of degree  $|m|$  respectively.

In Table 3.1, we measure the maximum absolute difference between the far field corresponding to our approximate solution and the Mie-series solution, over 1000 equally spaced points around the unit circle. The results contained therein illustrate the exponential convergence achieved by the Nyström method.

$N$	Error	$N$	Error	$N$	Error
3	1.241e-1	7	1.320e-3	15	5.755e-5
4	9.881e-3	8	2.054e-4	16	1.111e-5
5	3.956e-4	9	2.476e-5	17	1.824e-6
6	1.005e-5	10	2.364e-6	18	2.582e-7
7	2.311e-7	11	1.833e-7	19	3.185e-8
8	7.152e-9	12	1.184e-8	20	3.453e-9
9	4.835e-10	13	7.624e-10	21	3.767e-10

Table 3.1: Error between the exact far field of  $G_e\lambda$  and the approximate far field obtained using the Nyström scheme when  $\lambda = -R(u^{\text{inc}})$ , for varying values of  $N$ . The three wavenumbers considered are  $k = \frac{\pi}{2}$  (left),  $k = \pi$  (center) and  $k = 2\pi$  (right).

### 3.4.2 Accuracy of the FEM

To demonstrate accuracy for the FEM, we make use of the following result.

**Proposition 3.4.1.** *Suppose  $\Omega$  is the annulus centered at the origin with outer radius 1. Then the function  $v(x, y) = \sin a(x + y)$  solves (3.6)–(3.8) in the special case where  $n(\mathbf{x}) = 1$ ,  $\lambda(\mathbf{x}) = a(x + y) \cos a(x + y) + ik \sin a(x + y)$  for  $\mathbf{x} \in \Omega$  and (3.7) is the Dirichlet boundary condition  $v(x, y) = \sin a(x + y)$  for  $(x, y) \in \partial D$ , provided  $k = \sqrt{2}a$ .*

Thus in the special case above, the exact value of  $G_i \lambda$  is known. In Table 3.2, we demonstrate the accuracy of the FEM by measuring the  $L_2$ -norm error between the true value of  $G_i \lambda$  given in Proposition 3.4.1, and the approximate value resulting from the FEM. We note that we generate the FEM mesh using the DistMesh package [81].

$h$	Error	$h$	Error	$h$	Error
0.1	4.3081e-3	0.1	1.8315e-2	0.1	7.3493e-2
0.05	9.4984e-4	0.05	3.8982e-3	0.05	1.6016e-2
0.025	2.3210e-4	0.025	9.6915e-4	0.025	4.0376e-3
0.0125	5.4802e-5	0.0125	2.2916e-4	0.0125	9.5619e-4
0.00625	1.3611e-5	0.00625	5.7215e-5	0.00625	2.3911e-4
0.003125	3.3684e-6	0.003125	1.4149e-5	0.003125	5.9057e-5

Table 3.2: Error between the exact value of  $G_i \lambda$  and our approximate solution at the FEM mesh points using the FEM for  $k = \frac{\pi}{2}$  (left),  $k = \pi$  (center) and  $k = 2\pi$  (right). In each table we have fixed the radius of  $D$  to be 0.6. The values for  $N$  are 9, 13 and 21 respectively.

### 3.4.3 Validation of the Coupled FEM-BEM Scheme

To validate our implementation of the coupled FEM-BEM technique, we now consider a test problem for which the Mie-series solution to the forward problem is known. We present tables for  $k = \frac{\pi}{2}, k = \pi, 2\pi$ . Using Table 3.1 as a guide, we fix a suitable value for  $N$  to highlight the effect of refining the mesh-size  $h$  in Table 3.3. We then fix a value for  $h$ , to analyze the effect of varying  $N$  in Table 3.4.



We take the wave-direction to be  $\hat{\mathbf{d}} = (1, 0)$ ,  $n(\mathbf{x}) = 1$  for  $\mathbf{x} \in \Omega$  and  $D$  to be the circle centered at the origin, with radius 0.6. We further assume that the boundary condition on  $\partial D$  is the Dirichlet condition  $u = 0$ . The error tables are produced by considering 1000 equally spaced points around the unit circle, and then measuring the maximum absolute difference between the far field corresponding to the coupled FEM-BEM solution and the Mie-series solution.

$h$	Error	$h$	Error	$h$	Error
0.1	2.4961e-3	0.1	1.1349e-2	0.1	4.9056e-2
0.05	4.3498e-4	0.05	2.2603e-3	0.05	1.0796e-2
0.025	1.1706e-4	0.025	6.5902e-4	0.025	2.5665e-3
0.0125	3.0294e-5	0.0125	1.3218e-4	0.0125	7.1020e-4
0.00625	6.9530e-6	0.00625	4.4789e-5	0.00625	1.7201e-4
0.003125	1.7447e-6	0.003125	8.0216e-6	0.003125	3.9412e-5

Table 3.3: Maximum error in the far field between the true and numerical solution for  $k = \frac{\pi}{2}$  (left),  $k = \pi$  (center) and  $k = 2\pi$  (right). We have fixed  $N = 9$  (left),  $N = 13$  (center) and  $N = 21$  (right). These values show that the order of convergence of the FEM is preserved in the FEM-BEM technique.

$N$	Error	$N$	Error	$N$	Error
3	2.0805e-2	7	2.2143e-5	15	3.7221e-5
4	6.1758e-4	8	8.4286e-6	16	3.6226e-5
5	1.0276e-5	9	8.2247e-6	17	3.6111e-5
6	1.6607e-6	10	8.0123e-6	18	3.8888e-5
7	1.7783e-6	11	1.0008e-5	19	3.6711e-5
8	1.6914e-6	12	1.0449e-5	20	3.7460e-5
9	1.7447e-6	13	8.0216e-6	21	3.9411e-5

Table 3.4: Maximum error in the far field between the true and numerical solution for  $k = \frac{\pi}{2}$  (left),  $k = \pi$  (center) and  $k = 2\pi$  (right). We have fixed  $h = 0.003125$  for all three tables. These values show that increasing  $N$  does not necessarily reduce the error between the true and numerical solution. This is because the Nyström scheme converges much more rapidly than the FEM. Consequently, the error resulting from the Nyström scheme becomes dominated by the error from the FEM, once  $N$  surpasses a certain threshold.

### 3.4.4 Scattering by a Square

In this section, we consider the forward problem in the case where  $D$  is a square of side length 1. We first verify in Table 3.5 that the FEM effectively solves the BVP

defined by  $G_i$  over  $\Omega$ , which now possesses a non-smooth boundary.

We then provide error tables for the coupled FEM-BEM technique as a whole. Unlike Section 3.4.3 however, the true solution to the forward problem is unknown. However, a very accurate numerical solution to this forward problem can be obtained using the MPSpack toolbox in Matlab [9], which we shall henceforth refer to as the “MPS-solution”.

In Table 3.6, we fix a suitable value for  $N$  to highlight the effect of refining the mesh-size  $h$ . In Table 3.7, we fix an appropriate value for  $h$ , to show the effect of varying  $N$ . In both cases, the results are qualitatively similar to those observed in the previous section.

$h$	Error	$h$	Error	$h$	Error
0.1	1.5549e-2	0.1	7.1651e-2	0.1	2.3100e-1
0.05	3.1623e-3	0.05	1.6530e-2	0.05	5.8019e-2
0.025	8.7988e-4	0.025	3.6472e-3	0.025	1.4842e-2
0.0125	2.1958e-4	0.0125	4.3282e-4	0.0125	3.4115e-3
0.00625	5.3455e-5	0.00625	2.3226e-4	0.00625	8.7846e-4
0.003125	1.3272e-6	0.003125	5.8020e-5	0.003125	2.3111e-4

Table 3.5: Error between the exact value of  $G_i\lambda$  and our approximate solution using the FEM for  $k = \frac{\pi}{2}$  (left),  $k = \pi$  (center) and  $k = 2\pi$  (right). In each table we have fixed the side-length of  $D$  to be 0.5. To account for the non-smoothness of the boundary  $\partial D$ , we have employed mesh-refinement at the corners the square; the distribution of the mesh size  $h$  is given according to the formula  $h(x, y) = \min\{h_1(x, y), h_2(x, y), h_3(x, y), h_4(x, y)\}$ , where  $h_1(x, y) = 0.5 + \|(x, y) - (0.5, 0.5)\|$ ,  $h_2(x, y) = 0.5 + \|(x, y) - (-0.5, 0.5)\|$ ,  $h_3(x, y) = 0.5 + \|(x, y) - (0.5, -0.5)\|$  and  $h_4(x, y) = 0.5 + \|(x, y) - (-0.5, -0.5)\|$ .

$h$	Error	$h$	Error	$h$	Error
0.1	1.6697e-2	0.1	3.4810e-2	0.1	1.0538e-1
0.05	6.1004e-3	0.05	1.2242e-2	0.05	3.0250e-2
0.025	2.2291e-3	0.025	4.5037e-3	0.025	9.4937e-3
0.0125	8.3334e-4	0.0125	1.7312e-3	0.0125	3.3268e-3
0.00625	3.0910e-5	0.00625	6.6305e-4	0.00625	1.2482e-3
0.003125	1.0518e-4	0.003125	2.5633e-4	0.003125	4.7774e-4

Table 3.6: Maximum error in the far field between the MPS-solution and FEM-BEM solution for  $k = \frac{\pi}{2}$  (left),  $k = \pi$  (center) and  $k = 2\pi$  (right). We have fixed  $N = 9$  (left),  $N = 13$  (center) and  $N = 21$  (right).

$N$	Error	$N$	Error	$N$	Error
3	2.5820e-2	7	1.3826e-3	15	4.7849e-4
4	1.0889e-2	8	6.7072e-4	16	4.8089e-4
5	1.8398e-3	9	2.6819e-4	17	4.7643e-4
6	1.3033e-3	10	1.9145e-4	18	4.7545e-4
7	2.9459e-4	11	2.7829e-4	19	4.7845e-4
8	3.3404e-4	12	2.7263e-4	20	4.7904e-4
9	1.0518e-4	13	2.5633e-4	21	4.7774e-4

Table 3.7: Maximum error in the far field between the MPS-solution and FEM-BEM solution for  $k = \frac{\pi}{2}$  (left),  $k = \pi$  (center) and  $k = 2\pi$  (right). We have fixed  $h = 0.003125$  for all three tables.

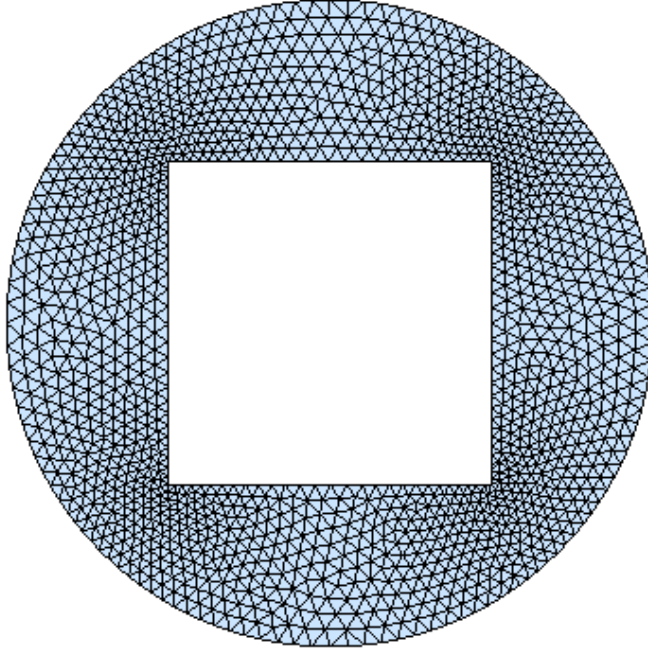


Figure 3.2: Visualization of the mesh-refinement given in Table 3.5. Here  $h = 0.025$ .

### 3.4.5 Discussion

It is clear from the results of the previous section that our implementation of the coupled FEM-BEM technique is highly effective in accurately solving the forward problem. We believe our coupled FEM-BEM scheme can be significantly improved by implementing a higher order FEM, much like [39]. This is because when we compare Table 3.1 and Table 3.2, we immediately notice that the Nyström method has much faster convergence than the FEM. Consequently, when we combine both methods in the coupled FEM-BEM technique, the error from the Nyström scheme eventually becomes dominated by the error from the FEM, as evidenced in Table 3.4 and Table 3.7. Therefore incorporating a higher order FEM would produce better results, which is verified in [39].

Knowing how to choose the parameters from the previous section depends on the level of accuracy required. As an example, suppose we wanted to achieve an error of approximately  $10^{-6}$  when  $k = \frac{\pi}{2}$ . Then noting that the results in Tables 3.3 and 3.6 are qualitatively similar to the results in Table 3.2, we choose  $h$  and  $N$  so that a balanced error of  $10^{-6}$  occurs in the FEM and Nyström method respectively.

Table 3.2 suggests to achieve an error of  $10^{-6}$ , we must take  $h = 0.003125$ . From Table 3.1,  $N = 7$  seems sufficient to achieve an error of  $10^{-6}$  in the Nyström scheme. The fact that this particular choice of parameters works is then verified in Table 3.4.

We mentioned in Section 3.1 that the accuracy of the FEM depends on using a fixed number of elements per wavelength in the FEM mesh. This explains the visible trends in Tables 3.2, 3.3 3.5 and 3.6 of the error becoming larger for fixed  $h$  as  $k$  increases.

# Chapter 4

## Coupled FEM-BEM Technique for Inhomogeneous Problems

### 4.1 The Inhomogeneous Problem

In the previous chapter, we applied a coupled FEM-BEM technique to the forward problem. In Chapters 5–6 we will describe a numerical method to solve the corresponding inverse problem, which will involve solving heterogeneous BVPs characterized by an inhomogeneous Helmholtz equation. In this chapter we explain how to numerically solve forward inhomogeneous BVPs, which take the following form:

**Definition 4.1.1** (Inhomogeneous Problem). *Suppose  $g \in C(\mathbb{R}^2 \setminus D)$  has compact support contained in  $\Omega$  and  $n(\mathbf{x}) = 1$  for  $\mathbf{x} \in \mathbb{R}^2 \setminus B$ . Find the solution  $u \in C^2(\mathbb{R}^2 \setminus \bar{D}) \cap C(\mathbb{R}^2 \setminus D)$  to*

$$\Delta u(\mathbf{x}) + k^2 n(\mathbf{x}) u(\mathbf{x}) = g(\mathbf{x}) \quad \text{for } \mathbf{x} \in \mathbb{R}^2 \setminus \bar{D}, \quad (4.1)$$

*satisfying the Sommerfeld radiation condition*

$$\lim_{r \rightarrow \infty} \sqrt{r} \left( \frac{\partial u}{\partial r} - iku \right) = 0, \quad r = |\mathbf{x}|,$$

*uniformly with respect to the direction  $\frac{\mathbf{x}}{|\mathbf{x}|}$ , and a boundary condition*

$$\mathcal{B}u(\mathbf{x}) = f(\mathbf{x}), \quad \mathbf{x} \in \partial D, \quad (4.2)$$

*where the operator  $\mathcal{B}$  and the function  $f$  depend on the material properties of the scatterer  $D$ .*

This inhomogeneous problem is a challenging generalization of the forward problem from the previous chapter; the primary difference being we now assume  $g \neq 0$ . As a result, all the challenges discussed in Section 3.1 associated with the forward problem still remain. In particular, the nature of the problem dictates that standard approaches commonly used for solving BVPs cannot be utilized.

The FEM, for example, cannot be applied because the problem is defined over an unbounded region. Moreover, adaptations of the FEM (such as the expanding grids technique) are not ideal, because they do not ensure the Sommerfeld radiation condition is satisfied exactly.

BEM techniques are not applicable either. This is because we do not assume the refractive index function  $n(\mathbf{x})$  in (4.1) to be constant, and BEMs are only applicable to homogeneous problems.

The main challenge, however, which was previously absent, is our new assumption that the right hand side of (4.1) is non-zero. This prohibits us from applying the coupled FEM-BEM technique from the previous chapter. Instead we develop a novel extension of the coupled FEM-BEM technique, in which the function  $g(x)$  appearing in (4.1) is suitably accounted for. We formulate this new coupled FEM-BEM technique in the following section.

## 4.2 Formulation

We begin by seeking a solution of the form

$$u(\mathbf{x}) = \begin{cases} u_{int}(\mathbf{x}), & \mathbf{x} \in \Omega, \\ u_{ext}(\mathbf{x}), & \mathbf{x} \in \Omega^c, \end{cases}$$

for  $u_{int} \in H^1(\Omega)$  and  $u_{ext} \in \mathcal{W}(\Omega^c)$ , such that  $u$  and  $\frac{\partial u}{\partial \mathbf{n}}$  are continuous across  $\partial\Omega$ .

As in Chapter 3 we suppose the quantity  $\mu = R(u)$  is known, where

$$[R(u)](\mathbf{x}) = \frac{\partial u}{\partial \mathbf{n}}(\mathbf{x}) + iku(\mathbf{x}), \quad \mathbf{x} \in \partial\Omega,$$

and  $\mathbf{n}$  represents the outward pointing unit normal on  $\partial\Omega$ . Then returning to the notation from Chapter 3, it is clear that

$$u_{ext} = G_e \mu.$$

Now the interior field  $u_{int}$  must satisfy the inhomogeneous Helmholtz equation (4.1), the boundary condition (4.2) on  $\partial D$ , and the boundary condition  $R(u_{int}) = \mu$  on  $\partial\Omega$ . Recall from Chapter 3 that  $G_i \mu$  satisfies both these boundary conditions, as well as the Helmholtz equation

$$\Delta u(\mathbf{x}) + k^2 n(\mathbf{x})u(\mathbf{x}) = 0, \quad \mathbf{x} \in \Omega. \quad (4.3)$$

Hence we can write

$$u_{int} = G_i \mu + G_p g,$$

where  $G_p g$  is given by the following definition.

**Definition 4.2.1.** *Given a function  $g$  having compact support  $\Omega$ ,  $G_p g$  is defined to*

be the weak solution  $v$  to the BVP

$$\Delta v(\mathbf{x}) + k^2 n(\mathbf{x})v(\mathbf{x}) = g(\mathbf{x}), \quad \mathbf{x} \in \Omega, \quad (4.4)$$

$$v(\mathbf{x}) = 0, \quad \mathbf{x} \in \partial D, \quad (4.5)$$

$$[R(v)](\mathbf{x}) = 0, \quad \mathbf{x} \in \partial\Omega. \quad (4.6)$$

Equipped with this definition, we establish the following result.

**Proposition 4.2.2.** *The solution to the inhomogeneous problem given in Definition 4.1.1 is*

$$u = \begin{cases} G_i \mu + G_p g, & \mathbf{x} \in \Omega, \\ G_e \mu, & \mathbf{x} \in \mathbb{R}^2 \setminus B, \end{cases} \quad (4.7)$$

provided

$$\gamma G_i \mu + \gamma G_p g = \gamma G_e \mu \quad \text{on } \partial\Omega. \quad (4.8)$$

*Proof.* The function  $u$  defined in (4.7) satisfies (4.1)–(4.2) by definition of the operators  $G_e$ ,  $G_i$  and  $G_p$ . Thus all that remains to show is that  $u$  and  $\frac{\partial u}{\partial \mathbf{n}}$  are continuous across  $\partial\Omega$ . Note from the definitions of  $G_i$  and  $G_p$  that

$$\begin{aligned} R(u) &= R(G_i \mu + G_p g) \\ &= R(G_i \mu) + R(G_p g) \\ &= \mu + 0 \\ &= \mu. \end{aligned}$$

From the definition of  $G_e$  we have

$$R(G_e \mu) = \mu.$$



In that case it follows

$$\begin{aligned} R(u) &= R(G_e \mu) \\ &= \mu, \end{aligned}$$

which implies  $R(u)$  is continuous across  $\partial\Omega$ . Noting that (4.8) ensures continuity of  $u$  across  $\partial\Omega$ , we deduce  $\frac{\partial u}{\partial \mathbf{n}}$  must also be continuous across  $\partial\Omega$ .  $\square$

Notice (4.8) can be rewritten as

$$\gamma(G_e - G_i)\mu = \gamma G_p g \quad \text{on } \partial\Omega, \quad (4.9)$$

which is similar to the operator equation (3.13) we had in Chapter 3. The primary difference is that we need to compute  $G_p g$ , which we now explain.

### 4.3 Evaluating the induced field

To compute the induced field  $v = G_p g$  for a given function  $g$  defined on  $\Omega$ , we use the FEM. We begin by multiplying (4.4) through by a test function  $w \in H^1(\Omega)$  and integrate over  $\Omega$ , which yields

$$\iint_{\Omega} w(\mathbf{x}) \Delta v(\mathbf{x}) \, d\mathbf{x} + k^2 \iint_{\Omega} n(\mathbf{x}) w(\mathbf{x}) v(\mathbf{x}) \, d\mathbf{x} = \iint_{\Omega} w(\mathbf{x}) g(\mathbf{x}) \, d\mathbf{x}.$$

Applying Green's first identity [5, p.325] to the first integral on the left then gives

$$\begin{aligned} \iint_{\Omega} \nabla v(\mathbf{x}) \cdot \nabla w(\mathbf{x}) \, d\mathbf{x} - k^2 \iint_{\Omega} n(\mathbf{x}) w(\mathbf{x}) v(\mathbf{x}) \, d\mathbf{x} \\ = \int_{\partial\Omega \cup \partial D} w(\mathbf{x}) \frac{\partial v}{\partial \mathbf{n}}(\mathbf{x}) \, dS - \iint_{\Omega} w(\mathbf{x}) g(\mathbf{x}) \, d\mathbf{x}. \end{aligned}$$

Now recall that  $v$  satisfies the Robin boundary condition  $[R(v)](\mathbf{x}) = 0$  for  $\mathbf{x} \in \partial\Omega$ , and hence

$$\frac{\partial v}{\partial \mathbf{n}}(\mathbf{x}) = -ikv(\mathbf{x})$$

for  $\mathbf{x} \in \partial\Omega$ . Thus

$$\begin{aligned} \int_{\partial\Omega \cup \partial D} w(\mathbf{x}) \frac{\partial v}{\partial \mathbf{n}}(\mathbf{x}) \, ds &= \int_{\partial D} w(\mathbf{x}) \frac{\partial v}{\partial \mathbf{n}}(\mathbf{x}) \, ds + \int_{\partial\Omega} w(\mathbf{x}) \frac{\partial v}{\partial \mathbf{n}}(\mathbf{x}) \, ds \\ &= \int_{\partial D} w(\mathbf{x}) \frac{\partial v}{\partial \mathbf{n}}(\mathbf{x}) \, ds - ik \int_{\partial\Omega} w(\mathbf{x}) v(\mathbf{x}) \, ds. \end{aligned}$$

It follows that the weak form of (4.4)–(4.6) is to solve

$$\begin{aligned} \iint_{\Omega} \nabla v(\mathbf{x}) \cdot \nabla w(\mathbf{x}) \, d\mathbf{x} - k^2 \iint_{\Omega} n(\mathbf{x}) v(\mathbf{x}) w(\mathbf{x}) \, d\mathbf{x} + ik \int_{\partial\Omega} v(\mathbf{x}) w(\mathbf{x}) \, ds \\ = \int_{\partial D} w(\mathbf{x}) \frac{\partial v}{\partial \mathbf{n}}(\mathbf{x}) \, ds - \iint_{\Omega} w(\mathbf{x}) g(\mathbf{x}) \, d\mathbf{x} \end{aligned} \quad (4.10)$$

for  $w \in H^1(\Omega)$ . We then seek an approximate solution  $v_h$  to (4.10) by projecting  $v$  onto the finite-dimensional subspace  $W_h \subset H^1(\Omega)$ , defined in Section 3.3.2. We thus require

$$\begin{aligned} \iint_{\Omega_h} \nabla v(\mathbf{x}) \cdot \nabla \phi_j(\mathbf{x}) \, d\mathbf{x} - k^2 \iint_{\Omega_h} n(\mathbf{x}) v(\mathbf{x}) \phi_j(\mathbf{x}) \, d\mathbf{x} + ik \int_{\partial\Omega_h} v(\mathbf{x}) \phi_j(\mathbf{x}) \, ds \\ = \int_{\partial D_h} \phi_j(\mathbf{x}) \frac{\partial v}{\partial \mathbf{n}} \, ds - \iint_{\Omega_h} \phi_j(\mathbf{x}) g(\mathbf{x}) \, d\mathbf{x} \end{aligned} \quad (4.11)$$

to hold for  $j = 0, 1, \dots, l$ . We then seek an approximate solution  $v_h$  to (3.26) of the form

$$v_h(\mathbf{x}) = \sum_{i=0}^l v_i \phi_i(\mathbf{x}), \quad (4.12)$$

where the coefficients  $v_i \approx v(\mathbf{x}_i)$  are unknown. Substituting (4.12) into (4.11), we get:

$$\begin{aligned} & \sum_{i=0}^l v_i \left( \iint_{\Omega_h} \nabla \phi_i(\mathbf{x}) \cdot \nabla \phi_j(\mathbf{x}) \, d\mathbf{x} - k^2 \iint_{\Omega_h} n(\mathbf{x}) \phi_i(\mathbf{x}) \phi_j(\mathbf{x}) \, d\mathbf{x} + ik \int_{\partial\Omega_h} \phi_i(\mathbf{x}) \phi_j(\mathbf{x}) \, ds \right) \\ &= \int_{\partial D_h} \phi_j(\mathbf{x}) \frac{\partial v}{\partial \mathbf{n}}(\mathbf{x}) \, ds - \iint_{\Omega_h} \phi_j(\mathbf{x}) g(\mathbf{x}) \, d\mathbf{x}. \end{aligned}$$

We write this integral equation in the form of a matrix equation

$$(B - k^2 C + ikD)\mathbf{v} = \mathbf{g}, \quad (4.13)$$

where  $B$ ,  $C$  and  $D$  are given by (3.29)–(3.31), and

$$\mathbf{g}_j = \iint_{\Omega_h} \phi_j(\mathbf{x}) g(\mathbf{x}) \, d\mathbf{x}, \quad j = 0, 1, \dots, l.$$

Equation (4.13) is then solved using Gaussian elimination for the unknown vector  $\mathbf{v}$  containing the basis coefficients  $(v_i)_{0 \leq i \leq l}$  of  $v$ . Before doing so however, we must account for the Dirichlet boundary condition on  $\partial D$ . We do this by identifying which nodes lie on  $\partial D$ ; the rows of  $B - k^2 C + ikD$  corresponding to such nodes are replaced with corresponding rows of the identity matrix, while replacing the corresponding entries of  $\mathbf{g}$  with 0.

## 4.4 Numerical Results

First we demonstrate the accuracy of the FEM in computing  $G_p g$ , by considering a special instance of the BVP (4.4)–(4.6) for which the true solution is known. We then give error tables which show the accuracy of the coupled FEM-BEM scheme as a whole in solving the inhomogeneous problem. While doing so, we will show the effect of refining the mesh-size and increasing the number of Nyström points, as in Section 3.4.3.

### Accuracy of the FEM in computing $G_p g$

First we derive a special instance of the BVP (4.4)–(4.6) for which the true solution is known.

**Proposition 4.4.1.** *Let  $D$  be the circle centered at the origin with radius  $R < 1$  and let*

$$g(\mathbf{x}) = k^2(n(\mathbf{x}) - 1)v_1(\mathbf{x}) + k^2n(\mathbf{x})v_2(\mathbf{x}), \quad (4.14)$$

where

$$v_1(\mathbf{x}) = \sum_{p=0}^{\infty} [a_p J_p(kr) + H_p^{(1)}(kr)] e^{ip\theta}, \quad (4.15)$$

$$v_2(\mathbf{x}) = \sum_{p=1}^{\infty} [c_p r^p + r^{-p}] e^{ip\theta}, \quad (4.16)$$

and  $n$  is an arbitrary function in  $\Omega$ . Then

$$v(r, \theta) = v_1(r, \theta) + v_2(r, \theta)$$

is the solution to (4.4)–(4.6) when

$$a_p = \frac{(p - ik) \left[ 1 + H_p^{(1)}(k) \right] - k H_{p-1}^{(1)}(k) + (p + ik) \left[ R^{-p} H_{p-1}^{(1)}(Rk) + R^{-2p} \right]}{(ik - p) J_p(k) + k J_{p-1}(k) - (p + ik) R^{-p} J_p(Rk)},$$

$$c_p = -R^{-p} H_{p-1}^{(1)}(Rk) - R^{-2p} - a_p R^{-p} J_p(Rk),$$

where  $J_p$  represents Bessel's function of the first kind of degree  $p$ ,  $H_p^{(1)}$  represents Hankel's function of the first kind of degree  $p$ , and  $(r, \theta)$  denote the polar coordinates of  $\mathbf{x}$ .

*Proof.* Let

$$v_1(\mathbf{x}) = \sum_{p=0}^{\infty} [a_p J_p(kr) + b_p H_p^{(1)}(kr)] e^{ip\theta}, \quad (4.17)$$

where  $a_l$  and  $b_l$  are arbitrary constants. Then noting that  $v_1(\mathbf{x})$  satisfies the Helmholtz equation

$$\Delta v_1(\mathbf{x}) + k^2 v_1(\mathbf{x}) = 0$$

for  $\mathbf{x} \in \Omega$ , we deduce  $v_1$  also solves

$$\Delta v_1 + k^2 n(\mathbf{x}) v_1(\mathbf{x}) = k^2 (n(\mathbf{x}) - 1) v_1(\mathbf{x}),$$

for any function  $n$ . Now let

$$v_2(\mathbf{x}) = c_0 + d_0 \log r + \sum_{p=1}^{\infty} [c_p r^p + d_p r^{-p}] e^{ip\theta}, \quad \mathbf{x} \in \Omega,$$

so that  $\Delta v = 0$ , where  $c_p$  and  $d_p$  denote arbitrary constants. Then

$$\Delta v_1 + k^2 n(\mathbf{x}) v_1(\mathbf{x}) + \Delta v_2(\mathbf{x}) = k^2 (n(\mathbf{x}) - 1) v_1(\mathbf{x}).$$

That is,

$$\Delta v_1 + k^2 n(\mathbf{x}) v_1(\mathbf{x}) + \Delta v_2(\mathbf{x}) + k^2 n(\mathbf{x}) v_2(\mathbf{x}) = k^2 (n(\mathbf{x}) - 1) v_1(\mathbf{x}) + k^2 n(\mathbf{x}) v_2(\mathbf{x}).$$

Hence, the equation

$$\begin{aligned} \Delta v + k^2 n(\mathbf{x}) v(\mathbf{x}) &= k^2 (c_0 + d_0 \log r) n(\mathbf{x}) \\ &+ k^2 \sum_{p=0}^{\infty} [a_p (n(\mathbf{x}) - 1) J_p(kr) + b_p (n(\mathbf{x}) - 1) H_p^{(1)}(kr) + c_p n(\mathbf{x}) r^p + d_p n(\mathbf{x}) r^{-p}] e^{ip\theta} \end{aligned}$$

has solution

$$v(\mathbf{x}) = v_1(\mathbf{x}) + v_2(\mathbf{x})$$

$$= a_0 J_0(kr) + b_0 H_0^{(1)}(kr) + c_0 + d_0 \log r + \sum_{p=1}^{\infty} [a_p J_p(kr) + b_p H_p^{(1)}(kr) + c_p r^p + d_p r^{-p}] e^{ip\theta}.$$

Now we require  $[R(v)](\mathbf{x}) = 0$  on  $\partial\Omega$  and  $v(\mathbf{x}) = 0$  on  $\partial D$ . Noting that

$$\frac{\partial v}{\partial r} = ka_0 J'_0(kr) + kb_0 \{H_0^{(1)}\}'(kr) + \frac{d_0}{r} + \sum_{p=1}^{\infty} [ka_p J'_p(kr) + kb_p \{H_p^{(1)}\}'(kr) + pc_p r^{p-1} - pd_p r^{-p-1}] e^{ip\theta},$$

and using

$$J'_p(kr) = J_{p-1}(kr) - \frac{p}{kr} J_p(kr),$$

$$\{H_p^{(1)}\}'(kr) = H_{p-1}^{(1)}(kr) - \frac{p}{kr} H_p^{(1)}(kr),$$

we get

$$R(u) = a_0 [kJ_{-1}(kr) + ikJ_0(kr)] + b_0 [kH_{-1}^{(1)}(kr) + ikH_0^{(1)}(kr)] + c_0 + d_0 \left( \frac{1}{r} + \log r \right)$$

$$+ \sum_{p=0}^{\infty} \left\{ a_p \left[ kJ_{p-1}(kr) - \frac{p}{r} J_p(kr) + ikJ_p(kr) \right] + b_p \left[ kH_{p-1}^{(1)}(kr) - \frac{p}{r} H_p^{(1)}(kr) + ikH_p^{(1)}(kr) \right] \right.$$

$$\left. + c_p [pr^{p-1} + ikr^p] + d_p [-pr^{-p-1} + ikr^{-p}] \right\} e^{ip\theta}.$$

Thus the two boundary conditions will be satisfied provided

$$a_p [kJ_{p-1}(k) - pJ_p(k) + ikJ_p(k)] + b_p [kH_{p-1}^{(1)}(k) - pH_p^{(1)}(k) + ikH_p^{(1)}(k)]$$

$$+ c_p [p + ik] + d_p [-p + ik] = 0 \quad (4.18)$$

and

$$a_p J_p(Rpk) + b_p H_{p-1}^{(1)}(Rk) + c_p R^p + d_p R^{-p} = 0, \quad (4.19)$$

while taking  $a_0 = b_0 = c_0 = d_0 = 0$ . Now let  $b_p = d_p = 1$ . Then rearranging (4.19) gives

$$c_p = -R^{-p}H_{p-1}^{(1)}(Rk) - R^{-2p} - a_p R^{-p}J_p(Rk).$$

Substituting this back into (4.18) and simplifying, we get

$$a_p = \frac{(p - ik) \left[ 1 + H_p^{(1)}(k) \right] - kH_{p-1}^{(1)}(k) + (p + ik) \left[ R^{-p}H_{p-1}^{(1)}(Rk) + R^{-2p} \right]}{(ik - p)J_p(k) + kJ_{p-1}(k) - (p + ik)R^{-p}J_p(Rk)}.$$

□

To demonstrate the accuracy of the FEM in solving inhomogeneous BVPs of the form (4.4)–(4.6), we use the FEM to compute  $G_p g$  in the special case where  $D$  is the circle centered at the origin with radius 0.6, and  $g$  is given by (4.14). Then we give the  $L_2$ -error in Table 4.1 between this approximate solution and the true solution derived in Proposition 4.4.1. We compute the  $L_2$  error using a Gauss-rectangle rule taking the quadrature points to be the FEM mesh points.

$h$	Error	$h$	Error	$h$	Error
0.1	5.2222e-3	0.1	3.4811e-2	0.1	8.8205e-2
0.05	1.4589e-3	0.05	9.2527e-3	0.05	2.3561e-2
0.025	3.8205e-4	0.025	2.4901e-3	0.025	6.1429e-3
0.0125	9.7206e-5	0.0125	7.0136e-4	0.0125	1.6910e-4
0.00625	2.5899e-5	0.00625	1.8948e-4	0.00625	4.3873e-4
0.003125	7.0668e-6	0.003125	4.5109e-5	0.003125	1.1055e-4

Table 4.1:  $L_2$  error between the exact value of  $G_p g$  and our approximate solution at the FEM mesh points using the FEM for  $k = \frac{\pi}{2}$  (left),  $k = \pi$  (center) and  $k = 2\pi$  (right), where  $g$  is given by (4.14). In each table we have fixed the radius of  $D$  to be 0.6.

Next we show the accuracy of the coupled FEM-BEM technique in solving Inhomogeneous problems of the form given in Definition 4.1.1. To do so, we make use of the following result (taken from [35]) in order to design a suitable test problem.

**Lemma 4.4.2.** *The radiating wave functions*

$$e_m(r, \theta) = H_{|m|}^{(1)}(kr)e^{im\theta}, \quad m = 0, 1, 2, \dots, \infty,$$

*satisfy the homogeneous Helmholtz equation*

$$\Delta u(\mathbf{x}) + k^2 u(\mathbf{x}) = 0, \quad \mathbf{x} \in \mathbb{R}^2 \setminus \bar{D},$$

*and the Sommerfeld radiation condition. The far field of  $e_m$  is given by [35]*

$$e_m^\infty(\theta) = \sqrt{\frac{1}{\pi k}} (-1)^m (1 - i) e^{im\theta}.$$

For a proof of this lemma, we refer the reader to Section 9.5 of the Appendix. It follows that if we define

$$u(r, \theta) = H_1^{(1)}(kr)e^{i\theta},$$

then

$$\Delta u(\mathbf{x}) + k^2 u(\mathbf{x}) = 0$$

for  $\mathbf{x} \in \mathbb{R}^2 \setminus \bar{D}$ . Therefore,

$$\Delta u(\mathbf{x}) + k^2 u(\mathbf{x}) + n(\mathbf{x})k^2 u(\mathbf{x}) - n(\mathbf{x})k^2 u(\mathbf{x}) = 0,$$

and hence

$$\Delta u(\mathbf{x}) + n(\mathbf{x})k^2 u(\mathbf{x}) = (n(\mathbf{x}) - 1)k^2 u(\mathbf{x}), \quad \mathbf{x} \in \mathbb{R}^2 \setminus \bar{D}.$$

That is,  $u$  is the solution to the inhomogeneous problem given in Definition 4.1.1 for some arbitrary function  $n(\mathbf{x})$  having compact support  $\Omega$ , in the special case where



$D$  is the circle centered at the origin with radius  $R$ , with boundary condition (4.2)

$$u(R, \theta) = H_1^{(1)}(Rk)e^{i\theta},$$

and right hand side

$$g(\mathbf{x}) = (n(\mathbf{x}) - 1)k^2 u(\mathbf{x}).$$

In that case, the far field corresponding to  $u$  is given by

$$u_\infty(\theta) = \sqrt{\frac{1}{\pi k}}(i - 1)e^{i\theta}.$$

In Tables 4.2–4.3, we solve the inhomogeneous problem for the above special case using the coupled FEM-BEM technique, and then measure the  $L^2$  error in the far field as in Section 3.4.3. In Table 4.2 we fix values for the number of points  $N$  used in the Nyström scheme to highlight the effect of refining the mesh-size  $h$ . In Table 4.3 we fix values for  $h$  to analyze the effect of varying  $N$ . We use the same values for  $N$  and  $h$  from Chapter 3, because the numerical schemes we describe later in the thesis will require the forward medium problem and the inhomogeneous problem to be solved conjointly. For both tables, we take  $R = 0.6$  and the function  $n(\mathbf{x})$  to be

$$n(\mathbf{x}) = \begin{cases} |\mathbf{x}| & \text{if } \mathbf{x} \in \Omega, \\ 1 & \text{if } \mathbf{x} \in \mathbb{R}^2 \setminus B. \end{cases}$$

We have also provided a visual comparison between the true solution and the coupled FEM-BEM solution when  $k = \pi$ ,  $N = 13$ ,  $h = 0.003125$  in Figure 4.1. Note the solution has a distinct spiral pattern, which is due to the radial  $H_1^{(1)}(\pi r)$  component of the solution.

$h$	Error	$h$	Error	$h$	Error
0.1	2.1822e-3	0.1	1.3529e-2	0.1	5.1349e-2
0.05	5.0109e-4	0.05	2.4394e-3	0.05	1.2526e-2
0.025	1.3904e-4	0.025	6.8038e-4	0.025	2.7014e-3
0.0125	3.2580e-5	0.0125	1.5435e-4	0.0125	7.2999e-4
0.00625	7.9003e-6	0.00625	4.7100e-5	0.00625	1.9145e-4
0.003125	1.9129e-6	0.003125	8.3927e-6	0.003125	3.8306e-5

Table 4.2: Maximum error in the far field between the true and numerical solution for  $k = \frac{\pi}{2}$  (left),  $k = \pi$  (center) and  $k = 2\pi$  (right). We have fixed  $N = 9$  (left),  $N = 13$  (center) and  $N = 21$  (right).

$N$	Error	$N$	Error	$N$	Error
3	5.3793e-2	7	2.4852e-5	15	3.8530e-5
4	1.8240e-3	8	9.1569e-6	16	3.6309e-5
5	3.3598e-5	9	9.2867e-6	17	3.8106e-5
6	3.6739e-6	10	8.3793e-6	18	3.7234e-5
7	3.7458e-6	11	2.6298e-5	19	3.6356e-5
8	3.6189e-6	12	2.3589e-5	20	3.7610e-5
9	1.9129e-6	13	8.3927e-6	21	3.8306e-5

Table 4.3: Maximum error in the far field between the true and numerical solution for  $k = \frac{\pi}{2}$  (left),  $k = \pi$  (center) and  $k = 2\pi$  (right). We have fixed  $h = 0.003125$  for all three tables.

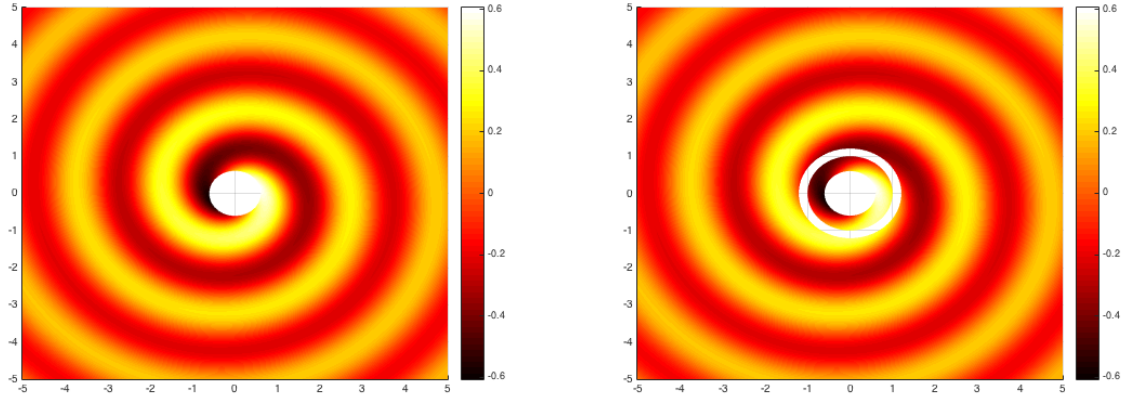


Figure 4.1: True solution  $u(r, \theta) = H_1^{(1)}(\pi r)e^{i\theta}$  to the inhomogeneous problem on the left, coupled FEM-BEM solution on the right. Here  $k = \pi$ ,  $h = 0.003125$ ,  $N = 13$ , and the far field error is  $8.4 \times 10^{-6}$ . Note that the method of Surface Integral Equations cannot compute the exterior field close to the boundary because the integrand in (3.21) becomes singular. This corresponds to the white annulus region in the figure on the right, in which the exterior field has not been computed.

### 4.4.1 Discussion

We deduce from the results of the previous section that our implementation of the coupled FEM-BEM technique is highly effective in accurately solving the inhomogeneous problem. We note that the results in Table 4.1 are qualitatively similar to those of Table 3.2, and the convergence in both these tables is significantly slower than that of Table 3.1. It follows that when we solve the inhomogeneous problem using our coupled FEM-BEM technique, the error from the Nyström scheme will eventually become dominated by the error from the FEM. For this reason, we believe we can solve the inhomogeneous problem more efficiently by incorporating a higher order FEM into our numerical method.

Knowing how to choose the parameters  $h$  and  $N$  in our numerical method depends on the level of accuracy required. To achieve an error of  $10^{-6}$  when  $k = \frac{\pi}{2}$  for example, we must choose  $h$  and  $N$  so that a balanced error of  $10^{-6}$  occurs in the computation of operators  $G_e, G_i$  and  $G_p$ .

Tables 3.2 and 4.1 suggest that to achieve an error of  $10^{-6}$ , we must take  $h = 0.003125$ . From Table 3.1,  $N = 7$  seems sufficient to achieve an error of  $10^{-6}$  in the Nyström scheme. The fact that this particular choice of parameters works is then verified in Table 4.3.

We mentioned in the previous chapter that the accuracy of the FEM depends on using a fixed number of elements per wavelength in the FEM mesh. This explains the visible trends in Tables 4.1 and 4.2 of the error becoming larger for fixed  $h$  as  $k$  increases.

# Chapter 5

## Inverse Medium Problem for Non-Stratified Media

In this chapter we solve the inverse of the forward problem discussed in Chapter 3, in the special case where the obstacle  $D$  within  $\Omega$  is absent.

We therefore take  $D = \emptyset$  so that  $\Omega = B$  and consider the interaction of an incident plane wave

$$u^{\text{inc}}(\mathbf{x}) = e^{ik\mathbf{x}\cdot\hat{\mathbf{d}}} \quad (5.1)$$

with the two dimensional heterogeneous medium described in Chapter 3 with refractive index  $n(\mathbf{x})$  for  $\mathbf{x} \in \mathbb{R}^2$ , where  $k$  denotes the incident wavenumber, and the unit vector  $\hat{\mathbf{d}}$  is the plane wave direction.

Recall from Chapter 3 that we make the mild assumption that the heterogeneity of the medium is contained in the unit disk  $B$  centered at the origin. Outside the unit disk the refractive index is constant, and we normalize so that

$$n(\mathbf{x}) = 1, \quad \mathbf{x} \in \mathbb{R}^2 \setminus B.$$

Furthermore, we continue to describe the refractive index using the function  $m(\mathbf{x}) :=$

---

$1 - n(\mathbf{x})$ , because it will be convenient to work with functions having compact support.

Following the notation of Chapter 3, interaction of the incident field  $u^{\text{inc}}$  with the scatterer produces an induced field  $u^i$  in  $B$  and a scattered field  $u^s$  in  $\mathbb{R}^2 \setminus B$ . Note here it is the heterogeneous medium inside  $B$  we refer to as the scatterer, because  $D = \emptyset$  and thus the heterogeneity is the sole cause of the scattered wave  $u^s$ . By Definition 3.0.1, the scattered field satisfies the homogeneous Helmholtz equation

$$\Delta u^s(\mathbf{x}) + k^2 u^s(\mathbf{x}) = 0, \quad \mathbf{x} \in \mathbb{R}^2 \setminus B, \quad (5.2)$$

and the Sommerfeld radiation condition [23, Equation (3.85)]

$$\lim_{|\mathbf{x}| \rightarrow \infty} \sqrt{|\mathbf{x}|} \left( \frac{\partial u^s}{\partial \mathbf{x}}(\mathbf{x}) - i k u^s(\mathbf{x}) \right) = 0 \quad (5.3)$$

uniformly with respect to the direction  $\hat{\mathbf{x}}$ , while  $u^i$  satisfies the heterogeneous Helmholtz equation

$$\Delta u^i(\mathbf{x}) + k^2 n(\mathbf{x}) u^i(\mathbf{x}) = 0, \quad \mathbf{x} \in B. \quad (5.4)$$

For a given incident direction  $\hat{\mathbf{d}}$  and refractive index  $m(\mathbf{x})$ , the *forward problem* we discussed in Chapter 3 is to compute the corresponding far field  $u_\infty(\hat{\mathbf{x}}, m)$ . To solve the corresponding *inverse problem*, we must compute the refractive index  $m$  given far field data  $f_\infty$ . This equates to solving the ill-posed and nonlinear equation

$$\mathcal{F}_d(m) = f_\infty, \quad (5.5)$$

we discussed in Chapter 2, where the operator  $\mathcal{F}_d : m \mapsto u_\infty(\hat{\mathbf{x}}, m)$  maps the function  $m(\mathbf{x})$  to the corresponding far field  $u_\infty(\hat{\mathbf{x}}, m)$ . Note the operator  $\mathcal{F}_d$  is simply denoted as  $\mathcal{F}$  in [23, Chapter 10]; we have used the subscript  $d$  to emphasise

---

the dielectric nature of the scatter for which the operator is defined.

The extensive literature on inverse scattering problems (see [23] and references therein) is predominantly focused on the problem of reconstructing the shape (or impedance) of impenetrable scatterers. The theory for the inverse medium problem is comparatively undeveloped, and uniqueness results do not sharply specify the type or quantity of data required [23, Section 10.2]. However, Newton-type methods have been successfully applied to the inverse medium problem. In particular, for square (or cubic) domains the quasi-Newton method was applied to compute the tensor product Fourier coefficients of the refractive index [46, 47, 48]. For three dimensional spherical domains, the refractive index was represented using a tensor product of the spherical harmonics and splines [52, 53]. In the latter case, the scattering problem was reformulated using the *Lippmann–Schwinger* volume integral equations, and the resulting nonlinear problem was solved using the Levenburg–Marquardt iteration.

The above articles assumed the refractive index  $m(\mathbf{x})$  to be radially symmetric; thus being applicable only to stratified media. We solved the inverse problem, (5.5), for both stratified and non-stratified media in [7], using the iterative solver described in Chapter 2, equipped with the coupled FEM-BEM technique (see Chapter 3) as the forward solver.

To forgo assumptions regarding the symmetry of  $m$ , we used the Logan–Shepp polynomials [71] as a basis for the high order approximation of the function  $m$  inside  $B$ . These polynomials are essentially functions of a single variable in a rotated frame of reference, and therefore don’t require  $m$  to possess any axis symmetry (unlike traditional basis options such as Fourier series). Although there are several other basis options available, Logan–Shepp polynomials along with Zernike polynomials are the most accurate in approximating non axis-symmetric functions [11]. We favoured the use of Logan–Shepp polynomials as these were recently used to successfully compute high order approximations on the disk for various elliptic PDE problems [4]. The-

oretically, these functions span the space of finite dimensional polynomials in two variables, yet we show in Section 5.3 they can efficiently approximate much more challenging functions.

In [7], we computed the Fréchet derivative using the method of finite-differences. In this chapter we vastly improve upon our approach in [7] by using the novel coupled FEM-BEM technique for the inhomogeneous Helmholtz equation discussed in Chapter 3 instead, to numerically compute the Fréchet derivative. This approach drastically reduces computation time, and allows us to use higher order approximations to obtain improved reconstructions.

## 5.1 Logan-Shepp Polynomials

As explained in Chapter 2, given an approximate solution  $m$  to (5.5), we seek an improved approximation  $m + q$  by solving the linearized equation

$$\mathcal{F}_d(m) + \mathcal{F}'_d(m)q = f_\infty, \quad (5.6)$$

where  $\mathcal{F}'_d$  denotes the Fréchet derivative of  $\mathcal{F}_d$  at  $m$ . Equation (5.6) is discretized using an ansatz space with basis

$$\mathbb{P}^N := \{P_{l,j} : l \leq j, j = 0, 1, 2, \dots, N\},$$

and collocation at  $S$  points

$$\hat{\mathbf{x}}_s = \left( \cos \frac{2\pi s}{S}, \sin \frac{2\pi s}{S} \right), \quad s = 0, 1, \dots, S-1,$$

where

$$P_{l,j}(x_1, x_2) = \frac{1}{\sqrt{\pi}} U_j \left( x_1 \cos \frac{l\pi}{j+1} + x_2 \sin \frac{l\pi}{j+1} \right), \quad (x_1, x_2) \in B,$$

denote the Logan-Shepp Polynomials, and  $U_j$  is the  $j$ -th degree Chebyshev polynomial of the second kind [1, Chapter 22]. The Logan-Shepp polynomials are orthogonal on the disk  $B$ , and are used to approximate functions with high order accuracy (see Table 5.1). We show through numerical simulations in Section 5.3 that  $N = 15$  is sufficient to reconstruct the key features of the refractive index for a range of smooth and non-smooth heterogeneous media.

Our discrete approximations to  $q$  and  $m$  are thus

$$q_N(\mathbf{x}) = \sum_{j=0}^N \sum_{l=0}^j q_{l,j} P_{l,j}(\mathbf{x}) \quad \text{and} \quad m_N(\mathbf{x}) = \sum_{j=0}^N \sum_{l=0}^j m_{l,j} P_{l,j}(\mathbf{x}), \quad (5.7)$$

where  $(q_{l,j})_{0 \leq l \leq j \leq N}$  and  $(m_{l,j})_{0 \leq l \leq j \leq N}$  represent the spectral coefficients of  $q_N$  and  $m_N$  with respect to  $\mathbb{P}^N$  respectively.

## 5.2 Reformulating the Inverse Problem as a Discrete Nonlinear Equation

Following Section 2.2.1, we solve the discretized equations

$$[\mathcal{F}_d(m_N)](\hat{\mathbf{x}}_s) + [\mathcal{F}'_d(m_N)q_N](\hat{\mathbf{x}}_s) = f_\infty(\hat{\mathbf{x}}_s), \quad s = 0, 1, \dots, S-1,$$

by reformulating them as a linear system

$$F\mathbf{m} + F'_m \mathbf{q} = \mathbf{f}, \quad (5.8)$$

where  $\mathbf{m} = (m_{0,1}, m_{1,1}, \dots, m_{N-1,N}, m_{N,N})^T$ ,  $\mathbf{q} = (q_{0,1}, q_{1,1}, \dots, q_{N-1,N}, q_{N,N})^T$  and  $\mathbf{f} = (\mathbf{f}_0, \mathbf{f}_1, \dots, \mathbf{f}_{S-1})^T$ . We solve the ill-posed equation (5.8) using the Levenburg-



Marquardt scheme (see Chapter 2) which yields the regularized solution

$$\mathbf{q} = [\alpha I + (F'_m)^T (F'_m)]^{-1} (F'_m)^T [\mathbf{f} - F\mathbf{m}],$$

where  $I$  is the identity matrix and the regularization parameter  $\alpha$  is chosen according to the Morozov discrepancy principle.

To compute  $F\mathbf{m}$ , we use the coupled FEM-BEM scheme from Chapter 2. To compute the Fréchet derivative, we use the following result [23, p. 333]:

**Theorem 5.2.1.** *The operator  $\mathcal{F}_d$  is Fréchet differentiable. The derivative is given by*

$$(\mathcal{F}_d)'_m q = \omega_\infty,$$

where  $\omega_\infty$  is the far field pattern of the radiating solution  $\omega \in H^2_{\text{loc}}(\mathbb{R}^2)$  to

$$\Delta\omega + k^2 n\omega = k^2 uq \quad \text{in } \mathbb{R}^2, \tag{5.9}$$

$u \in C(\mathbb{R}^2)$  is the unique solution to (5.2)–(5.4), and  $q$  has compact support  $B$ .

We compute the Fréchet derivative by solving the inhomogeneous Helmholtz equation (5.9) using the coupled FEM-BEM scheme in Chapter 4.

## 5.3 Numerical Results

In this section we present reconstructions for various challenging media that we used in [7]. We consider the following test problems:

- **Bowl:** The heterogeneous region is the off-centre disk of radius  $1/2$  centered

at  $\mathbf{c} = (0.3, 0.3)$ . The continuous refractive index function is

$$m(\mathbf{x}) = \begin{cases} 2 - 4|\mathbf{x} - \mathbf{c}|^2, & \text{for } |\mathbf{x} - \mathbf{c}| < 1/2, \\ 1, & \text{otherwise.} \end{cases}$$

- **Ellipse:** The heterogeneous region is contained inside an ellipse. The discontinuous refractive index function is

$$m(\mathbf{x}) = \begin{cases} 1.21, & \text{for } \frac{x_1^2}{4^2} + \frac{x_2^2}{5^2} \leq \frac{1}{10^2}, \\ 1, & \text{otherwise.} \end{cases}$$

- **Three disks:** The heterogeneous region comprises three disks of radius  $1/4$  and centres  $c_1 = (0.4, 0)$ ,  $c_2 = (-0.2, 0.346)$  and  $c_3 = (0.2, -0.346)$ . The discontinuous refractive index function is

$$m(\mathbf{x}) = \begin{cases} 1.21, & \text{for } |\mathbf{x} - \mathbf{c}_1| < 1/4, \\ 1.21, & \text{for } |\mathbf{x} - \mathbf{c}_2| < 1/4, \\ 1.44, & \text{for } |\mathbf{x} - \mathbf{c}_3| < 1/4, \\ 1, & \text{otherwise.} \end{cases}$$

For the bowl problem, we compute the far field using the coupled FEM-BEM technique from Chapter 3. To avoid the so called *inverse crime* of using data generated from the forward solver for the inversion, we add Gaussian noise to generate the reference data. That is, for  $s = 0, 1, \dots, S - 1$ , we add noise  $x_s + y_s i$  to the simulated data  $\mathbf{f}_s$  where  $x_s, y_s$  for  $s = 0, 1, \dots, S - 1$ , are independent samples of the Gaussian distribution with zero mean and variance  $\sigma^2$ . We visualise the computed far field against the reference far field in Figure 5.1.

For the discontinuous ellipse and three-disks problem, we generate the reference far field using solvers independent of our coupled FEM-BEM code. In particular, the reference data for the three-disks problem is generated using a multiple scattering

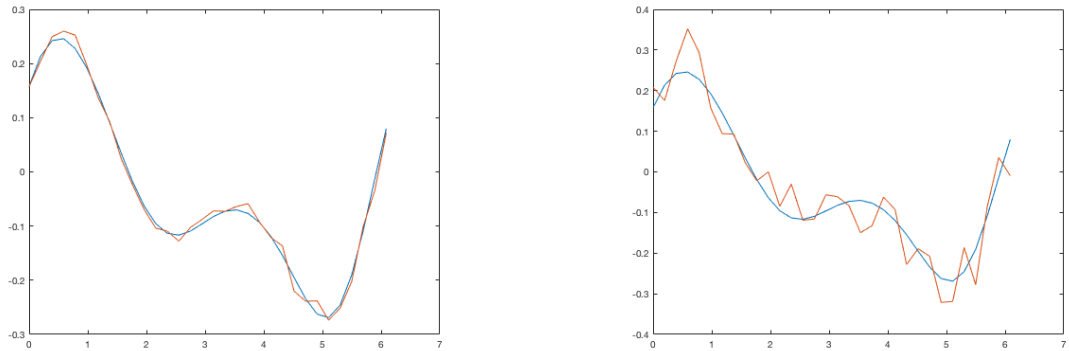


Figure 5.1: Plot of the real part of the far field computed by the forward solver (blue) and the reference data generated by adding Gaussian noise (red), for the ‘bowl’ test problem. In the figure on the left,  $\sigma = 1 \times 10^{-2}$  and the mean signal to noise ratio is 1 : 0.1278. In the figure on the right,  $\sigma = 5 \times 10^{-2}$  and the mean signal to noise ratio is 1 : 0.4447.

version of the Mie series. For the discontinuous ellipse problem, the reference data is generated using a surface integral equation formulation [8] that we solve using a high order Nyström scheme [23, Section 3.5].

In Table 5.1 we demonstrate the small number of degrees of freedom required to approximate the refractive indexes of our test media using the Logan–Shepp polynomials. In particular, we tabulate the relative  $L^2$  error in the discrete orthogonal projection of the refractive index. In practice, the  $L^2$  norm is approximated using a Gauss-rectangle rule with more than 20 000 points in the disk.

Motivated by the results in Table 5.1, we apply our algorithm to reconstruct the three test media from far field data, using polynomials of degree  $N = 15$  in the Logan–Shepp expansion. We tabulate the relative  $L^2$  errors of the reconstructed refractive index  $m(\mathbf{x})$  for each test problem in Table 5.2. There we also recall our previous results for these test problems published in [7]. Comparing the two sets of results side by side, we notice a significant improvement of the results we achieved in [7], which is due to our implementation of the coupled FEM-BEM technique in computing the Fréchet derivative.

degree $N$	d.o.f	error bowl	error ellipse	error three disks
5	21	6.6%	4.3%	9.1%
10	66	2.5%	3.3%	5.5%
15	136	1.4%	2.6%	5.3%

Table 5.1: Relative  $L^2$  error of the discrete orthogonal projection of the refractive index against number of degrees of freedom (d.o.f.) i.e. the number of Logan-Shepp polynomials which form the orthogonal basis (d.o.f is given by  $\frac{(N+1)(N+2)}{2}$ ). Note the convergence for the ellipse and three-disks problems are slower than the bowl, and this is because the refractive indexes for these two media are discontinuous.

We also visualize the reconstructions for each test problem in Figures 5.2–5.5. For each test problem we get excellent reconstructions of the key features of the media, including the sizes, locations and refractive-index values of all present inhomogeneities.

medium	noise $\sigma$	error $k = \pi$	error $k = 2\pi$	medium	noise $\sigma$	error $k = \pi$	error $k = 2\pi$
bowl	$1 \times 10^{-2}$	8.1%	15%	bowl	$1 \times 10^{-2}$	7.3%	9.0%
	$5 \times 10^{-2}$	16%	24%		$5 \times 10^{-2}$	10%	8.2%
ellipse	0	9.4%	8.9%	ellipse	0	5.7%	5.9%
three disks	0	18%	13%	three disks	0	16%	12%

Table 5.2: Relative  $L^2$  error of the reconstructed refractive index  $m(\mathbf{x})$  in the unit disk using Logan-Shepp Polynomials of degree 15. Results on the left are those published in [7], in which we computed the Fréchet derivative using the method of finite-differences. On average, the CPU times for those results were 3.2 hours (when  $k = \pi$ ) and 12.3 hours (when  $k = 2\pi$ ), using Matlab with the parallel computing toolbox, running on a desktop machine with a quad-core 2.8 GHz Intel Core i7 processor. The results on the right were generated using the methods discussed in this chapter i.e. computing the Fréchet derivative using the coupled FEM-BEM technique as explained in Chapter 3. On average, the CPU time was 5 minutes (when  $k = \pi$ ) and 10 minutes (when  $k = 2\pi$ ).

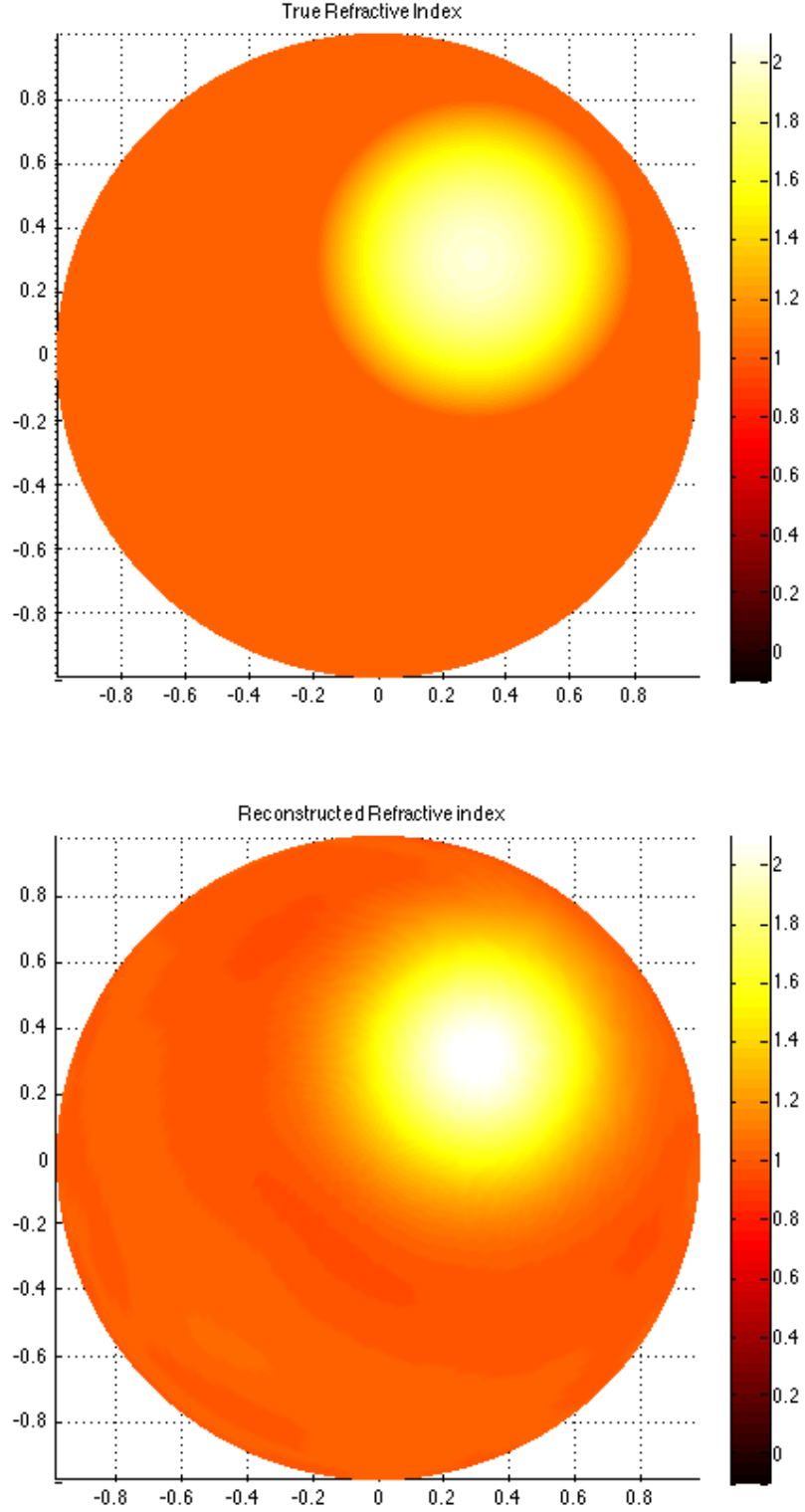


Figure 5.2: Reconstruction of the refractive index  $m(\boldsymbol{x})$  in the unit disk for the bowl test problem ( $k = \pi$ ) with noise parameter  $\sigma = 1 \times 10^{-2}$  using 6 incident directions. Relative  $L^2$  error is 7.28%.

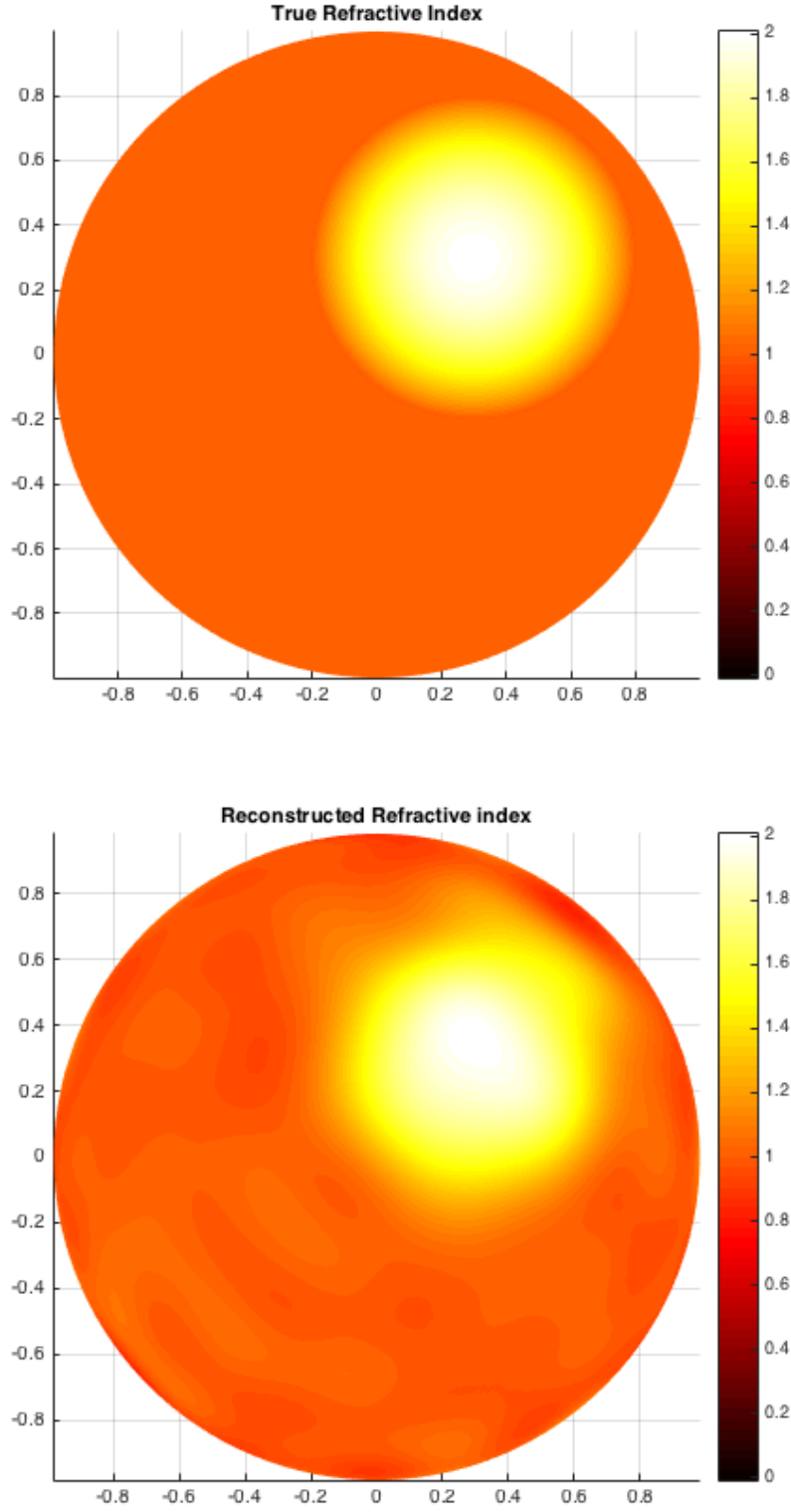


Figure 5.3: Reconstruction of the refractive index  $m(\mathbf{x})$  in the unit disk for the bowl test problem ( $k = 2\pi$ ) with noise parameter  $\sigma = 5 \times 10^{-2}$  using 6 incident directions. Relative  $L^2$  error is 8.23%.

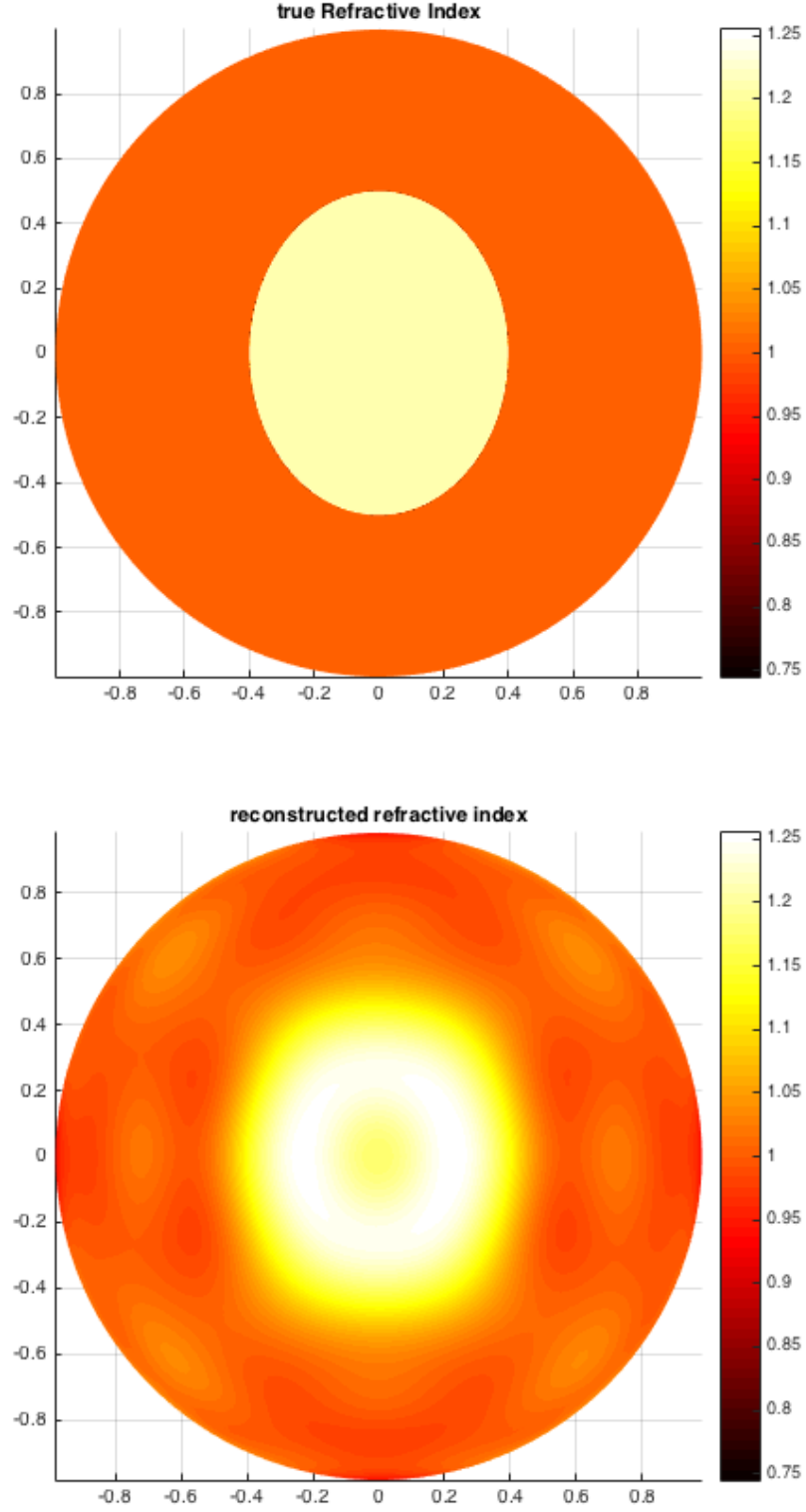


Figure 5.4: Reconstruction of the refractive index  $m(\mathbf{x})$  in the unit disk for the discontinuous ellipse test problem ( $k = 2\pi$ ) using 4 incident directions. Relative  $L^2$  error is 5.97%.

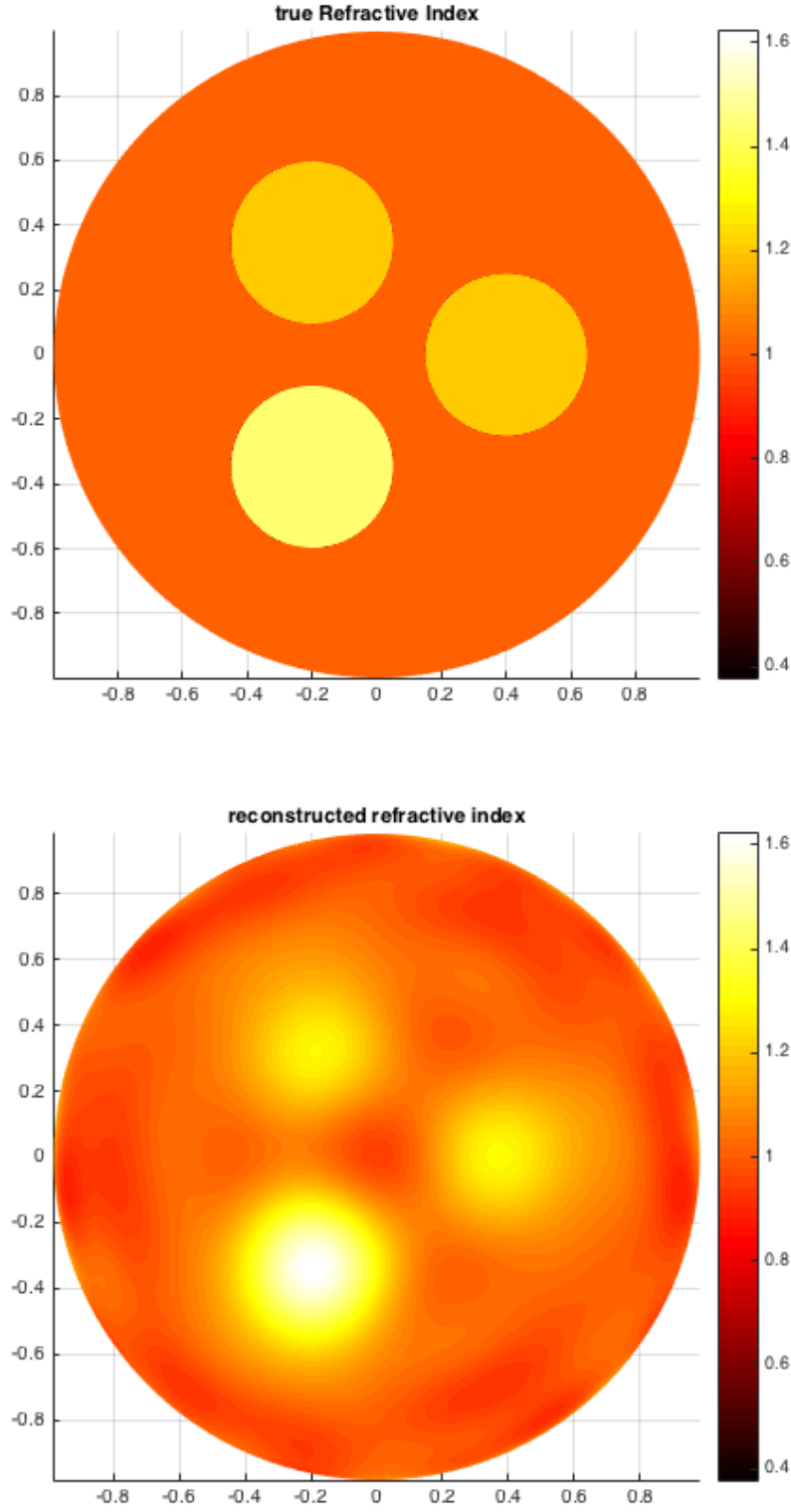


Figure 5.5: Reconstruction of the refractive index  $m(\mathbf{x})$  in the unit disk for the three-disks test problem ( $k = 2\pi$ ) using 6 incident directions. Relative  $L^2$  error is 12.23%.



### 5.3.1 Discussion

Figures 5.2–5.5 illustrate visually the quality of reconstructions which correspond to the relative errors of Table 5.2. We see that a relative  $L^2$  error of less than 10% translates to an accurate reconstruction, in the sense that the location and magnitude of the heterogeneities are reconstructed almost exactly. When the relative  $L^2$  error goes slightly above 10% (see Figure 5.5), the reconstruction is noticeably poorer. Even though the locations of the heterogeneities have been recognised, their magnitude is not clearly reconstructed like in Figures 5.2–5.4.

We notice in the reconstructions of Figures 5.2 and 5.3 that there are patches having unexpected colours which appear in the part of the medium which should be homogeneous. We also notice such patches appearing in the outer edges of the reconstruction in Figure 5.4. Also in Figure 5.4, there is some alternation of colour in the center of the reconstructed image. Further unexpected patches are evident in Figure 5.5. We hypothesize this is due to a form of Gibbs’ phenomenon, as we are approximating the refractive index functions using a spectral basis. We suspect that although higher order modes may achieve a higher overall quality of reconstruction, they will increasingly induce odd irregularities occurring throughout the reconstruction.

There is a noticeable difference in the error of the ‘three disks’ problem compared to the other test problems. We hypothesize that perhaps more iterations are required in Newton’s method for the ‘three disks’ problem to achieve the same reconstruction quality as the other test problems.

Perhaps the most interesting result from the previous section is the noticeable difference of errors in Table 5.2 between the results published in [7], and the results achieved in this chapter. Both approaches utilized the coupled FEM-BEM technique, but we improved on the method of finite-differences in [7] by computing the Fréchet derivative using its analytic expression and our novel FEM-BEM scheme

from Chapter 4. Thus by improving the forward solver, we were able to achieve higher quality reconstructions. For this reason, it might be possible to improve our results once more by incorporating a higher order FEM, although this is just speculation which requires further research.

We note that a relative  $L^2$  error of approximately 1% corresponds roughly to an error in the far field error of magnitude  $10^{-4}$ . Therefore it is sufficient to choose the parameters  $N$  and  $h$  for the forward solver so that the far field error is at most  $10^{-4}$ . Increasing  $N$  or refining  $h$  any further won't yield better reconstructions, because at best the relative error of the reconstruction is that of the projection (which is at least 1.4% from Table 5.1 for  $N = 15$ ). Doing so will only make computations more numerically costly unnecessarily.

# Chapter 6

## Inverse Coated Problem

In this chapter we numerically solve the inverse of the forward problem from Chapter 3 and for the sake of consistency, we use the same notation as before. This equates to solving the ill-posed and nonlinear equation

$$\mathcal{F}_c(m) = f_\infty, \tag{6.1}$$

where the operator

$$\mathcal{F}_c : m \mapsto u_\infty(\hat{\mathbf{x}}, m)$$

maps the function  $m(x)$  to the corresponding far field  $u_\infty(\hat{\mathbf{x}}, m)$  of the solution to the forward problem. Note that  $\mathcal{F}_c$  is analogous to the operator  $\mathcal{F}$  studied in [23, Chapter 10]; we have utilized the subscript  $c$  because in this context  $D$  is a ‘coated’ scatterer. We solve (6.1) using our modified Newton-type solver described in Chapter 2. This requires solving the following three sub-problems, which we discuss in this chapter:

- Finding a suitable ansatz  $\mathbb{A}^N$  to approximate  $m$  on  $\Omega$ .
- Deriving an analytic representation for the Fréchet derivative  $\mathcal{F}'_c(m)$ .
- Evaluating the discrete Fréchet derivative  $\mathcal{F}'_c(m_N)q_N$  for  $q_N \in \mathbb{A}^N$ .

Each problem is challenging in its own right, and constitutes an entirely new contribution in the literature.

## 6.1 Approximation Theory

We assume  $\Omega$  can be mapped bijectively into the rectangular reference domain  $R = [-1, 1] \times [0, 2\pi]$ . Note this assumption holds in our particular case of interest, where  $D$  is simply connected. This assumption then enables us to approximate functions on  $\Omega$  using the “Angular Legendre” orthogonal functions on  $R$  from Chapter 2.

Suppose  $T$  is a bijective mapping from  $\Omega$  into  $R$ . Then any point  $\mathbf{x} \in \Omega$  can be written as

$$\mathbf{x} = T^{-1}(u, v)$$

for some  $(u, v) \in R$ . We can therefore write any  $m$  defined on  $\Omega$  as

$$m(\mathbf{x}) = \hat{m}(u, v), \quad \mathbf{x} \in \Omega, \quad (u, v) = T\mathbf{x},$$

for  $\hat{m} = m \circ T^{-1}$  on  $R$ . Thus we can approximate the function  $m(\mathbf{x})$  on  $\Omega$  by approximating the function  $\hat{m}(u, v)$  on  $R$ , using the Angular Legendre functions.

Our approximation to  $m$  is given by

$$\hat{m}_N(u, v) = \sum_{s=0}^{N_1} \sum_{t=-N_2}^{N_2} a_{s,t} L_s(u) e^{itv}, \quad (6.2)$$

where  $N = (N_1 + 1)(2N_2 + 1)$  and

$$a_{s,t} = \frac{2s+1}{4\pi} \int_0^{2\pi} \int_{-1}^1 \hat{m}(u, v) L_s(u) e^{itv} du dv. \quad (6.3)$$

In practice this integral is then approximated using Gaussian Quadrature (see Ap-

pendix 9.7). We explicitly define  $T$  for when  $\partial D$  is a circle and square respectively below:

### **$\partial D$ is a circle**

Let  $\partial D$  be a circle centered at the origin with radius  $r_0 < 1$ . Then a bijective mapping from the annulus  $\Omega$  to  $R$  is given by

$$T_{r_0} : (r, \theta) \mapsto \left( \frac{2}{1 - r_0}(r - r_0) - 1, \theta \right).$$

Moreover, the inverse is given by

$$T_{r_0}^{-1}(r, \theta) = \left( \frac{1 - r_0}{2}(r + 1) + r_0, \theta \right).$$

### **$\partial D$ is a square**

Let  $D$  be a square with side length  $2l$ , where  $l < \frac{1}{\sqrt{2}}$ . Then a bijection  $T_{sq}$  from  $\Omega$  to  $R$  is given by

$$T_{sq} = T_{r_0} \circ T^*,$$

where

$$T^*(r, \theta) = \left( \frac{r_0}{1 - r_{min}}(r - 1) + 1, \theta \right), \quad r_{min}(\theta) \leq r \leq r_{max}(\theta) = 1,$$

maps  $\Omega$  to the annulus  $\{x^2 + y^2 = r^2 \mid r_0 \leq r \leq 1\}$ . Here

$$r_{\min}(\theta) = \begin{cases} l \csc \theta, & \text{for } \frac{\pi}{4} < \theta \leq \frac{3\pi}{4}, \\ -l \sec \theta, & \text{for } \frac{3\pi}{4} < \theta \leq \pi, \quad -\pi < \theta \leq -\frac{3\pi}{4}, \\ -l \csc \theta, & \text{for } -\frac{3\pi}{4} < \theta \leq -\frac{\pi}{4}, \\ l \sec \theta, & \text{for } -\frac{\pi}{4} < \theta \leq \frac{\pi}{4}. \end{cases}$$

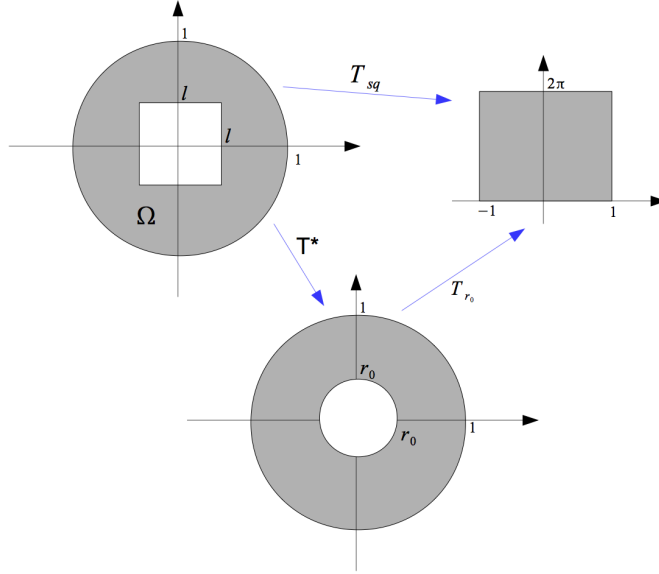


Figure 6.1: Visualization of the mapping  $T_{sq} = T_{r_0} \circ T^*$ .

In Figure 6.1 we visualise the mapping  $T_{sq}$  in the general case, while in Figure 6.2 we visualise  $\hat{m}$  when  $m(z) = |z|$ .

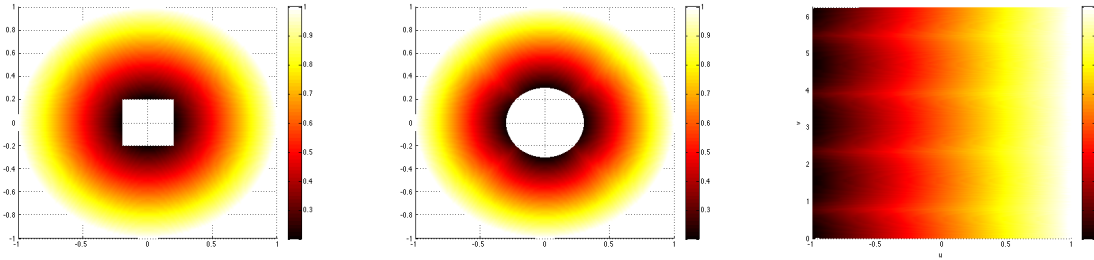


Figure 6.2: Visualization of the distance function  $m(z) = |z|$  in  $\Omega$  for square with sides of length  $2l = 0.4$  (left), under the transformation  $T^*$  with  $r_0 = 0.3$  (middle), and under the transformation  $T_{sq} = T_{r_0} \circ T^*$  (right).

## 6.2 An analytic representation for the Fréchet derivative

In this section we derive an analytic representation for the Fréchet derivative  $\mathcal{F}'_c(m)$  by establishing the *Lippmann-Schwinger* equation for the forward problem.

We extend the results in [23, Chapter 10] which are formulated over the unit disk  $B$  which is a  $C^2$  domain, to the region  $\Omega$  which is a Lipschitz domain. Although similar, our derivation requires more general formulations of the results utilized in [23, Chapter 10], particularly Green's identities and Green's representation formula. In Section 9.8 of the Appendix, we state the weaker forms (see [5, p.325], [34, p.102]) of Green's identities and then derive Green's Representation formula for Lipschitz domains, in the setting of Sobolev spaces.

### 6.2.1 The *Lippmann-Schwinger* Equation

**Lemma 6.2.1.** *If  $u \in H^2_{\text{loc}}(\mathbb{R}^2 \setminus \bar{D})$  is a solution of (3.2)–(3.4), then  $u$  is a solution of the *Lippmann-Schwinger* equation*

$$u = u^{\text{inc}} - k^2 \iint_{\mathbb{R}^2 \setminus \bar{D}} \Phi(\mathbf{x}, \mathbf{y}) m(\mathbf{y}) u(\mathbf{y}) \, d\mathbf{y}. \quad (6.4)$$

*Conversely, if  $u \in C(\mathbb{R}^2 \setminus \bar{D})$  is a solution of the *Lippmann-Schwinger* equation, then  $u \in H^2_{\text{loc}}(\mathbb{R}^2 \setminus \bar{D})$  and  $u$  is a solution of (3.2)–(3.4).*

*Proof.* Suppose  $u \in H^2_{\text{loc}}(\mathbb{R}^2 \setminus \bar{D})$  is a solution of (3.2)–(3.4), and that  $\mathbf{x} \in \mathbb{R}^2 \setminus \bar{D}$  is an arbitrary point. Furthermore, let  $B'$  be an open ball (with outward unit normal  $\mathbf{n}$ ) such that  $B'$  contains  $\Omega$  and  $\mathbf{x} \in B'$ . Then applying Green's representation

formula (Theorem 9.8.3) in  $B'$ , we get

$$u(\mathbf{x}) = \int_{\partial B' \cup \partial D} \left\{ \frac{\partial u}{\partial \mathbf{n}} \Phi(\mathbf{x}, \mathbf{y}) - u(\mathbf{y}) \frac{\partial \Phi}{\partial \mathbf{n}}(\mathbf{y}) \right\} ds(\mathbf{y}) - \iint_{B' \setminus \bar{D}} \{ \Delta u(\mathbf{y}) + k^2 u(\mathbf{y}) \} \Phi(\mathbf{x}, \mathbf{y}) d\mathbf{y},$$

From (3.2),

$$\Delta u(\mathbf{y}) + k^2 u(\mathbf{y}) = k^2 m(\mathbf{y}) u(\mathbf{y}), \quad \mathbf{y} \in B' \setminus \bar{D}.$$

Therefore,

$$u(\mathbf{x}) = \int_{\partial B' \cup \partial D} \left\{ \frac{\partial u}{\partial \mathbf{n}} \Phi(\mathbf{x}, \mathbf{y}) - u(\mathbf{y}) \frac{\partial \Phi}{\partial \mathbf{n}}(\mathbf{y}) \right\} ds(\mathbf{y}) - k^2 \iint_{B' \setminus \bar{D}} \Phi(\mathbf{x}, \mathbf{y}) m(\mathbf{y}) u(\mathbf{y}) d\mathbf{y}.$$

On the other hand, applying Green's representation formula to  $u^{\text{inc}}$  gives

$$u^{\text{inc}}(\mathbf{x}) = \int_{\partial B' \cup \partial D} \left\{ \frac{\partial u^{\text{inc}}}{\partial \mathbf{n}}(\mathbf{y}) \Phi(\mathbf{x}, \mathbf{y}) - u^{\text{inc}}(\mathbf{y}) \frac{\partial \Phi}{\partial \mathbf{n}}(\mathbf{y}) \right\} ds(\mathbf{y}).$$

By defining  $u^s(\mathbf{x}) = u^i(\mathbf{x}) - u^{\text{inc}}(\mathbf{x})$  for  $\mathbf{x} \in \Omega$ , it follows from Green's second identity and (3.3) that

$$\int_{\partial B' \cup \partial D} \left\{ \frac{\partial u^s}{\partial \mathbf{n}}(\mathbf{y}) \Phi(\mathbf{x}, \mathbf{y}) - u^s(\mathbf{y}) \frac{\partial \Phi}{\partial \mathbf{n}}(\mathbf{y}) \right\} ds(\mathbf{y}) = 0.$$

That is,

$$\begin{aligned} u &= u^{\text{inc}} - k^2 \iint_{B' \setminus \bar{D}} \Phi(\mathbf{x}, \mathbf{y}) m(\mathbf{y}) u(\mathbf{y}) d\mathbf{y} \\ &= u^{\text{inc}} - k^2 \iint_{\mathbb{R}^2 \setminus \bar{D}} \Phi(\mathbf{x}, \mathbf{y}) m(\mathbf{y}) u(\mathbf{y}) d\mathbf{y}, \end{aligned}$$

since the function  $m(\mathbf{y})$  has compact support  $\Omega \subset B' \setminus \bar{D}$ .



To prove the second part of the statement, suppose  $u \in C(\mathbb{R}^2 \setminus \bar{D})$  satisfies the *Lippmann-Schwinger* equation. If we define

$$u^s(\mathbf{x}) := -k^2 \iint_{\mathbb{R}^2 \setminus \bar{D}} \Phi(\mathbf{x}, \mathbf{y}) m(\mathbf{y}) u(\mathbf{y}) d\mathbf{y}$$

for  $\mathbf{x} \in \mathbb{R}^2 \setminus \bar{D}$ , then  $u^s$  will satisfy the Sommerfeld radiation condition (3.3). The remaining results follow from Theorems 8.1 and 8.2 of [23].  $\square$

We are now in a position to derive an analytic representation for the Fréchet derivative  $\mathcal{F}'_c(m)$ .

**Theorem 6.2.2.** *The operator  $\mathcal{F}'_c$  defined in (6.1) is Fréchet differentiable. The derivative is given by*

$$(\mathcal{F}'_c)'_m q = v_\infty,$$

where  $v_\infty$  is the far field pattern of the radiating solution  $v \in H^2_{\text{loc}}(\mathbb{R}^2 \setminus \bar{D})$  to

$$\begin{aligned} \Delta v + k^2 n v &= k^2 v q \quad \text{in } \mathbb{R}^2 \setminus \bar{D}, \\ v &= 0 \quad \text{on } \partial D, \end{aligned}$$

$u$  is the unique solution to (6.4), and  $q$  has compact support  $\Omega$ .

*Proof.* Suppose  $u$  is the unique solution to (6.4). Then by Lemma 6.2.1,  $u$  is the radiating solution to

$$\Delta \tilde{v} + k^2 n \tilde{v} = 0 \quad \text{in } \mathbb{R}^2 \setminus \bar{D}, \tag{6.5}$$

$$\tilde{v} = 0 \quad \text{on } \partial D. \tag{6.6}$$

From [23, p. 277], the far field pattern of  $u$  is given by

$$\mathcal{F}_c(m) = -\frac{k^2}{4\pi} \iint_{\mathbb{R}^2 \setminus \bar{D}} e^{-ik\mathbf{x} \cdot \mathbf{y}} m(\mathbf{y}) u(\mathbf{y}) d\mathbf{y}.$$

It follows that

$$\mathcal{F}_c(m + hq) = -\frac{k^2}{4\pi} \iint_{\mathbb{R}^2 \setminus \bar{D}} e^{-ik\mathbf{x} \cdot \mathbf{y}} [m + hq] w(\mathbf{y}) d\mathbf{y},$$

where  $w$  is the radiating solution to

$$\Delta w + k^2(1 - [m + hq])w = 0 \quad \text{in } \mathbb{R}^2 \setminus \bar{D}, \quad (6.7)$$

$$w = 0 \quad \text{on } \partial D. \quad (6.8)$$

Therefore,

$$\begin{aligned} \mathcal{F}_c(m + hq) - \mathcal{F}_c(m) &= -\frac{k^2}{4\pi} \iint_{\mathbb{R}^2 \setminus \bar{D}} e^{-ik\mathbf{x} \cdot \mathbf{y}} \{[m(\mathbf{y}) + hq(\mathbf{y})]w(\mathbf{y}) - m(\mathbf{y})u(\mathbf{y})\} d\mathbf{y} \\ &= -\frac{k^2}{4\pi} \iint_{\mathbb{R}^2 \setminus \bar{D}} e^{-ik\mathbf{x} \cdot \mathbf{y}} m(\mathbf{y})[w(\mathbf{y}) - u(\mathbf{y})] d\mathbf{y} - \frac{hk^2}{4\pi} \iint_{\mathbb{R}^2 \setminus \bar{D}} e^{-ik\mathbf{x} \cdot \mathbf{y}} q(\mathbf{y})w(\mathbf{y}) d\mathbf{y}. \end{aligned}$$

Then

$$\begin{aligned} \mathcal{F}'_c(m)q &= \lim_{h \rightarrow 0} \frac{\mathcal{F}_c(m + hq) - \mathcal{F}_c(m)}{h} \\ &= \lim_{h \rightarrow 0} \left\{ -\frac{k^2}{4\pi h} \iint_{\mathbb{R}^2 \setminus \bar{D}} e^{-ik\mathbf{x} \cdot \mathbf{y}} m(\mathbf{y})[w(\mathbf{y}) - u(\mathbf{y})] d\mathbf{y} - \frac{k^2}{4\pi} \iint_{\mathbb{R}^2 \setminus \bar{D}} e^{-ik\mathbf{x} \cdot \mathbf{y}} q(\mathbf{y})w(\mathbf{y}) d\mathbf{y} \right\} \\ &= -\frac{k^2}{4\pi} \iint_{\mathbb{R}^2 \setminus \bar{D}} e^{-ik\mathbf{x} \cdot \mathbf{y}} m(\mathbf{y}) \lim_{h \rightarrow 0} \left\{ \frac{w(\mathbf{y}) - u(\mathbf{y})}{h} \right\} d\mathbf{y} - \frac{k^2}{4\pi} \iint_{\mathbb{R}^2 \setminus \bar{D}} e^{-ik\mathbf{x} \cdot \mathbf{y}} q(\mathbf{y}) \left\{ \lim_{h \rightarrow 0} w(\mathbf{y}) \right\} d\mathbf{y} \\ &= -\frac{k^2}{4\pi} \iint_{\mathbb{R}^2 \setminus \bar{D}} e^{-ik\mathbf{x} \cdot \mathbf{y}} [m(\mathbf{y})v(\mathbf{y}) + q(\mathbf{y})u(\mathbf{y})] d\mathbf{y}, \end{aligned}$$

where  $v := u'_m q$  is the Fréchet derivative of  $u$  with respect to  $m$  (in the direction of

$q$ ). Thus by Lemma 6.2.1,  $\mathcal{F}'_c(m)q$  is the far field pattern of  $v$ , where

$$v + k^2 \iint_{\mathbb{R}^2 \setminus \bar{D}} \Phi(\mathbf{x}, \mathbf{y}) [m(\mathbf{y})v(\mathbf{y}) + q(\mathbf{y})u(\mathbf{y})] d\mathbf{y} = 0.$$

It follows from Theorem 8.1 of [23] that

$$\Delta v + k^2 v = k^2 [m(\mathbf{y})v(\mathbf{y}) + q(\mathbf{y})u(\mathbf{y})]$$

and thus  $\Delta v + k^2 v = k^2 uq$ . □

It follows that computing the Fréchet derivative requires finding the radiating solution to a boundary value problem (BVP) of the form

$$\begin{aligned} \Delta v(\mathbf{x}) + k^2 m(\mathbf{x})v(\mathbf{x}) &= g(\mathbf{x}), & \mathbf{x} \in \Omega, \\ \Delta v(\mathbf{x}) + k^2 v(\mathbf{x}) &= 0, & \mathbf{x} \in \mathbb{R}^2 \setminus B. \end{aligned} \tag{6.9}$$

We compute the solution of the inhomogeneous Helmholtz equation (6.9) using the coupled FEM-BEM scheme in Chapter 4.

## 6.3 Numerics

In this section, we consider three different media:

- **Bowl:** The heterogeneous region is the off-centre disk of radius  $1/2$  centered at  $\mathbf{c} = (0.3, 0.3)$ . The continuous refractive index function is

$$m(\mathbf{x}) = \begin{cases} 2 - 4|\mathbf{x} - \mathbf{c}|^2, & \text{for } |\mathbf{x} - \mathbf{c}| < 1/2, \\ 1, & \text{otherwise.} \end{cases}$$

This is the same ‘bowl’ test problem used in Section 5.3, with the exception that  $D \neq \emptyset$ . In particular, we consider the cases where  $D$  is the circle of

diameter 0.4 and  $D$  is the square of side length 0.4.

- **Three disks:** When  $D$  is the circle of diameter 0.4, we also consider another “three disks” problem, similar to that considered in Section 5.3. Here the heterogeneous region comprises three disks of radius 0.15, 0.175, 0.125, and centres  $c_1 = (0.65, 0)$ ,  $c_2 = (-0.424, 0.424)$ ,  $c_3 = (0, -0.5)$  respectively. That is, the discontinuous refractive index function is

$$m(\mathbf{x}) = \begin{cases} 1.44, & \text{for } |\mathbf{x} - \mathbf{c}_1| < 0.15, \\ 1.21, & \text{for } |\mathbf{x} - \mathbf{c}_2| < 0.175, \\ 1.625, & \text{for } |\mathbf{x} - \mathbf{c}_3| < 0.125, \\ 1, & \text{otherwise.} \end{cases}$$

- **Periodic:** For the third test problem, we take  $D$  to be the square of side length 0.4 and set  $m(\mathbf{x})$  to be the periodic function  $m(r, \theta) = 1.5 + 0.5 \sin(2\theta)$ . From this point forward, we refer to this test problem as the ‘periodic’ problem.

We begin by demonstrating the accuracy of the Angular Legendre Polynomials in approximating the refractive indexes of the above test media in Table 6.1. There we tabulate the relative  $L^2$  error in the discrete orthogonal projection of each refractive index, by approximating the  $L^2$  norm using a Gauss-rectangle rule with more than 20 000 points in  $\Omega$ . We observe that although the Angular Legendre polynomials require more degrees of freedom than the Logan-Shepp polynomials from Chapter 5, they’re still able to produce highly accurate approximations of our test functions.

Next we provide reconstructions for each test problem. For the bowl and periodic test problems, we generate the far field using the coupled FEM-BEM technique from Chapter 3. Much like Chapter 5, we avoid the so called *inverse crime* when generating the reference data by adding Gaussian noise to the far field produced from the forward solver for the inversion. We visualise the computed far field against the reference far field in Figures 6.3-6.5 for the bowl and periodic test problems.

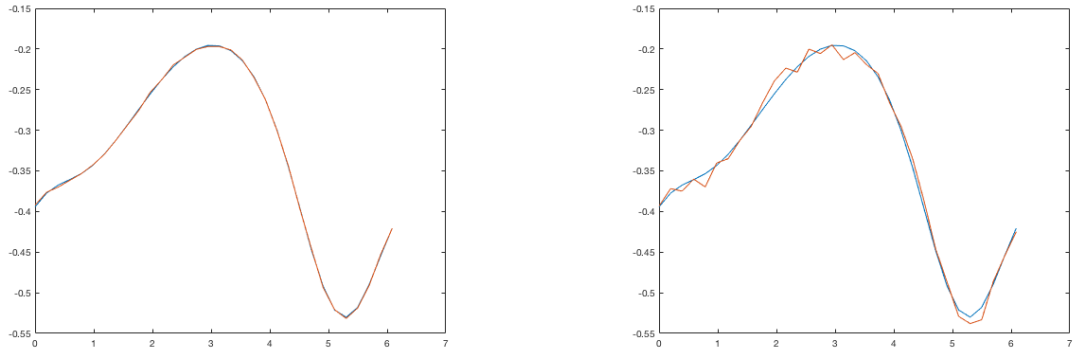


Figure 6.3: Plot of the real part of the far field computed by the forward solver (blue) and the reference data generated by adding Gaussian noise (red), for the ‘bowl’ test problem when  $D$  is the circle of diameter 0.4. In the figure on the left,  $\sigma = 1 \times 10^{-3}$  and the mean signal to noise ratio is 1 : 0.0031. In the figure on the right,  $\sigma = 1 \times 10^{-2}$  and the mean signal to noise ratio is 1 : 0.0214.

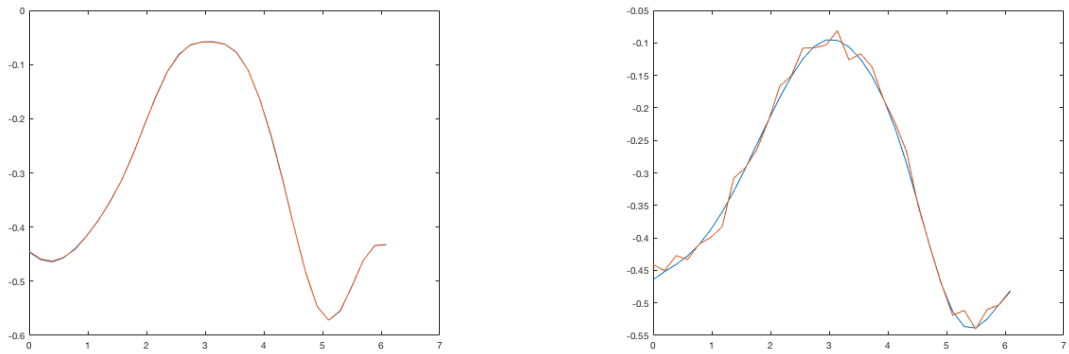


Figure 6.4: Plot of the real part of the far field computed by the forward solver (blue) and the reference data generated by adding Gaussian noise (red), for the ‘bowl’ test problem when  $D$  is the square of side length 0.4. In the figure on the left,  $\sigma = 1 \times 10^{-3}$  and the mean signal to noise ratio is 1 : 0.0035. In the figure on the right,  $\sigma = 1 \times 10^{-2}$  and the mean signal to noise ratio is 1 : 0.0418.

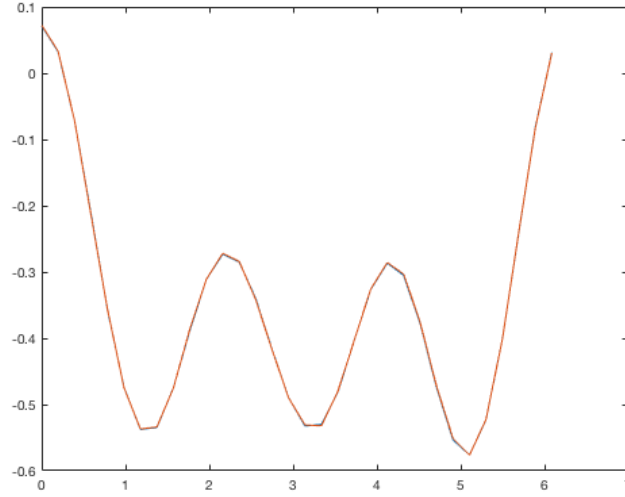


Figure 6.5: Plot of the real part of the far field computed by the forward solver (blue) and the reference data generated by adding Gaussian noise (red), for the ‘periodic’ test problem. Here  $\sigma = 1 \times 10^{-3}$  and the mean signal to noise ratio is 1 : 0.0043.

For the three-disks problem, the reference data is generated using a multiple scattering version of the Mie series. Visualizations of our reconstructions for each test problem are provided in Figures 6.6 - 6.9, and we provide additional results in Table 6.2. Similarly to Chapter 5, we see that we achieve excellent reconstructions for each test problem.

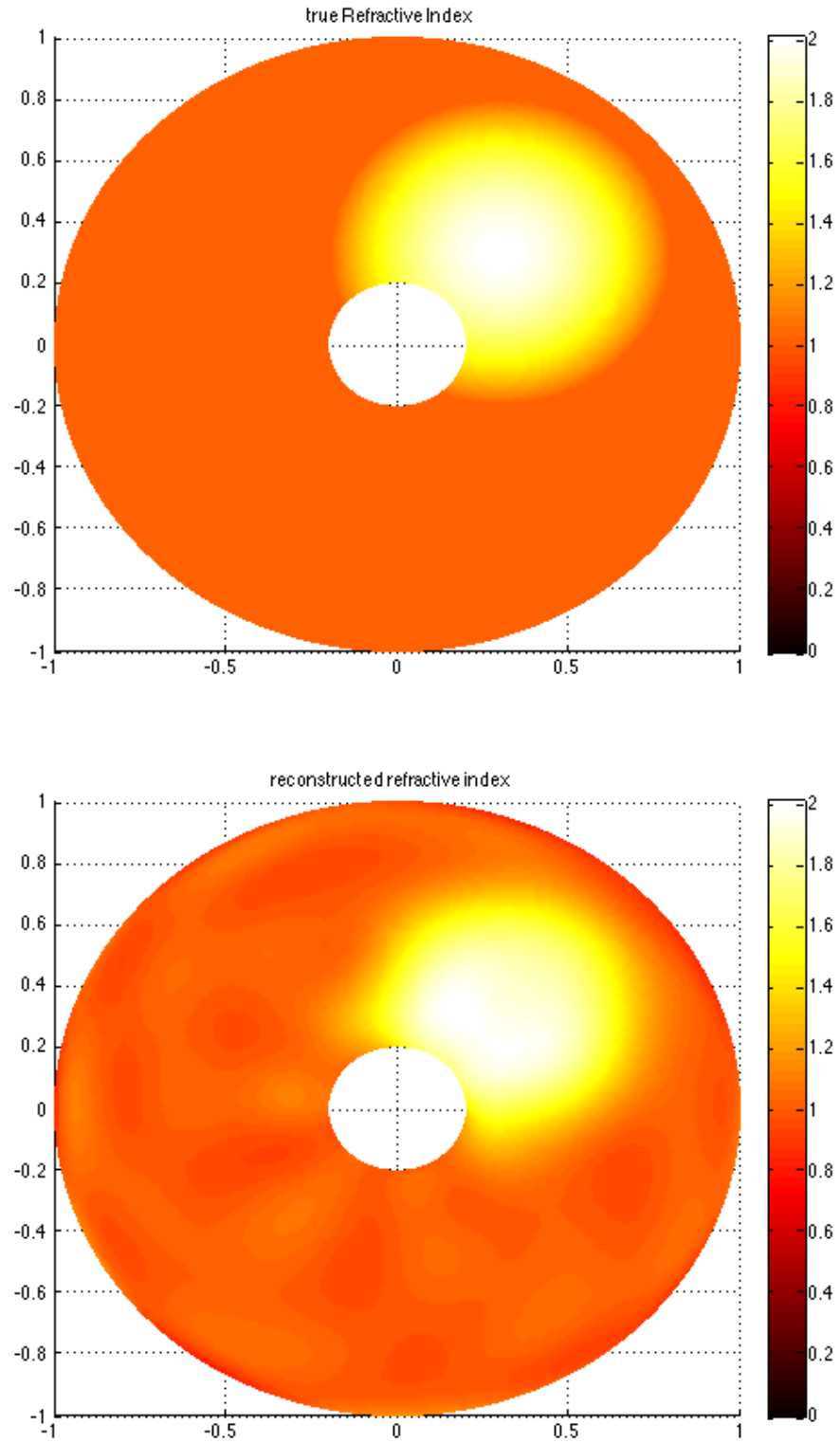


Figure 6.6: Reconstruction of the refractive index  $m(\mathbf{x})$  for the bowl test problem ( $k = \pi$ ) with noise parameter  $\sigma = 1 \times 10^{-3}$  using degree 7 and 4 incident directions. Relative  $L^2$  error is 7.71%.

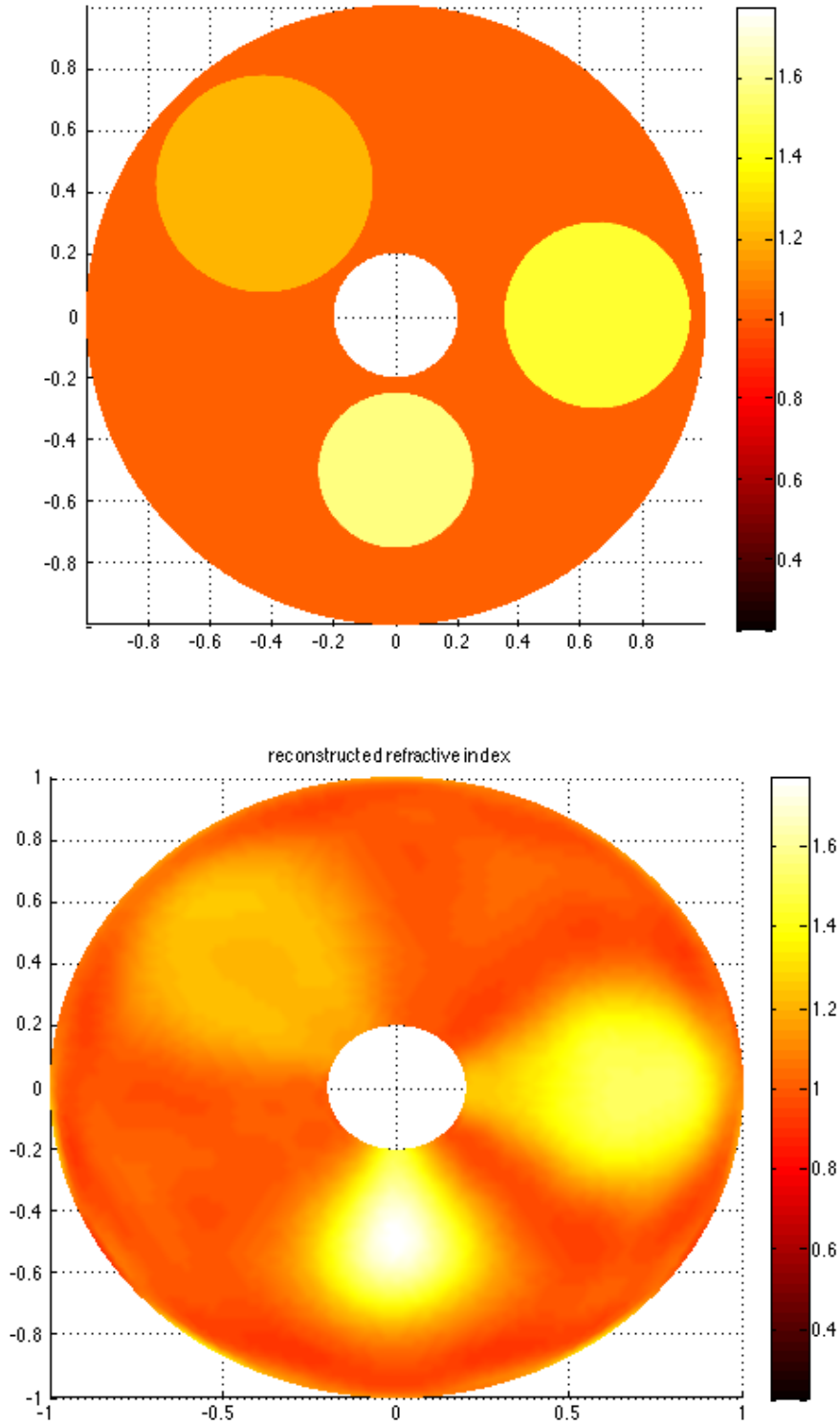


Figure 6.7: Reconstruction of the refractive index  $m(\boldsymbol{x})$  for the three-disks problem ( $k = 2\pi$ ) using degree 10 and 6 incident directions. Relative  $L^2$  error is 17.03%.



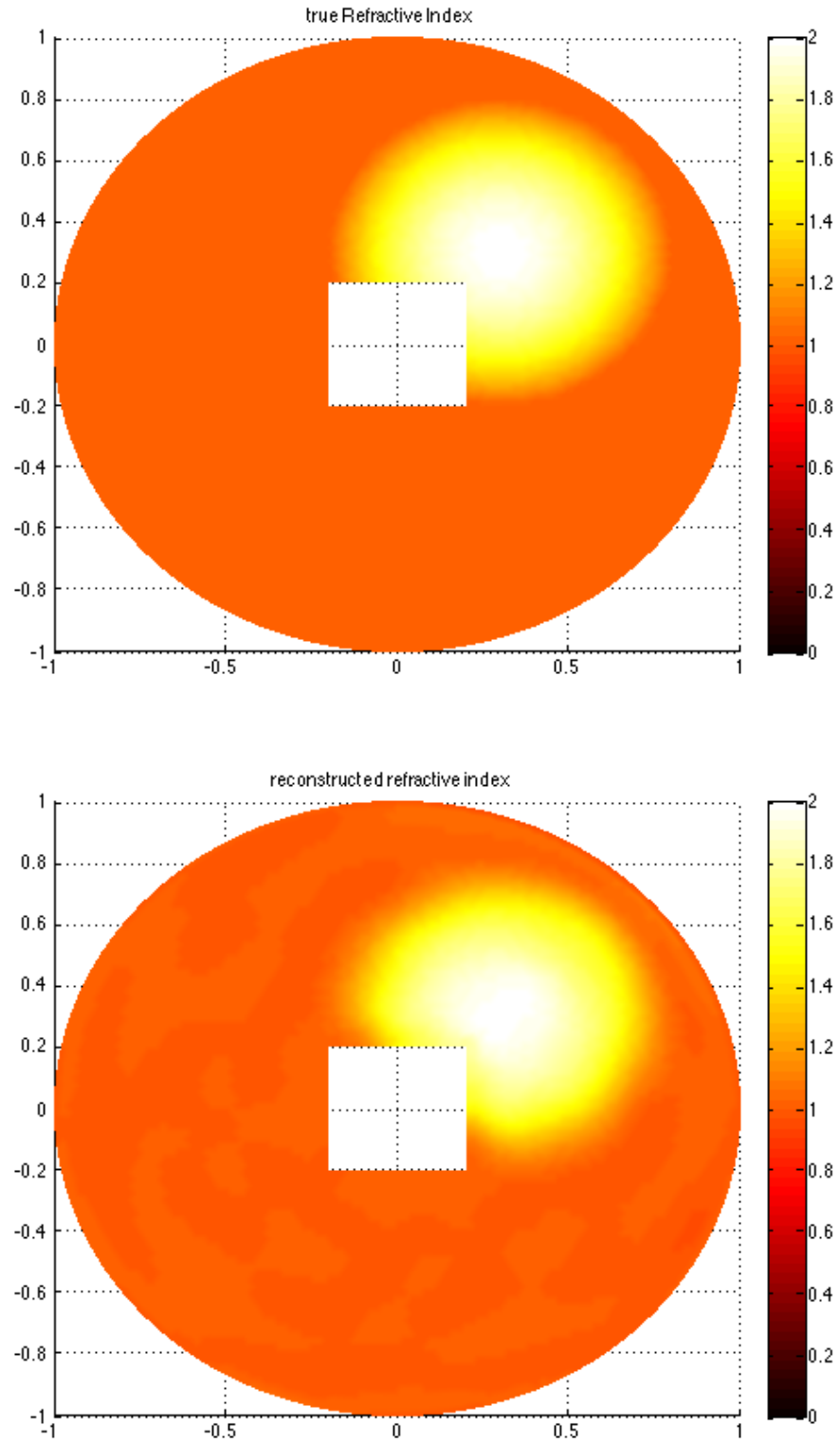


Figure 6.8: Reconstruction of the refractive index  $m(\mathbf{x})$  for the bowl test problem ( $k = \pi$ ) with noise parameter  $\sigma = 1 \times 10^{-3}$  using degree 9 and 4 incident directions. Relative  $L^2$  error is 4.42%.

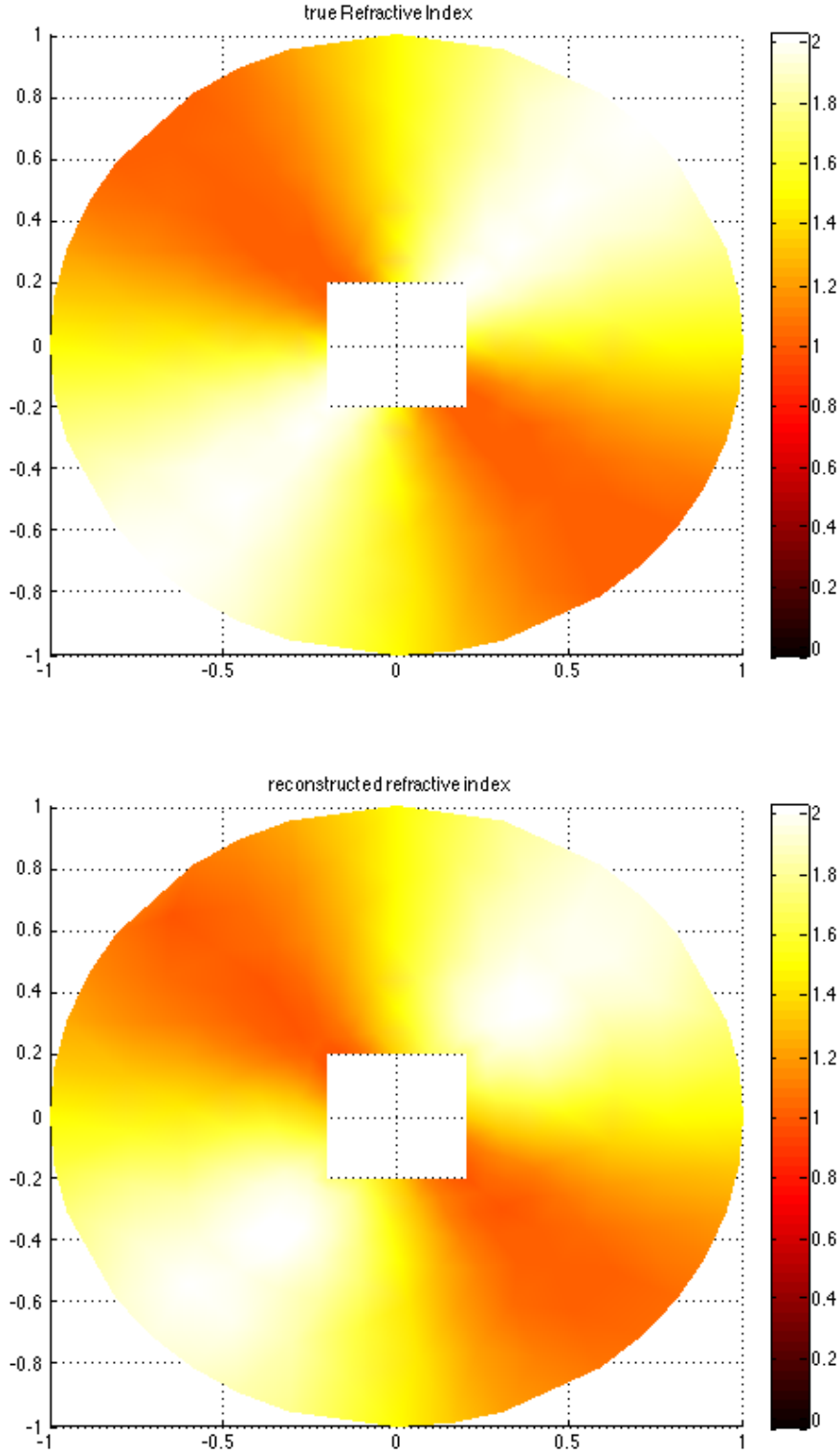


Figure 6.9: Reconstruction of the refractive index  $m(\mathbf{x})$  for the periodic problem ( $k = 2\pi$ ) with noise parameter  $\sigma = 1 \times 10^{-3}$  using degree 7 and 8 incident directions. Relative  $L^2$  error is 6.26%.

degree $N$	d.o.f	bowl (circle)	bowl (square)	three disks
5	66	5.31%	5.80%	16.3%
10	231	1.83%	1.95%	12.5%
15	496	1.00%	1.11%	11.4%
20	861	0.70%	0.76%	9.10%
25	1326	0.51%	0.57%	8.38%
30	1891	0.38%	0.42%	7.36%
35	2556	0.31%	0.35%	6.47%
40	3321	0.26%	0.28%	6.40%
45	4186	0.21%	0.23%	5.61%
50	5151	0.18%	0.20%	5.12%

Table 6.1: Relative  $L^2$  error of the discrete orthogonal projection of the refractive index against number of degrees of freedom (d.o.f.), for each test problem. We exclude the error values for the periodic problem, because in that case the discrete orthogonal projection matches the refractive index almost exactly (the relative  $L^2$  error is already  $2.38e-15$  when  $N = 5$ ).

medium	noise $\sigma$	error	error
		$k = \pi$	$k = 2\pi$
bowl ( $\partial D$ is a circle)	$1 \times 10^{-3}$	7.71%	6.12%
	$1 \times 10^{-2}$	8.54%	5.84%
bowl ( $\partial D$ is a square)	$1 \times 10^{-3}$	4.42%	4.40%
	$1 \times 10^{-2}$	6.13%	5.79%
three disks	0	17.77%	17.03%
periodic	$1 \times 10^{-3}$	7.53%	6.26%

Table 6.2: Relative  $L^2$  error of the reconstructed refractive index  $m(\mathbf{x})$  in  $\Omega$  using Angular Legendre polynomials of degree 7–10.

### 6.3.1 Discussion

We observe that similarly to the figures in Chapter 5, we achieve excellent reconstructions for all test problems, including the new ‘periodic’ test problem in Figure 6.9.

Figures 6.6–6.9 illustrate visually the quality of reconstructions which corresponds to the relative errors of Table 6.2. We observe that a relative  $L^2$  error of less than 10% corresponds to an accurate reconstruction, in that the magnitude and location of the heterogeneities are reconstructed almost precisely. When the relative  $L^2$  error increases to more than 10% (see Figure 6.7), the quality of the reconstruction

becomes noticeably less accurate. Although the positions of the heterogeneities have been recognized, their magnitude is not clearly reconstructed like in Figures 6.6, 6.8 and 6.9.

We note that there are patches having unexpected colours which appear in the reconstructions of Figures 6.6 and 6.8, in the parts of the medium which should be homogeneous. We also observe a similar peculiarity in Figure 6.7. Now because we are approximating the refractive index using a spectral basis, we hypothesize that this is due to a form of Gibbs' phenomenon. We suspect that although higher order modes may achieve a higher overall quality of reconstruction, they will increasingly induce odd irregularities occurring throughout the reconstruction. We observe that such irregularities are not visible in Figure 6.9, which we hypothesize is due to the fact that the orthogonal projection matches the refractive index almost exactly in that case.

In Table 5.2 we notice a significant difference in the error for the 'three disks' problem compared to the other test problems. We speculate that perhaps more iterations are required in Newton's method for the 'three disks' problem in order to obtain the same quality of reconstruction as the other test problems.

Although the quality of reconstructions in Chapters 5 and 6 are roughly the same, the figures from Chapter 6 differ in that they were generated using much higher degrees of freedom in the ansatz. This is because the Angular Legendre functions are not as effective as the Logan-Shepp polynomials in approximating the various refractive index functions, in the sense that much higher degrees of freedom are required to approximate the refractive index function to the same level of accuracy.

Note that an error in the far field of magnitude  $10^{-4}$  corresponds roughly to a relative  $L^2$  error of 1% in the reconstruction. It therefore suffices to select the parameters  $h$  and  $N$  in the forward solver so that the far field error is at most  $10^{-4}$  for the 'bowl' and 'three disks' problems. Refining  $h$  or increasing  $N$  any further will not produce

better reconstructions, because at best the relative error of the reconstruction is that of the projection (which is at least 1.83% from Table 6.1 for  $N = 10$ ). Doing so will unnecessarily make computations more costly.

# Chapter 7

## Discussion

After successfully solving the inverse problems of Chapters 5–6, we understand there are numerous factors which determine the quality of our reconstructions, including:

- The quality of the forward solver.
- The convergence rate of the Levenburg-Marquardt scheme.
- The ability of the ansatz space to accurately approximating the refractive index function.
- The starting solution being sufficiently close to the true solution in the non-linear solver.

None of the above factors are solely sufficient to ensuring our numerical method will work, but they are all necessary conditions. Whether improvements in the above areas would improve the quality of reconstructions is a topic for further research, but we hypothesize in the affirmative. Below we discuss some of the above factors.

---

## Quality of the forward solver

Recall from our discussion in Section 5.3.1 that we were able to drastically improve our results in Chapter 5 from those published in [7]. Both approaches utilized the coupled FEM-BEM technique, but we improved on the method of finite-differences in [7] by computing the Fréchet derivative using its analytic representation. Thus by improving the quality of the forward solver, we were able to improve the quality of reconstructions. For this reason we hypothesize that improving the quality of the forward solver will improve the quality of reconstructions. One possible way of achieving this might be to incorporate a higher order FEM in the forward solver, following [39]. Whether this would improve our numerical method however remains a topic for further research.

## Choice of ansatz space

We hypothesize that improving our choice of ansatz will improve the quality of reconstructions. That is, choosing an ansatz which produces a smaller error in approximating the refractive index function, or approximates the refractive index more accurately with fewer degrees of freedom. There are two pieces of evidence to support this:

1. For both inverse problems, the reconstructions for the ‘three disks’ problems is noticeably poorer compared to the other test problems. Using Tables 5.1 and 6.1, we speculate the reason for this is that the error of the ansatz in approximating the refractive index function for the ‘three disks’ problem is significantly higher than the other test problems. This suggest an ansatz which produces a smaller error in the approximation of the refractive index function might yield better reconstructions.
2. There is a noticeable decline in the quality of reconstructions for ‘three disks’

---

problems from Chapter 5 to Chapter 6. We believe this can be explained by comparing the degrees of freedom listed in Table 6.1 compared to Table 5.1. We notice that the degrees of freedom required to approximate the refractive index function to a certain level of accuracy for that problem are substantially higher in Table 6.1 compared to Table 5.1. This suggests an ansatz which approximates the refractive index more accurately with fewer degrees of freedom might yield better reconstructions.

From the outset, we do not expect to achieve a comparatively high quality reconstruction for the ‘three disks’ problem because we are approximating a discontinuous function using a spectral basis. However, the above points suggest that improving the ansatz could possibly improve the quality of reconstructions for this test problem. This remains a topic for further research.

The test problems in this thesis that have a discontinuous refractive index are very challenging. However we have selected them as test problems due to the availability of independent forward solvers for computing the far field data, that are not based on the coupled FEM-BEM technique.

## Starting solution in the nonlinear solver

When choosing the parameters for the nonlinear solver, the standard choice is to take the starting solution to be  $m(\mathbf{x}) = 1$ . If some data on the solution were available, to provide an initial guess, then we would expect better reconstructions. One way to obtain such data would be to first seek a numerical solution to the inverse problem at a lower wavenumber. In this way, a rough idea of the medium (and hence a better starting solution) can be determined relatively quickly, because the CPU to compute each forward iteration will decrease rather significantly when the wavenumber lowers.

One final point to consider is the number of incident directions used in the nonlinear



---

solver. Currently it is unknown how many incident directions will yield the best reconstruction, and this therefore requires further research.

# Chapter 8

## Conclusion

Kirsch and Monk were the first to formulate the coupled FEM-BEM technique for the forward problem in [60, 61], developing the necessary theory behind the technique. In their numerical results they used a Mie-series formulation to compute the exterior field, and therefore did not present results for the FEM-BEM technique itself. We were therefore the first to implement this technique and to provide full numerical results (the article [39] appeared at the same time).

Next we developed a novel extension of the FEM-BEM technique to solve the inhomogeneous problem. Kirsch and Monk had not considered the inhomogeneous problem, making this particular contribution of the thesis completely original. Not only did we develop the theory necessary to solve the inhomogeneous problem, but we also implemented our novel FEM-BEM scheme successfully and presented a full range of numerical results. Our next contribution [7] to the literature was that we developed a numerical method to solve the inverse medium problem for non-stratified media. Up until [7], the inverse medium problem had been solved with the assumption that the refractive index was radially symmetric [46, 47, 48, 52, 53]. We were the first to solve this inverse problem while forgoing this assumption. Moreover, we were the first to apply the FEM-BEM technique to the inverse problem.

---

In [7] we computed the Fréchet derivative using the method of finite differences. We improved greatly on this approach in this thesis by computing the Fréchet derivative using its analytic expression, which is another one of our contributions to the field. We note that we're also the first to compute the Fréchet derivative using the FEM-BEM technique.

Thus far in the literature, the inverse medium problem has only been considered in the special case where the scatter  $D$  is absent. We were the first to solve the inverse problem in the case where the scatterer  $D$  is present. We expanded on the theory in [23, Chapter 10] and solved this inverse coated problem in full, providing results for various challenging test problems.

We conclude by listing some possible areas for further research, which follow on from the contents of this thesis:

- One possible area for further research would be to incorporate a higher order FEM in our forward solver, following [39]. By incorporating higher degree polynomials in the FEM, we hypothesize that our current  $h^2$  like convergence in the forward scheme could improve to  $h^p$  for  $p \geq 2$  depending on the order of elements. Another advantage is that we would achieve the same level of accuracy in each forward iteration using a smaller FEM stiffness matrix. But we also note that this smaller stiffness matrix will be more numerically expensive to set up. More research is required to determine whether incorporating a higher order FEM will yield better reconstructions of the refractive index.
- Following on from our discussion in Chapter 7, we hypothesize that we can improve the quality of our reconstructions by deriving ansatz spaces which can approximate functions in  $B$  and  $\Omega$  using fewer degrees of freedom. Using fewer degrees of freedom in the nonlinear solver will result in a smaller Jacobian, which in turn will reduce CPU time. It is a topic for further research whether improving the accuracy of the ansatz in this way will improve the accuracy of

---

the inverse solver.

- In this thesis, we consider the illumination of an infinite cylinder in such a way to ensure the scattering problem reduces to 2 dimensions. One natural extension would be to look at the same problem but within a general three dimensional setting. We hypothesize that we can solve the inverse problem for the three dimensional case using a similar approach to the method we used to solve the two dimensional case. The analogue of the two dimensional Nyström scheme discussed in this thesis has already been established in the three dimensional setting [36, 37, 38]. The FEM for three dimensional problems has also been well documented in the literature. In the three dimensional case, we expect that the problem of approximating the refractive index function on the unit disk will be replaced by approximating the refractive index function on the unit sphere. A three-dimensional analogue of the Logan-Shepp polynomials that might be suitable has been done in [4]. Therefore we believe we can extend the techniques of this thesis to readily solve the same problem in a three-dimensional setting.
- Two other possible areas for further research would be to consider scattering by cylindrical or spherical waves, and the case of the heterogeneous coating possessing a complex refractive index  $n(\mathbf{x}) = n_r(\mathbf{x}) + in_i(\mathbf{x})$ , where the imaginary part,  $n_i$ , represents the potential for wave energy absorption by the material. We note that our current algorithm is suitable for both test problems. In particular, we hypothesize that the main adjustment necessary to our algorithm to solve the second problem would be to include the possibility of complex coefficients when expanding the refractive index function using the spectral basis.

# Chapter 9

## Appendix

### 9.1 Neumann Boundary Condition for TE Waves

In this section, we show how a Neumann boundary condition arises in the scattering of TE waves. Following [51, page 130], TE waves arise in the special case where  $\mathbf{c} = (0, 0, 1)$  and  $\psi^a = 0$ . In that case, we have  $\mathbf{E} = -\nabla \times \mathbf{F}$  by (1.64) and therefore the boundary condition  $\mathbf{n} \times \mathbf{E} = \mathbf{0}$  becomes

$$\mathbf{n} \times (\nabla \times \mathbf{F}) = \mathbf{0}, \quad (9.1)$$

where  $\mathbf{n} = (n_1, n_2, 0)$ . Noting  $\mathbf{F} = (0, 0, \psi^f)$ , we get

$$\nabla \times \mathbf{F} = \left( \frac{\partial \psi^f}{\partial y}, -\frac{\partial \psi^f}{\partial x}, 0 \right).$$

It follows from (9.1) that

$$\left( -n_3 \frac{\partial \psi^f}{\partial x}, n_3 \frac{\partial \psi^f}{\partial y}, -n_1 \frac{\partial \psi^f}{\partial x} - n_2 \frac{\partial \psi^f}{\partial y} \right) = \mathbf{0}$$

and therefore

$$n_1 \frac{\partial \psi^f}{\partial x} + n_2 \frac{\partial \psi^f}{\partial y} = 0.$$

This is equivalent to the Neumann boundary condition

$$\mathbf{n} \cdot \nabla \psi^f = \frac{\partial \psi^f}{\partial \mathbf{n}} = 0.$$

## 9.2 The Tikhonov Regularization Theorem

In this section we prove Theorem 2.2.1, following [23]. We begin by stating the following theorem [23, Theorem 4.7]:

**Theorem 9.2.1.** *Let  $\{\mu_n\}$  denote the sequence of non-zero singular values of  $F'_m$  ordered such that*

$$\mu_1 \geq \mu_2 \geq \mu_3 \geq \dots$$

*and repeated according to their multiplicity. Then there exist orthonormal sequences  $\{\mathbf{q}_n\}, \{\mathbf{f}_n\}$  in  $\mathbb{R}^N$  such that*

$$F'_m \mathbf{q}_n = \mu_n \mathbf{f}_n, \quad (F'_m)^T \mathbf{f}_n = \mu_n \mathbf{q}_n$$

*for all  $n \in \mathbb{N}$ . For each  $\mathbf{q}^\delta \in \mathbb{R}^N$ , we have the singular value decomposition*

$$\mathbf{q}^\delta = \sum_{n=1}^{\infty} (\mathbf{q}^\delta \cdot \mathbf{q}_n^\delta) \mathbf{q}_n^\delta + Q \mathbf{q}^\delta,$$

*with the orthogonal projection operator  $Q : \mathbb{R}^N \rightarrow \text{Null}(F'_m)$  and*

$$F'_m \mathbf{q}^\delta = \sum_{n=1}^{\infty} \mu_n (\mathbf{q}^\delta \cdot \mathbf{q}_n^\delta) \mathbf{f}_n.$$

**Remark.** *Each system  $(\mu_n, \mathbf{q}_n^\delta, \mathbf{f}_n)_{n \in \mathbb{N}}$  with the above properties is called a singular system of  $F'_m$ .*

We also have the following result [23, Theorem 4.9]:

**Theorem 9.2.2.** *Suppose  $(\mu_n, \mathbf{q}_n^\delta, \mathbf{f}_n)_{n \in \mathbb{N}}$  is a singular system of  $F'_m : \mathbb{R}^N \rightarrow \mathbb{R}^N$ , and let  $s : (0, \infty) \times (0, \|F'_m\|] \rightarrow \mathbb{R}$  be a bounded function such that for all  $\alpha > 0$  there exists a positive constant  $c(\alpha)$  with*

$$|s(\alpha, \mu)| \leq c(\alpha) \mu, \quad 0 < \mu < \|F'_m\| \quad (9.2)$$

and

$$\lim_{\alpha \rightarrow 0} s(\alpha, \mu) = 1, \quad 0 < \mu < \|F'_m\|. \quad (9.3)$$

Then the bounded linear operators  $R_\alpha : \mathbb{R}^N \rightarrow \mathbb{R}^N$ ,  $\alpha > 0$  defined by

$$R_\alpha \mathbf{f} := \sum_{n=1}^{\infty} \frac{1}{\mu_n} s(\alpha, \mu_n) (\mathbf{f} \cdot \mathbf{f}_n) \mathbf{q}_n^\delta, \quad \mathbf{f} \in \mathbb{R}^N \quad (9.4)$$

describe a regularization scheme.

We are now in a position to prove Theorem 2.2.1. We begin by noting

$$\alpha \|\mathbf{q}^\delta\|^2 \leq (\alpha \mathbf{q}^\delta + (F'_m)^T F'_m \mathbf{q}^\delta) \cdot \mathbf{q}^\delta$$

and therefore deduce the operator  $\alpha I + (F'_m)^T F'_m$  is injective for  $\alpha > 0$ . Now let  $(\mu_n, \mathbf{q}_n^\delta, \mathbf{f}_n)_{n \in \mathbb{N}}$  be a singular system for  $F'_m$ . Then the operator  $T : \mathbb{R}^N \rightarrow \mathbb{R}^N$  defined by

$$T \mathbf{q}^\delta := \sum_{n=1}^{\infty} \frac{1}{\alpha + \mu_n^2} (\mathbf{q}^\delta \cdot \mathbf{q}_n^\delta) \mathbf{q}_n^\delta + \frac{1}{\alpha} Q(\mathbf{q}^\delta) \quad (9.5)$$

is bounded and satisfies

$$(\alpha I + (F'_m)^T F'_m) T = T(\alpha I + (F'_m)^T F'_m) = I.$$

That is,  $T = (\alpha I + (F'_m)^T F'_m)^{-1}$ . Now since  $F'_m$  is injective,

$$\alpha \mathbf{q}^{\alpha, \delta} + (F'_m)^T F'_m \mathbf{q}^{\alpha, \delta} = (F'_m)^T (\mathbf{f}^\delta - F \mathbf{m}^\delta)$$

will have a unique solution  $\mathbf{q}^{\alpha, \delta}$ . We deduce from (9.5) and

$$(F'_m)^T (\mathbf{f}^\delta - F \mathbf{m}^\delta) \cdot \mathbf{q}_n^\delta = \mu_n (\mathbf{f}^\delta - F \mathbf{m}^\delta) \cdot \mathbf{f}_n$$

that

$$\mathbf{q}^{\alpha, \delta} = \sum_{n=1}^{\infty} \frac{\mu_n}{\alpha + \mu_n^2} [(\mathbf{f}^\delta - F \mathbf{m}^\delta) \cdot \mathbf{f}_n] \mathbf{q}_n^\delta.$$



Hence  $R_\alpha$  can be written in the form (9.4) by taking

$$s(\alpha, \mu) = \frac{\mu^2}{\alpha + \mu^2}.$$

This bounded function satisfies (9.2)–(9.3) when  $c(\alpha) = \frac{1}{2\sqrt{\alpha}}$  due to the arithmetic-geometric mean inequality  $\sqrt{\alpha}\mu \leq \frac{\alpha + \mu^2}{2}$ . It therefore follows that  $R_\alpha$  is a regularization strategy.

### 9.3 Finite Element Calculations

This section contains three important results which are needed to compute (3.29), (3.30) and (3.31) respectively.

**Proposition 9.3.1.** *Consider a triangle  $T'$  with vertices  $\mathbf{x}_a = (x_a, y_a)$ ,  $\mathbf{x}_b = (x_b, y_b)$ , and  $\mathbf{x}_c = (x_c, y_c)$ . Then:*

$$\begin{aligned} \iint_{T'} \nabla \phi_a \cdot \nabla \phi_a \, dx dy &= \frac{J}{2K^2} [(y_c - y_b)^2 + (x_b - x_c)^2], \\ \iint_{T'} \nabla \phi_a \cdot \nabla \phi_b \, dx dy &= \frac{J}{2K^2} [(y_c - y_b)(y_a - y_c) + (x_b - x_c)(x_c - x_a)], \end{aligned}$$

where

$$J = |(x_b - x_a)(y_c - y_a) - (x_c - x_a)(y_b - y_a)|, \quad (9.6)$$

$$\text{and } K = (y_b - y_a)(x_c - x_a) - (x_b - x_a)(y_c - y_a). \quad (9.7)$$

*Proof.* Given a triangle  $T'$  on the  $x$ - $y$  plane with vertices  $\mathbf{x}_a, \mathbf{x}_b$  and  $\mathbf{x}_c$ , we map triangle  $T'$  to the reference triangle  $S$  on the  $u$ - $v$  plane, with vertices  $a = (0, 0)$ ,  $b = (1, 0)$  and  $c = (0, 1)$ . The following equations map  $S$  to  $T'$ :

$$x = (x_b - x_a)u + (x_c - x_a)v + x_a, \quad (9.8)$$

$$\text{and } y = (y_b - y_a)u + (y_c - y_a)v + y_a. \quad (9.9)$$

Under this affine transformation, point  $a$  corresponds to  $\mathbf{x}_a$ , point  $b$  corresponds to

$\mathbf{x}_b$ , and point  $c$  corresponds to  $\mathbf{x}_c$ . The Jacobian of this transformation is

$$\begin{aligned} J &= \left| \det \begin{pmatrix} \frac{\partial x}{\partial u} & \frac{\partial x}{\partial v} \\ \frac{\partial y}{\partial u} & \frac{\partial y}{\partial v} \end{pmatrix} \right| \\ &= \left| \det \begin{pmatrix} x_b - x_a & x_c - x_a \\ y_b - y_a & y_c - y_a \end{pmatrix} \right| \\ &= |(x_b - x_a)(y_c - y_a) - (x_c - x_a)(y_b - y_a)|. \end{aligned}$$

Multiplying (9.8) by  $(y_c - y_a)$  and (9.9) by  $(x_c - x_a)$ , we get:

$$x(y_c - y_a) = (x_b - x_a)(y_c - y_a)u + (x_c - x_a)(y_c - y_a)v + x_a(y_c - y_a), \quad (9.10)$$

$$\text{and } y(x_c - x_a) = (y_b - y_a)(x_c - x_a)u + (y_c - y_a)(x_c - x_a)v + y_a(x_c - x_a). \quad (9.11)$$

Subtracting (9.10) from (9.11), we get

$$\begin{aligned} y(x_c - x_a) - x(y_c - y_a) &= u [(y_b - y_a)(x_c - x_a) - (x_b - x_a)(y_c - y_a)] \\ &\quad + [y_a(x_c - x_a) - x_a(y_c - y_a)]. \end{aligned} \quad (9.12)$$

Therefore,  $u = \frac{1}{K} [y(x_c - x_a) - x(y_c - y_a) - y_a(x_c - x_a) + x_a(y_c - y_a)]$  where  $K$  is given by (9.7). It follows that

$$\frac{\partial u}{\partial x} = \frac{y_a - y_c}{K} \quad \text{and} \quad \frac{\partial u}{\partial y} = \frac{x_c - x_a}{K}.$$

Multiplying (9.8) by  $(y_b - y_a)$  and (9.9) by  $(x_b - x_a)$ , we get:

$$x(y_b - y_a) = (x_b - x_a)(y_b - y_a)u + (x_c - x_a)(y_b - y_a)v + x_a(y_b - y_a), \quad (9.13)$$

$$\text{and } y(x_b - x_a) = (y_b - y_a)(x_b - x_a)u + (y_c - y_a)(x_b - x_a)v + y_a(x_b - x_a). \quad (9.14)$$

Subtracting (9.14) from (9.13), we get

$$x(y_b - y_a) - y(x_b - x_a) = Kv + [x_a(y_b - y_a) - y_a(x_b - x_a)]. \quad (9.15)$$

Therefore,  $v = \frac{1}{K} [x(y_b - y_a) - y(x_b - x_a) - x_a(y_b - y_a) + y_a(x_b - x_a)]$ . It follows

$$\frac{\partial v}{\partial x} = \frac{y_b - y_a}{K} \quad \text{and} \quad \frac{\partial v}{\partial y} = \frac{x_a - x_b}{K}.$$

Suppose we define roof functions  $\hat{\phi}_i$  on the  $u$ - $v$  plane for  $i = a, b, c$ . These correspond to our original roof functions on the  $x$ - $y$  plane and they are defined in a similar way: the function  $\hat{\phi}_i$  takes the value of 1 at the point  $i$ , and vanishes at the other two points. More explicitly, we have:

$$\hat{\phi}_a(u, v) = 1 - u - v, \quad (9.16)$$

$$\hat{\phi}_b(u, v) = u, \quad (9.17)$$

$$\text{and } \hat{\phi}_c(u, v) = v. \quad (9.18)$$

We will now evaluate the differential expressions needed to establish our desired integral formulas:

$$\frac{\partial}{\partial x} (\phi_a(x, y)) = \frac{\partial}{\partial u} (\hat{\phi}_a(u, v)) \frac{\partial u}{\partial x} + \frac{\partial}{\partial v} (\hat{\phi}_a(u, v)) \frac{\partial v}{\partial x} = \frac{y_c - y_b}{K},$$

$$\frac{\partial}{\partial y} (\phi_a(x, y)) = \frac{\partial}{\partial u} (\hat{\phi}_a(u, v)) \frac{\partial u}{\partial y} + \frac{\partial}{\partial v} (\hat{\phi}_a(u, v)) \frac{\partial v}{\partial y} = \frac{x_b - x_c}{K}.$$

Applying the same steps as above, the remaining expressions are found:

$$\frac{\partial}{\partial x} (\phi_b(x, y)) = \frac{y_a - y_c}{K}, \quad \frac{\partial}{\partial y} (\phi_b(x, y)) = \frac{x_c - x_a}{K},$$

$$\frac{\partial}{\partial x} (\phi_c(x, y)) = \frac{y_b - y_a}{K}, \quad \frac{\partial}{\partial y} (\phi_c(x, y)) = \frac{x_a - x_b}{K}.$$

Then,

$$\begin{aligned}
 \iint_{T'} \nabla \phi_a \cdot \nabla \phi_a \, dx dy &= \int_0^1 \int_0^{1-u} J \left( \frac{(y_c - y_b)^2}{K^2} + \frac{(x_b - x_c)^2}{K^2} \right) dv du \\
 &= \frac{J}{K^2} [(y_c - y_b)^2 + (x_b - x_c)^2] \int_0^1 \int_0^{1-u} dv du \\
 &= \frac{J}{2K^2} [(y_c - y_b)^2 + (x_b - x_c)^2] . \\
 \iint_{T'} \nabla \phi_a \cdot \nabla \phi_b \, dx dy &= \int_0^1 \int_0^{1-u} J \left( \frac{(y_c - y_b)(y_a - y_c)}{K^2} + \frac{(x_b - x_c)(x_c - x_a)}{K^2} \right) dv du \\
 &= \frac{J}{K^2} [(y_c - y_b)(y_a - y_c) + (x_b - x_c)(x_c - x_a)] \int_0^1 \int_0^{1-u} dv du \\
 &= \frac{J}{2K^2} [(y_c - y_b)(y_a - y_c) + (x_b - x_c)(x_c - x_a)] .
 \end{aligned}$$

□

Using the above result we can assemble the matrix  $B$  defined by (3.29). We assemble the matrix  $C$  defined by (3.30) by applying the following result:

**Proposition 9.3.2.** *Consider the triangle  $T'$  from the previous proposition. Then:*

$$\begin{aligned}
 \iint_{T'} \phi_a(x, y) \phi_a(x, y) \, dx dy &= \frac{J}{12}, \\
 \iint_{T'} \phi_a(x, y) \phi_b(x, y) \, dx dy &= \frac{J}{24}.
 \end{aligned}$$

The proof is similar to the previous proof; we exclude it here for the sake of brevity.

To assemble the matrix defined by (3.31), we apply the following.

**Proposition 9.3.3.** *Consider the line  $l$  joining  $\mathbf{x}_r = (r_1, r_2)$  and  $\mathbf{x}_s = (s_1, s_2)$ .*

Then

$$\int_l \phi_r(x, y) \phi_s(x, y) = \frac{1}{6} \sqrt{(r_1 - s_1)^2 + (r_2 - s_2)^2} \quad (9.19)$$

$$\int_l \phi_r(x, y) \phi_r(x, y) = \frac{1}{3} \sqrt{(r_1 - s_1)^2 + (r_2 - s_2)^2} \quad (9.20)$$

*Proof.* Using the parametrization

$$\mathbf{g} : [0, 1] \rightarrow l; \quad t \rightarrow [r_1 t + (1 - t)s_1, r_2 t + (1 - t)s_2],$$

we have  $\phi_r(x, y) = t$  and  $\phi_s(x, y) = 1 - t$ . Therefore

$$\begin{aligned} \int_l \phi_r(x, y) \phi_s(x, y) &= \int_0^1 t(1 - t) \sqrt{(r_1 - s_1)^2 + (r_2 - s_2)^2} dt \\ &= \sqrt{(r_1 - s_1)^2 + (r_2 - s_2)^2} \int_0^1 t - t^2 dt \\ &= \frac{1}{6} \sqrt{(r_1 - s_1)^2 + (r_2 - s_2)^2}. \end{aligned}$$

Similarly,

$$\begin{aligned} \int_l \phi_r(x, y) \phi_r(x, y) &= \int_0^1 t^2 \sqrt{(r_1 - s_1)^2 + (r_2 - s_2)^2} dt \\ &= \frac{1}{3} \sqrt{(r_1 - s_1)^2 + (r_2 - s_2)^2}. \end{aligned}$$

□

## 9.4 Derivation of the Integral Representation of the Far Field

In this section we derive the far field integral representation given in (3.36). We begin by stating the following definition.

**Definition 9.4.1.** *Every radiating solution to the two-dimensional Helmholtz equation has the asymptotic behaviour of an outgoing spherical wave*

$$u(\mathbf{x}) = \frac{e^{ik|\mathbf{x}|}}{\sqrt{|\mathbf{x}|}} \left\{ u_\infty(\hat{\mathbf{x}}) + \mathcal{O}\left(\frac{1}{|\mathbf{x}|}\right) \right\}, \quad \mathbf{x} \rightarrow \infty, \quad (9.21)$$

uniformly in all directions  $\hat{\mathbf{x}} = \frac{\mathbf{x}}{|\mathbf{x}|}$ . The far field of  $u$  is then defined to be  $u_\infty$ .

We now prove the following result.

**Proposition 9.4.2.** *The far field in the two-dimensional case has the integral representation*

$$u_\infty(\hat{\mathbf{x}}) = \frac{e^{\frac{\pi i}{4}}}{\sqrt{8\pi k}} \int_{\partial\Omega} \left\{ \frac{\partial e^{-ik\hat{\mathbf{x}} \cdot \mathbf{y}}}{\partial \mathbf{n}(\mathbf{y})} u^s(\mathbf{y}) + ik e^{-ik\hat{\mathbf{x}} \cdot \mathbf{y}} u^s(\mathbf{y}) - e^{-ik\hat{\mathbf{x}} \cdot \mathbf{y}} \mu(\mathbf{y}) \right\} ds(\mathbf{y}). \quad (9.22)$$

*Proof.* Noting

$$|\mathbf{x} - \mathbf{y}| = \sqrt{|\mathbf{x}|^2 - 2\mathbf{x} \cdot \mathbf{y} + |\mathbf{y}|^2} \quad (9.23)$$

$$= |\mathbf{x}| - \hat{\mathbf{x}} \cdot \mathbf{y} + \mathcal{O}\left(\frac{1}{|\mathbf{x}|}\right), \quad \hat{\mathbf{x}} = \frac{\mathbf{x}}{|\mathbf{x}|}, \quad (9.24)$$

we get

$$e^{ik|\mathbf{x} - \mathbf{y}|} = e^{ik|\mathbf{x}|} \left\{ e^{-ik\hat{\mathbf{x}} \cdot \mathbf{y}} + \mathcal{O}\left(\frac{1}{|\mathbf{x}|}\right) \right\}. \quad (9.25)$$

Now because the Hankel function of the first kind,  $H_0^{(1)}$ , has asymptotic behaviour [23]

$$H_0^{(1)}(t) = \sqrt{\frac{2}{\pi t}} e^{i(t - \frac{\pi}{4})} \left\{ 1 + \mathcal{O}\left(\frac{1}{t}\right) \right\}, \quad t \rightarrow \infty, \quad (9.26)$$

we deduce

$$\begin{aligned} H_0^{(1)}(k|\mathbf{x} - \mathbf{y}|) &= e^{-\frac{\pi i}{4}} \sqrt{\frac{2}{\pi k|\mathbf{x}|}} e^{ik|\mathbf{x}|} \left\{ e^{-ik\hat{\mathbf{x}} \cdot \mathbf{y}} + \mathcal{O}\left(\frac{1}{|\mathbf{x}|}\right) \right\} \\ &= e^{-\frac{\pi i}{4}} \sqrt{\frac{2}{\pi k}} \frac{e^{ik|\mathbf{x}|}}{\sqrt{|\mathbf{x}|}} \left\{ e^{-ik\hat{\mathbf{x}} \cdot \mathbf{y}} + \mathcal{O}\left(\frac{1}{|\mathbf{x}|}\right) \right\} \end{aligned}$$

using (9.25). It follows that the fundamental solution of the 2D Helmholtz equation

$$\Phi(\mathbf{x}, \mathbf{y}) = \frac{i}{4} H_0^{(1)}(k|\mathbf{x} - \mathbf{y}|)$$

satisfies

$$\Phi(\mathbf{x}, \mathbf{y}) = \frac{i}{4} \cdot e^{-\frac{\pi i}{4}} \sqrt{\frac{2}{\pi k}} \frac{e^{ik|\mathbf{x}|}}{\sqrt{|\mathbf{x}|}} \left\{ e^{-ik\hat{\mathbf{x}} \cdot \mathbf{y}} + \mathcal{O}\left(\frac{1}{|\mathbf{x}|}\right) \right\}.$$

That is,

$$\Phi(\mathbf{x}, \mathbf{y}) = e^{\frac{\pi i}{4}} \sqrt{\frac{1}{8\pi k}} \frac{e^{ik|\mathbf{x}|}}{\sqrt{|\mathbf{x}|}} \left\{ e^{-ik\hat{\mathbf{x}} \cdot \mathbf{y}} + \mathcal{O}\left(\frac{1}{|\mathbf{x}|}\right) \right\}, \quad (9.27)$$

and hence

$$\frac{\partial \Phi(\mathbf{x}, \mathbf{y})}{\partial \mathbf{n}(\mathbf{y})} = e^{\frac{\pi i}{4}} \sqrt{\frac{1}{8\pi k}} \frac{e^{ik|\mathbf{x}|}}{\sqrt{|\mathbf{x}|}} \left\{ \frac{\partial e^{-ik\hat{\mathbf{x}} \cdot \mathbf{y}}}{\partial \mathbf{n}(\mathbf{y})} + \mathcal{O}\left(\frac{1}{|\mathbf{x}|}\right) \right\}. \quad (9.28)$$

Substituting (9.27)–(9.28) into Green's formula

$$u^s(\mathbf{x}) = \int_{\partial\Omega} \left\{ \frac{\partial \Phi(\mathbf{x}, \mathbf{y})}{\partial \mathbf{n}(\mathbf{y})} u^s(\mathbf{y}) - \frac{\partial u^s}{\partial \mathbf{n}(\mathbf{y})} \Phi(\mathbf{x}, \mathbf{y}) \right\} ds(\mathbf{y}),$$

yields

$$u_\infty(\hat{\mathbf{x}}) = \frac{e^{\frac{\pi}{4}}}{\sqrt{8\pi k}} \int_{\partial\Omega} \left\{ \frac{\partial e^{-ik\hat{\mathbf{x}} \cdot \mathbf{y}}}{\partial \mathbf{n}(\mathbf{y})} u^s(\mathbf{y}) - \frac{\partial u^s}{\partial \mathbf{n}(\mathbf{y})} e^{-ik\hat{\mathbf{x}} \cdot \mathbf{y}} \right\} ds(\mathbf{y}). \quad (9.29)$$

Recall from Chapter 3 that  $\frac{\partial u^s}{\partial \mathbf{n}} + ik u^s = \mu$  and therefore  $\frac{\partial u^s}{\partial \mathbf{n}} = \mu - ik u^s$ . Substituting



this into the above equation yields (9.22).

□

## 9.5 Radiating Wave Functions

In this section, we prove the following lemma from Chapter 4 regarding the radiating wave functions:

**Lemma 9.5.1.** *The radiating wave functions*

$$e_m(r, \theta) = H_{|m|}^{(1)}(kr)e^{im\theta}$$

*satisfy the homogeneous Helmholtz equation*

$$\Delta u(\mathbf{x}) + k^2 u(\mathbf{x}) = 0, \quad \mathbf{x} \in \mathbb{R}^2 \setminus \bar{D},$$

*and the Sommerfeld radiation condition. The far field of  $e_m$  is given by*

$$e_m^\infty(\theta) = \sqrt{\frac{1}{\pi k}} (-1)^m (1 - i) e^{im\theta}.$$

*Proof.* From [23], the Hankel functions of the first kind have asymptotic behaviour

$$H_{|m|}^{(1)}(t) = \sqrt{\frac{2}{\pi t}} e^{i(t - \frac{|m|\pi}{2} - \frac{\pi}{4})} \left\{ 1 + \mathcal{O}\left(\frac{1}{t}\right) \right\}, \quad t \rightarrow \infty, \quad (9.30)$$

$$H_{|m|}^{(1)'}(t) = \sqrt{\frac{2}{\pi t}} e^{i(t - \frac{|m|\pi}{2} + \frac{\pi}{4})} \left\{ 1 + \mathcal{O}\left(\frac{1}{t}\right) \right\}, \quad t \rightarrow \infty. \quad (9.31)$$

It is then obvious from (9.30)–(9.31) that the radiating wave functions satisfy the Sommerfeld radiation condition.

To see why they satisfy the homogeneous Helmholtz equation, first note that the Laplacian operator in polar coordinates is given by

$$\Delta u(r, \theta) = \frac{1}{r} \frac{\partial u}{\partial r} + \frac{\partial^2 u}{\partial r^2} + \frac{1}{r^2} \frac{\partial^2 u}{\partial \theta^2}.$$

It follows that

$$\begin{aligned}
 \Delta e_m + k^2 e_m &= \frac{k}{r} H_{|m|}^{(1)'}(kr) e^{im\theta} + k^2 H_{|m|}^{(1)''}(kr) e^{im\theta} - \frac{m^2}{r^2} H_{|m|}^{(1)}(kr) e^{im\theta} + k^2 H_{|m|}^{(1)}(kr) e^{im\theta} \\
 &= k^2 H_{|m|}^{(1)''}(kr) e^{im\theta} + \frac{k}{r} H_{|m|}^{(1)'}(kr) e^{im\theta} + H_{|m|}^{(1)}(kr) e^{im\theta} \left[ k^2 - \frac{m^2}{r^2} \right] \\
 &= \frac{e^{im\theta}}{r^2} \left( k^2 r^2 H_{|m|}^{(1)''}(kr) e^{im\theta} + kr H_{|m|}^{(1)'}(kr) e^{im\theta} + H_{|m|}^{(1)}(kr) e^{im\theta} [k^2 r^2 - m^2] \right) \\
 &= 0,
 \end{aligned}$$

because  $H_{|m|}^{(1)}(kr)$  is a fundamental solution of Bessel's equation of order  $m$ . That is,

$$k^2 r^2 H_{|m|}^{(1)''}(kr) e^{im\theta} + kr H_{|m|}^{(1)'}(kr) e^{im\theta} + H_{|m|}^{(1)}(kr) e^{im\theta} [k^2 r^2 - m^2] = 0.$$

Now the far field  $e_m^\infty(\theta)$  is obtained by taking the limit of  $e_m(r, \theta)$  as  $r \rightarrow \infty$  (for this reason, the expression for  $e_m^\infty(\theta)$  is independent of  $r$ ). From (9.30), we have

$$\begin{aligned}
 H_{|m|}^{(1)}(k|\mathbf{x}|) &= \sqrt{\frac{2}{\pi k|\mathbf{x}|}} e^{i(k|\mathbf{x}| - \frac{|m|\pi}{2} - \frac{\pi}{4})} \left\{ 1 + \mathcal{O}\left(\frac{1}{t}\right) \right\} \\
 &= \sqrt{\frac{1}{\pi k}} (-1)^m (1 - i) \frac{e^{ik|\mathbf{x}|}}{\sqrt{|\mathbf{x}|}} \left\{ 1 + \mathcal{O}\left(\frac{1}{t}\right) \right\}
 \end{aligned}$$

since  $\sqrt{2}e^{-\frac{\pi}{4}i} = 1 - i$  and  $e^{\frac{-i|m|\pi}{2}} = (-1)^m$ . It therefore follows

$$H_{|m|}^{(1)}(kr) e^{im\theta} = \sqrt{\frac{1}{\pi k}} (-1)^m (1 - i) e^{im\theta} \frac{e^{ik|\mathbf{x}|}}{\sqrt{|\mathbf{x}|}} \left\{ 1 + \mathcal{O}\left(\frac{1}{t}\right) \right\}$$

and therefore the far field of  $e_m(r, \theta)$  is given by

$$e_m^\infty(\theta) = \sqrt{\frac{1}{\pi k}} (-1)^m (1 - i) e^{im\theta}.$$

□

## 9.6 Orthogonal Polynomials

In this section, we first briefly discuss some properties of Chebyshev polynomials, and then prove that the Logan-Shepp polynomials are orthogonal over the unit disk.

### 9.6.1 Chebyshev polynomials

Chebyshev polynomials of the second kind  $\{U_n\}_{n \in \mathbb{N}_0}$  are fundamental solutions of the Chebyshev differential equation of the second kind,

$$(1 - x^2) \frac{dy}{dx} - 3x \frac{dy}{dx} + n(n+2)y = 0.$$

They are defined by the following recurrence relation:

$$U_0(x) = 1,$$

$$U_1(x) = 2x,$$

$$U_n(x) = 2xU_{n-1}(x) - U_{n-2}(x).$$

This recurrence relation combined with the identity [33, Section 1.4.3]

$$\frac{\sin(n+2)\theta}{\sin \theta} = 2 \cos \theta \frac{\sin(n+1)\theta}{\sin \theta} - \frac{\sin n\theta}{\sin \theta} \quad (n \geq 0)$$

implies

$$U_n(\cos \theta) = \frac{\sin(n+1)\theta}{\sin \theta}.$$

The Chebyshev polynomials of the second kind are orthogonal on the interval  $[-1, 1]$  with respect to the weight function  $\sqrt{1-x^2}$ :

$$\frac{2}{\pi} \int_{-1}^1 U_n(x) U_m(x) \sqrt{1-x^2} dx = \delta_{n,m}.$$

### 9.6.2 Logan-Shepp polynomials

In this section, we prove the Logan-Shepp polynomials

$$P_{l,j} = \frac{1}{\sqrt{\pi}} U_j \left( x_1 \cos \frac{l\pi}{j+1} + x_2 \sin \frac{l\pi}{j+1} \right)$$

are orthogonal over the unit disk, following [33]. We begin by defining a couple of polynomial spaces. Let

$$\Pi_j^2 := \text{span}\{x_1^{j_1} x_2^{j_2} : j_1 + j_2 \leq j, j_1, j_2 \in \mathbb{N}_0\}$$

denote the space of polynomials in two variables of total degree  $j$ . We then define

$$\mathcal{V}_j^2 := \text{span}\{p \in \Pi_j^2 : \iint_B p(\mathbf{x})q(\mathbf{x}) d\mathbf{x} = 0, \text{ for all } q \in \Pi_{j-1}^2\}$$

to be the space of all polynomials of degree  $j$  orthogonal to polynomials of lower degree. To prove the orthogonality of the Logan-Shepp polynomials, we first establish  $P_{l,j} \in \mathcal{V}_j^2$ .

To do so, note one of the features of Chebyshev polynomials are their relation to the Radon transform. Let  $\mathcal{L}(\theta, t) = \{(x_1, x_2) : x_1 \cos \theta + x_2 \sin \theta = t\}$  for  $-1 \leq t \leq 1$  and  $I(\theta, t) = \mathcal{L}(\theta, t) \cap B$ . Then the Radon projection  $\mathcal{R}_\theta(f; t)$  of a function  $f$  in the direction  $\theta$  with parameter  $t \in [-1, 1]$  is defined by

$$\mathcal{R}_\theta(f; t) := \int_{I(\theta, t)} f(\mathbf{x}) d\mathcal{L} \tag{9.32}$$

$$= \int_{-\sqrt{1-t^2}}^{\sqrt{1-t^2}} f(t \cos \theta - s \sin \theta, t \sin \theta + s \cos \theta) ds, \tag{9.33}$$

where  $d\mathcal{L}$  denotes the Lebesgue measure on  $I(\theta, t)$ .

Now for  $\theta \in [0, \pi]$  and  $g : \mathbb{R} \rightarrow \mathbb{R}$ , we define  $g_\theta(x_1, x_2) := g(x_1 \cos \theta + x_2 \sin \theta)$ .

Applying the change of variables  $t = x_1 \cos \phi + x_2 \sin \phi$  and  $s = -x_1 \sin \phi + x_2 \cos \phi$

produces a rotation and implies

$$\frac{1}{\pi} \iint_B f(\mathbf{x}) g_\theta(\mathbf{x}) \, d\mathbf{x} = \frac{1}{\pi} \int_{-1}^1 \mathcal{R}_\theta(f; t) g(t) \, dt. \quad (9.34)$$

Applying a second change of variable in (9.33) gives

$$\mathcal{R}_\theta(f; t) = \sqrt{1-t^2} \int_{-1}^1 f(t \cos \theta - s \sqrt{1-t^2} \sin \theta, t \sin \theta + s \sqrt{1-t^2} \cos \theta) \, ds.$$

Note that if  $f$  is a polynomial of degree  $n$ , then the integrand above will also be a polynomial of the same degree in  $t$ . It follows  $Q(t) := \frac{\mathcal{R}_\theta(f; t)}{\sqrt{1-t^2}}$  is a polynomial of degree  $n$  for all  $\theta$ . Moreover, we must have  $Q(1) = 2f(\cos \theta, \sin \theta)$ . It therefore follows from (9.34) that

$$\iint_B f(\mathbf{x}) P_{l,j}(\mathbf{x}) \, d\mathbf{x} = 0$$

for all  $f \in \Pi_n^2$  whenever  $n < j$ , due to the orthogonality of the Chebyshev polynomials. Now that we have established  $P_{l,j} \in \mathcal{V}_j^2$ , we can prove the orthogonality of the Logan-Shepp polynomials.

Note that (9.34) implies

$$\int_{-1}^1 \frac{\mathcal{R}_\theta(P_{l,j}; t)}{\sqrt{1-t^2}} U_n(t) \sqrt{1-t^2} \, dt = \iint_B P_{l,j}(\mathbf{x}) (U_n)_\theta(\mathbf{x}) \, d\mathbf{x} = 0, \quad n = 0, 1, \dots, j-1,$$

because  $P_{l,j} \in \mathcal{V}_j^2$ . It follows that the polynomial  $Q(t) = \frac{\mathcal{R}_\theta(P_{l,j}; t)}{\sqrt{1-t^2}}$  is orthogonal to  $U_n$  for  $0 \leq n \leq j-1$  and is therefore a multiple of  $U_j$ , as it is a polynomial of degree  $j$  i.e.  $Q(t) = cU_j(t)$  for some constant  $c$ . Taking  $t = 1$  and noting  $U_j(1) = j+1$ , we get

$$c = \frac{P_{l,j}(\cos \theta, \sin \theta)}{j+1} = \frac{2U_j(\cos[\theta - \frac{l\pi}{j+1}])}{j+1}.$$

Using the fact that

$$U_j \left( \cos \frac{(n-l)\pi}{j+1} \right) = \frac{\sin(n-l)\pi}{\sin \frac{(n-l)\pi}{j+1}} = 0$$

when  $n \neq l$ , we therefore conclude that

$$\begin{aligned}
 \iint_B P_{n,j}(\mathbf{x}) P_{l,j}(\mathbf{x}) \, d\mathbf{x} &= \frac{1}{\pi} \iint_B P_{l,j}(\mathbf{x}) (U_j)_\theta(\mathbf{x}) \, d\mathbf{x} \quad \text{where } \theta = \frac{n\pi}{j+1} \\
 &= \frac{1}{\pi} \int_{-1}^1 \mathcal{R}_\theta(P_{l,j}; t) U_j(t) \, dt \quad \text{using (9.34)} \\
 &= \frac{2}{\pi^2} \frac{U_j\left(\cos \frac{(n-l)\pi}{j+1}\right)}{j+1} \int_{-1}^1 [U_j(t)]^2 \sqrt{1-t^2} \, dt \\
 &= \delta_{l,n}
 \end{aligned}$$

since  $\mathcal{R}_\theta(p_{l,j}; t) = c\sqrt{1-t^2}U_j(t)$ .

## 9.7 Gaussian Quadrature

To approximate the integral (6.3), apply a  $Q$ -point Gaussian quadrature rule for the radial integral and a  $2Q$ -point rectangular quadrature rule for the angular integral:

$$a_{s,t} \approx \frac{2s+1}{4\pi} \sum_{j=0}^{2Q-1} \sum_{i=1}^Q \omega_i L_s e^{it\theta_j}(S_i), \quad (9.35)$$

where  $\theta_j = \frac{\pi j}{Q+1}$ ,  $S_i$  is the  $i$ th root of the  $Q$ th order Legendre polynomial, and

$$\omega_i = \frac{2\pi}{(Q+1)(1-S_i)^2(L'_Q(S_i))^2}$$

represents the quadrature weighting, where

$$L'_Q(S_i) = \frac{Q}{S_i^2 - 1} (S_i L_Q(S_i) - L_{Q-1}(S_i)).$$



## 9.8 Green's Theorems

### 9.8.1 Green's Identities

Consider a Lipschitz domain  $X$  with boundary  $\partial X$ , and let  $\mathbf{n}$  be the outward pointing unit normal on  $\partial X$ .

**Theorem 9.8.1** (Green's First Identity). *If  $v \in H^1(X)$  and  $w \in H^2(X)$ , then*

$$\iint_X v(\mathbf{x}) \Delta w(\mathbf{x}) \, d\mathbf{x} + \iint_X \nabla v(\mathbf{x}) \cdot \nabla w(\mathbf{x}) \, d\mathbf{x} = - \int_{\partial X} v(\mathbf{x}) \frac{\partial w}{\partial \mathbf{n}}(\mathbf{x}) \, ds(\mathbf{x}).$$

**Theorem 9.8.2** (Green's Second Identity). *If  $v, w \in H^1(X)$ , then*

$$\iint_X v(\mathbf{x}) \Delta w(\mathbf{x}) - w(\mathbf{x}) \Delta v(\mathbf{x}) \, d\mathbf{x} = \int_{\partial X} v(\mathbf{x}) \frac{\partial w}{\partial \mathbf{n}}(\mathbf{x}) - w(\mathbf{x}) \frac{\partial v}{\partial \mathbf{n}}(\mathbf{x}) \, ds(\mathbf{x}).$$

### 9.8.2 Green's Representation Formula

Using the above identities, we now derive Green's representation formula.

**Theorem 9.8.3.** *For  $u \in H^2(\Omega)$  and  $\mathbf{x} \in \Omega$ , we have*

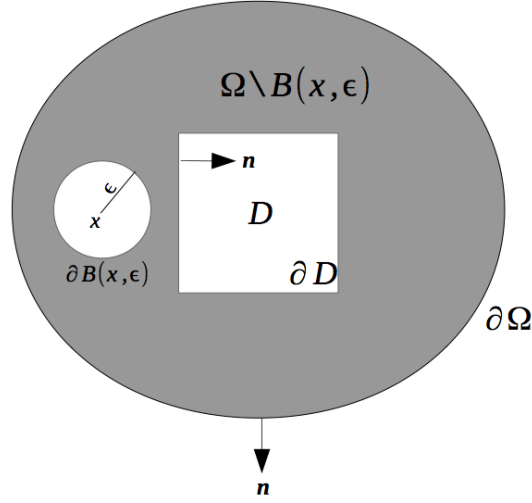
$$u(\mathbf{x}) = \int_{\partial D \cup \partial \Omega} \left\{ \frac{\partial u}{\partial \mathbf{n}}(\mathbf{y}) \Phi(\mathbf{x}, \mathbf{y}) - u(\mathbf{y}) \frac{\partial \Phi}{\partial \mathbf{n}}(\mathbf{y}) \right\} \, ds(\mathbf{y}) - \iint_{\Omega} \{ \Delta u(\mathbf{y}) + k^2 u(\mathbf{y}) \} \Phi(\mathbf{x}, \mathbf{y}) \, d\mathbf{y}.$$

*Proof.* Suppose  $x \in \Omega$  is an arbitrary point, and consider the circle

$$\partial B(\mathbf{x}, \epsilon) := \{ \mathbf{y} \in \mathbb{R}^2 : \|\mathbf{y} - \mathbf{x}\| = \epsilon \},$$

where  $\epsilon$  is chosen to be small enough to ensure  $B(\mathbf{x}, \epsilon) \subset \Omega$ .

Now because  $\Omega \setminus B(\mathbf{x}, \epsilon)$  is a Lipschitz domain, it follows from Green's second identity

Figure 9.1: Visualization of the region  $\Omega \setminus B(\mathbf{x}, \epsilon)$ .

that

$$\int_{\Gamma_\epsilon} \Phi(\mathbf{x}, \mathbf{y}) \frac{\partial u}{\partial \mathbf{n}}(\mathbf{y}) - u(\mathbf{y}) \frac{\partial \Phi}{\partial \mathbf{n}}(\mathbf{y}) ds(\mathbf{y}) = \iint_{\Omega \setminus B(\mathbf{x}, \epsilon)} \Phi(\mathbf{x}, \mathbf{y}) \Delta u(\mathbf{y}) - u(\mathbf{y}) \Delta_{\mathbf{y}} \Phi(\mathbf{x}, \mathbf{y}) d\mathbf{y}$$

for  $u, \Phi \in H^1(\Omega)$ , where  $\Gamma_\epsilon := \partial\Omega \cup \partial D \cup \partial B(\mathbf{x}, \epsilon)$  is the boundary of  $\Omega \setminus B(\mathbf{x}, \epsilon)$ .

Taking  $\Phi(\mathbf{x}, \mathbf{y}) = \frac{i}{4} H_0^{(1)}(k\|\mathbf{x} - \mathbf{y}\|)$ , the above equation simplifies to

$$\int_{\Gamma_\epsilon} \frac{\partial u}{\partial \mathbf{n}}(\mathbf{y}) \Phi(\mathbf{x}, \mathbf{y}) - u(\mathbf{y}) \frac{\partial \Phi}{\partial \mathbf{n}}(\mathbf{y}) ds(\mathbf{y}) = \iint_{\Omega \setminus B(\mathbf{x}, \epsilon)} \{\Delta u(\mathbf{y}) + k^2 u(\mathbf{y})\} \Phi(\mathbf{x}, \mathbf{y}) d\mathbf{y},$$

since  $\Phi(\mathbf{x}, \mathbf{y})$  is the fundamental solution to the Helmholtz equation in  $\mathbb{R}^2$ . It therefore follows that

$$\begin{aligned} \int_{\partial D \cup \partial\Omega} \frac{\partial u}{\partial \mathbf{n}}(\mathbf{y}) \Phi(\mathbf{x}, \mathbf{y}) - u(\mathbf{y}) \frac{\partial \Phi}{\partial \mathbf{n}}(\mathbf{y}) ds(\mathbf{y}) &= \iint_{\Omega \setminus B(\mathbf{x}, \epsilon)} \{\Delta u(\mathbf{y}) + k^2 u(\mathbf{y})\} \Phi(\mathbf{x}, \mathbf{y}) d\mathbf{y} \\ &\quad - \int_{\partial B(\mathbf{x}, \epsilon)} \frac{\partial u}{\partial \mathbf{n}}(\mathbf{y}) \Phi(\mathbf{x}, \mathbf{y}) - u(\mathbf{y}) \frac{\partial \Phi}{\partial \mathbf{n}}(\mathbf{y}) ds(\mathbf{y}). \end{aligned}$$

Taking the limit of both sides as  $\epsilon \rightarrow 0$ , we get

$$\begin{aligned} \int_{\partial D \cup \partial\Omega} \frac{\partial u}{\partial \mathbf{n}}(\mathbf{y}) \Phi(\mathbf{x}, \mathbf{y}) - u(\mathbf{y}) \frac{\partial \Phi}{\partial \mathbf{n}}(\mathbf{y}) ds(\mathbf{y}) &= \iint_{\Omega} \{\Delta u(\mathbf{y}) + k^2 u(\mathbf{y})\} \Phi(\mathbf{x}, \mathbf{y}) d\mathbf{y} \\ &\quad - \lim_{\epsilon \rightarrow 0} (I_1 - I_2), \end{aligned}$$

where

$$I_1 = \int_{\partial B(\mathbf{x}, \epsilon)} \frac{\partial u}{\partial \mathbf{n}}(\mathbf{y}) \Phi(\mathbf{x}, \mathbf{y}) \, ds(\mathbf{y}) \quad \text{and} \quad I_2 = \int_{\partial B(\mathbf{x}, \epsilon)} u(\mathbf{y}) \frac{\partial \Phi}{\partial \mathbf{n}}(\mathbf{y}) \, ds(\mathbf{y}).$$

To find the limit of  $I_1$ , first note that

$$\begin{aligned} \left| \int_{\partial B(\mathbf{x}, \epsilon)} \frac{\partial u}{\partial \mathbf{n}}(\mathbf{y}) \Phi(\mathbf{x}, \mathbf{y}) \, ds(\mathbf{y}) \right| &\leq \int_{\partial B(\mathbf{x}, \epsilon)} \left| \frac{\partial u}{\partial \mathbf{n}}(\mathbf{y}) \Phi(\mathbf{x}, \mathbf{y}) \right| \, ds(\mathbf{y}) \\ &= \left| \frac{i}{4} H_0^{(1)}(k\epsilon) \right| \int_{\partial B(\mathbf{x}, \epsilon)} \left| \frac{\partial u}{\partial \mathbf{n}}(\mathbf{y}) \right| \, ds(\mathbf{y}) \\ &\leq \frac{\pi\epsilon}{2} \left| H_0^{(1)}(k\epsilon) \right| \sup_{\mathbf{y} \in \partial B(\mathbf{x}, \epsilon)} \left| \frac{\partial u}{\partial \mathbf{n}}(\mathbf{y}) \right| \\ &\leq \frac{\pi\epsilon}{2} \left| H_0^{(1)}(k\epsilon) \right| \sup_{\mathbf{y} \in \partial B(\mathbf{x}, \epsilon)} |\nabla u| \end{aligned}$$

Now because  $|\nabla u|$  is continuous in  $B(\mathbf{x}, \epsilon)$  and

$$\begin{aligned} \lim_{\epsilon \rightarrow 0} \frac{\pi\epsilon}{2} \left| H_0^{(1)}(k\epsilon) \right| &= \lim_{\epsilon \rightarrow 0} \epsilon \log(k\epsilon) \quad \text{since } H_0^{(1)}(z) \sim \frac{2i}{\pi} \log z \text{ as } z \rightarrow 0 \\ &= 0 \quad \text{by l'Hopital's rule,} \end{aligned}$$

we can deduce

$$\lim_{\epsilon \rightarrow 0} I_1 = \lim_{\epsilon \rightarrow 0} \int_{\partial B(\mathbf{x}, \epsilon)} \frac{\partial u}{\partial \mathbf{n}}(\mathbf{y}) \Phi(\mathbf{x}, \mathbf{y}) \, ds(\mathbf{y}) = 0.$$

To calculate the limit of  $I_2$ , we write

$$\begin{aligned} \int_{\partial B(\mathbf{x}, \epsilon)} u(\mathbf{y}) \frac{\partial \Phi}{\partial \mathbf{n}}(\mathbf{y}) \, ds(\mathbf{y}) &= \int_{\partial B(\mathbf{x}, \epsilon)} [u(\mathbf{x}) + u(\mathbf{y}) - u(\mathbf{x})] \frac{\partial \Phi}{\partial \mathbf{n}}(\mathbf{y}) \, ds(\mathbf{y}) \\ &= u(\mathbf{x}) \int_{\partial B(\mathbf{x}, \epsilon)} \frac{\partial \Phi}{\partial \mathbf{n}}(\mathbf{y}) \, ds(\mathbf{y}) + \int_{\partial B(\mathbf{x}, \epsilon)} [u(\mathbf{y}) - u(\mathbf{x})] \frac{\partial \Phi}{\partial \mathbf{n}}(\mathbf{y}) \, ds(\mathbf{y}). \end{aligned}$$

Now, note that

$$\begin{aligned}
\lim_{\epsilon \rightarrow 0} u(\mathbf{x}) \int_{\partial B(\mathbf{x}, \epsilon)} \frac{\partial \Phi}{\partial \mathbf{n}}(\mathbf{y}) \, ds(\mathbf{y}) &= \lim_{\epsilon \rightarrow 0} \left( u(\mathbf{x}) \int_{\partial B(\mathbf{x}, \epsilon)} -\frac{ik}{4} H_1^{(1)}(k\|\mathbf{x} - \mathbf{y}\|) \, ds(\mathbf{y}) \right) \\
&= -\lim_{\epsilon \rightarrow 0} \left( u(\mathbf{x}) \times \frac{ik}{4} H_1^{(1)}(k\epsilon) \times 2\pi\epsilon \right) \\
&= -u(\mathbf{x}) \lim_{\epsilon \rightarrow 0} \frac{ik\pi\epsilon}{2} H_1^{(1)}(k\epsilon) \\
&= -u(\mathbf{x}) \left( \frac{ik\pi\epsilon}{2} \times \frac{-2i}{\pi k\epsilon} \right) \quad \text{since } H_1^{(1)}(z) \sim \frac{-2i}{\pi z} \text{ as } z \rightarrow 0 \\
&= -u(\mathbf{x}).
\end{aligned}$$

Also, note that

$$\begin{aligned}
\left| \int_{\partial B(\mathbf{x}, \epsilon)} [u(\mathbf{y}) - u(\mathbf{x})] \frac{\partial \Phi}{\partial \mathbf{n}}(\mathbf{y}) \, ds(\mathbf{y}) \right| &\leq 2\pi\epsilon \sup_{\mathbf{y} \in \partial B(\mathbf{x}, \epsilon)} \left\{ \frac{k}{4} |u(\mathbf{y}) - u(\mathbf{x})| |H_1^{(1)}(k\epsilon)| \right\} \\
&= \frac{k\pi\epsilon}{2} |H_1^{(1)}(k\epsilon)| \sup_{\mathbf{y} \in \partial B(\mathbf{x}, \epsilon)} \{|u(\mathbf{y}) - u(\mathbf{x})|\} \rightarrow 0
\end{aligned}$$

as  $\epsilon \rightarrow 0$ , since  $H_1^{(1)}(k\epsilon) \sim \frac{-2i}{\pi k\epsilon}$ . Therefore  $I_2 \rightarrow -u(\mathbf{x})$  as  $\epsilon \rightarrow 0$ , from which the desired result clearly follows.  $\square$

# Bibliography

- [1] M. Abramowitz and I. Stegun *Handbook of Mathematical Functions* Dover, 1972.
- [2] A. Abubakar and P. van den Berg *Iterative forward and inverse algorithms based on domain integral equations for three-dimensional electric and magnetic objects* Jour. Comp. Phys. Vol 195, pp. 236-262, 2004.
- [3] K. Atkinson *An Introduction to Numerical Analysis* Wiley, 1989.
- [4] K. Atkinson, D. Chien, and O. Hansen *A spectral method for elliptic equations: the Dirichlet problem* Advanced Computational Mathematics, 33:69-1891, 2014.
- [5] K. Atkinson and W. Han *Theoretical Numerical Analysis - A Functional Analysis Framework* Springer, 2009.
- [6] A. K. Aziz and R. B. Kellogg *Finite element analysis of a scattering problem.* Math. Comp, Vol 37, pp. 261-272, 1981.
- [7] S. Bagheri and S. C. Hawkins *A coupled FEM-BEM algorithm for the inverse acoustic medium problem* ANZIAM J, Vol 56, C163-C178, 2015.
- [8] A. Barnett and L. Greengard *A new integral representation for quasi-periodic fields and its application to two-dimensional band structure calculations* Journal of Computational Physics 229:6898-6914, 2010.
- [9] A. H. Barnett and others. <https://code.google.com/p/mpspack/>. (2014).

- [10] P. van den Berg and R. Kleinman *Gradient methods in inverse acoustic and electromagnetic scattering* Large-Scale Optimization with Applications, Part I: Optimization in Inverse Problems and Design (Biegler et al, eds.) The IMA Volumes in Mathematics and its Applications, Vol 92, Springer, Berlin, pp. 173-194, 1977.
- [11] John P. Boyd and Fu Yu. *Comparing seven spectral methods for interpolation and for solving the Poisson equation in a disk: Zernike polynomials, Logan-Shepp ridge polynomials, Chebyshev-Fourier series, cylindrical Robert functions, Bessel-Fourier expansions, square-to-disk conformal mapping and radial basis functions.* Journal of Computational Physics 230.4: 1408-1438, 2011.
- [12] J. H. Bramble *The Lagrange multiplier method for Dirichlet's problem* Mathematics of Computation, Vol. 37, No. 155 pp. 1-11, 1981.
- [13] J. H. Bramble and J. E. Pasciak *A new computational approach for the linearized scalar potential formulation of the magnetostatic field problem* IEEE Transactions on Magnetics, Vol. Mag-18, No. 2, 1982.
- [14] F. Brezzi and M. Fortin *Mixed and Hybrid Finite Element Methods* Springer, Berlin Heidelberg New York, 1991.
- [15] F. Cakoni and D. Colton *A Qualitative Approach to Inverse Scattering Theory.* Springer, US 2014.
- [16] F. Cakoni and D. Colton *Qualitative Methods in Inverse Scattering Theory* Springer, Berlin 2006.
- [17] F. Cakoni, D. Colton and P. Monk *The Linear Sampling Method in Inverse Electromagnetic Scattering* SIAM Publications, Philadelphia, 2011.
- [18] K. Chadan and P. C. Sabatier *Inverse Problems in Quantum Scattering Theory.* Springer, Berlin 1989.

- [19] G. Chavent, G. Papanicolaou, P. Sacks and W. Symes *Inverse Problems in Wave Propagation*. Springer, Berlin 1997.
- [20] D. Colton *Inverse acoustic and electromagnetic scattering theory* Inside Out: Inverse Problems MSRI Publications Volume 47, 2003.
- [21] D. Colton and P. Hähner *Modified farfield operators in inverse scattering theory* SIAM J. Math. Anal. Vol 24, pp. 365-389, 1993.
- [22] D. Colton and R. Kress *Integral Equation Methods in Scattering Theory* SIAM, 2013.
- [23] D. Colton and R. Kress *Inverse Acoustic and Electromagnetic Scattering Theory* Springer, 1992.
- [24] D. Colton and P. Monk *A comparison of two methods for solving the inverse scattering problem for acoustic waves in an inhomogeneous medium* J. Comp. Appl. Math, Vol 42, pp. 5-16, 1992.
- [25] D. Colton and P. Monk *A modified dual space method for solving the electromagnetic inverse scattering problem for an infinite cylinder* Inverse Problems, Vol 10, pp. 87-107, 1994.
- [26] D. Colton and P. Monk *A new method for solving the inverse scattering problem for acoustic waves in an inhomogeneous medium* Inverse Problems, Vol 5, pp. 1013-1026, 1989.
- [27] D. Colton and P. Monk *On a class of integral equations of the first kind in inverse scattering theory* SIAM J. Appl. Math. Vol 53, pp. 847-860, 1993.
- [28] D. Colton and P. Monk *The inverse scattering problem for acoustic waves in an inhomogeneous medium* Quart. J. Mech. Appl. Math. Vol. 41, pp. 97-125, 1988.
- [29] D. Colton and P. Monk *A new method for solving the inverse scattering problem for acoustic waves in an inhomogeneous medium II* Inverse Problems, Vol 6, pp.

935-947, 1990.

- [30] M. Costabel *Symmetric methods for the coupling of finite elements and boundary elements* Boundary Elements IX, pages 411-420. Springer-Verlag, Berlin, 1987.
- [31] M. J. Crocker *Handbook of Acoustics* Wiley, 1998.
- [32] V. Dominguez and F. J. Sayas *Overlapped BEMFEM for some Helmholtz transmission problems* Applied Numerical Mathematics 57, 1311-146, 2007.
- [33] Charles F. Dunkl and Yuan Xu *Orthogonal Polynomials of Several Variables* Cambridge University Press, 2014.
- [34] A. S. Fokas and B. Pelloni *Unified Transform for Boundary Value Problems: Applications and Advances* SIAM, 2015.
- [35] M. Ganesh and S. C. Hawkins *A far-field based T-matrix method for two dimensional obstacle scattering*. ANZIAM J, Vol 51, C215-230, 2010.
- [36] M. Ganesh and S. C. Hawkins *A spectrally accurate algorithm for electromagnetic scattering in three dimensions*. Numerical Algorithms, Vol 43, 35-60, 2006.
- [37] M. Ganesh and S. C. Hawkins *An efficient surface integral equation method for the time-harmonic Maxwell equations*. ANZIAM J, Vol 48, C17-33, 2007.
- [38] M. Ganesh and S. C. Hawkins *A high-order tangential basis algorithm for electromagnetic scattering by curved surfaces*. Journal of Computation Physics, Vol 227, 4543-4562, 2008.
- [39] M. Ganesh and C. Morgenstern *High-order FEM-BEM computer models for wave propagation in unbounded and heterogeneous media: Application to time-harmonic acoustic horn problem* Journal of Computational and Applied Mathematics, Vol 307, pp. 183-203, 2016.



- [40] G. N. Gatica and S. Meddahi *On the coupling of MIXED-FEM and BEM for an exterior Helmholtz problem in the plane* Numer. Math. 100: 663-695, 2005.
- [41] D. Gilbarg and N. Trudinger *Elliptic Partial Differential Equations of Second Order* Springer, 1998.
- [42] C. I. Goldstein *The finite element method with non-uniform mesh sizes applied to the exterior Helmholtz problem* Numer. Math, Vol 38, pp.61-82, 1981.
- [43] C. I. Goldstein *The solution of exterior interface problems using a variational method with Lagrange multipliers* J. Math. Anal, and Appl. 97, 480-50, 1983.
- [44] P. Grisvard *Elliptic Problems in Non smooth Domains* Pitman, Boston 1985.
- [45] C. W. Groetsch *The Theory of Tikhonov Regularisation for Fredholm Equations of the First Kind* Pitman Publishing, 1984.
- [46] S. Gutman *Regularized quasi-Newton method for inverse scattering problems* Mathematical and Computer Modelling, 18:5-31, 1993.
- [47] S. Gutman *Iterative method for multi-dimensional inverse scattering problems at fixed frequencies* Inverse Problems, 10:573-599, 1994.
- [48] S. Gutman and M. Klibanov *Two versions of quasi-Newton method for multidimensional inverse scattering problem* Journal of Computational Acoustics 1:197-228, 1993.
- [49] H. Han *A New class of variational formulations for the coupling finite and boundary element methods* J. Comp. Math. 8 223-232. MR1299224, 1990.
- [50] M. Hanke *A regularizing Levenburg-Marquardt scheme, with applications to inverse groundwater filtration problems* Inverse Problems, pages 79-95, 1997.
- [51] R.F. Harrington *Time-Harmonic Electromagnetic Fields* McGraw Hill, 1961.
- [52] T. Hohage *On the numerical solution of a three-dimensional inverse medium scattering problem* Inverse Problems 17:1743-1763, 2001.

- [53] T. Hohage *Fast numerical solution of the electromagnetic medium scattering problem and applications to the inverse problem* Journal of Computational Physics 214:224-238, 2006.
- [54] Y. Jeon *A Nyström method for boundary integral equations in domains with a piecewise smooth boundary* Journal of Applied Integral Equations, Vol 5, pp. 221-242, 1993.
- [55] C. Johnson *Numerical Solutions of Partial Differential Equations by the Finite Element Method* Cambridge University Press, 1987.
- [56] C. Johnson and J. C. Nédélec *On the coupling of boundary integral and finite element methods* Mathematics of Computation, Vol. 35, No. 152 pp. 1063-1079, 1980.
- [57] D. S. Jones *Acoustic and Electromagnetic Waves*. Clarendon Press, Oxford 1986.
- [58] A. Kirsch *An Introduction to the Mathematical Theory of Inverse Problems* Springer, 2011.
- [59] A. Kirsch and N. Grinberg *The Factorization Method for Inverse Problems* Oxford University Press, Oxford, 2008.
- [60] A. Kirsch and P. Monk *Convergence analysis of a coupled finite element and spectral method in acoustic scattering* IMA Journal of Numerical Analysis 9, 425-447, 1990.
- [61] A. Kirsch and P. Monk *An analysis of the coupling of finite-element and Nyström methods in acoustic scattering* IMA Journal of Numerical Analysis 14, 523-544, 1994.
- [62] A. Kleefeld and T. C. Lin *Boundary element collocation method for solving the exterior Neumann problem for Helmholtz's equation in three dimensions* Electronic Transactions on Numerical Analysis. Volume 39, pp. 113-143, 2012.

- [63] R. Kleinman and P. van den Berg *A modified gradient method for two dimensional problems in tomography* J. Comp. Appl. Math. Vol 42, pp. 17-35, 1992.
- [64] R. Kleinman and P. van den Berg *An extended range modified gradient technique for profile inversion* Radio Science, Vol 28, pp. 877-884, 1993.
- [65] G. A. Kreigsmann and C. S. Morawetz *Solving the Helmholtz equation for exterior problems with variable index of refraction: I.* SIAM J. Sci. Stat. Comput, Vol 1, pp.371-385, 1980.
- [66] R. Kress *A Nyström method for boundary integral equations in domains with corners.* Numerische Mathematik, Vol 58, pp. 146-161, 1990.
- [67] R. Kress *Ein ableitungsfreies restglied für die trigonometrische Interpolation periodischer analytischer funktionen* Numer. Math, Vol 16, pp.389-396, 1971.
- [68] R. Kress *Linear Integral Equations* New York: Springer-Verlag, 1989.
- [69] P. D. Lax and R. S. Phillips *Scattering Theory* Academic Press, New York 1967.
- [70] R. Leis *Initial Boundary Value Problems in Mathematical Physics* John Wiley, New York 1986.
- [71] B. F. Logan and L. A. Shepp *Optimal reconstruction of a function from its projections* Duke Mathematics Journal, 42:645-659, 1975.
- [72] S. Marburg *Six elements per wavelength. Is that enough?* Journal of Computational Acoustics, Vol 10, pp. 25-51, 2002.
- [73] S. Marburg and S. Schneider *Influence of element types on numeric error for acoustic boundary elements.* Journal of Computational Acoustics, Vol 11, pp. 363-386, 2003.
- [74] P. Martin *Multiple Scattering: Interaction of Time-Harmonic Waves with N Obstacles* Cambridge University Press, Cambridge 2006.

- [75] S. Meddahi *An optimal iterative process for the Johnson-Nedelec method of coupling boundary and finite elements* SIAM Journal on Numerical Analysis, Vol. 35, No. 4 pp. 1393-1415, 1998.
- [76] S. Meddahi, M. Gonzalez and P. Perez *On a FEM-BEM formulation for an exterior quasilinear problem in the plane* SIAM Journal on Numerical Analysis, Vol. 37, No. 6, pp. 1820-1837, 2000.
- [77] S. Meddahi and A. Marquez *A combination of spectral and finite elements for an exterior problem in the plane* Applied Numerical Mathematics 43, 275-295, 2002.
- [78] S. Meddahi, J. Valdez, O. Menendez and P. Perez *On the coupling of boundary integral and mixed finite element methods* Journal of Computational and Applied Mathematics 69 113-124, 1996.
- [79] C. Muller *Foundations of the Mathematical Theory of Electromagnetic Waves* Springer, Berlin 1969.
- [80] R. G. Newton *Scattering Theory of Waves and Particles* Springer, Berlin 1992.
- [81] P. Persson and G. Strang *A simple mesh generator in matlab* SIAM Review, Volume 46 (2), pp. 329-345, June 2004.
- [82] M. Reed and B. Simon *Scattering Theory* Academic Press, New York 1979.
- [83] C. Ruland *Ein Verfahren zur Lösung von  $(\Delta + k^2)u = 0$  in Aussengebieten mit Ecken* Applicable Analysis, Vol 7, pp. 69-79, 1978.
- [84] F. J. Sayas *A nodal coupling of finite and boundary elements* Numerical Methods for Partial Differential Equations, Vol. 19, pp. 555-570, 2002.
- [85] A.H. Schatz *An observation concerning Ritz-Galerkin methods with indefinite bilinear forms.* Math. Comp, Vol 28, pp. 959-962, 1974.

- [86] O. Scherzer *Handbook of Mathematical Methods in Imaging*. Springer, New York 2010.
- [87] C. H. Wilcox *Scattering Theory for the d'Alembert Equation in Exterior Domains*. Springer Lecture Notes in Mathematics, Vol 442, Berlin 1975.
- [88] Zienkiewicz, Kelly and Bettess *Marriage a la mode — the best of both worlds (finite elements and boundary integrals)* International Symposium on Innovative Numerical Analysis in Applied Engineering Science, CETIM, Senlis, 19-27, 1977.
- [89] M. Zlamal *Curved elements in the finite element method* SIAM Journal on Numerical Analysis, Vol. 10, No. 1 pp. 229-240, 1973.